Direct Detection of Leptophilic Dark Matter Through Electron Recoil Processes with XENON100

Master's Thesis

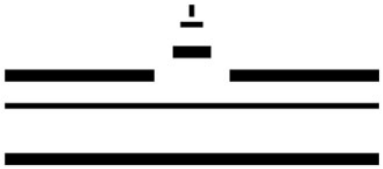

WESTFÄLISCHE
WILHELMS-UNIVERSITÄT
MÜNSTER

Miguel Ángel Vargas

Department of Physics
Westfälische Wilhelms-Universität Münster

This dissertation is submitted for the degree of
Master of Science
First examiner: Prof. Dr. Michael Klasen
Second examiner: Prof. Dr. Christian Weinheimer

Münster, 21 December 2015

To my Grandma..

"In some remote corner of the universe, poured out and glittering in innumerable solar systems, there once was a star on which clever animals invented knowledge. That was the haughtiest and most mendacious minute of world history -yet only a minute. After nature had drawn a few breaths the star grew cold, and the clever animals had to die.

One might invent such a fable and still not have illustrated sufficiently how wretched, how shadowy and flighty, how aimless and arbitrary, the human intellect appears in nature. There have been eternities when it did not exist; and when it is done for again, nothing will have happened. For this intellect has no further mission that would lead beyond human life. It is human, rather, and only its owner and producer gives it such importance, as if the world pivoted around it. But if we could communicate with the mosquito, then we would learn that it floats through the air with the same self-importance, feeling within itself the flying center of the world."

by Friedrich Nietzsche

Acknowledgements

First, I wish to thank my adviser Carlos Yaguna for all his guidance, dedication and patience during the course of this project. Through ups and downs he always tried to guide me into understanding physics better. Equally important, I would like to thank Michael Klasen not only for all his support, advice and assistance, but also for his kindness since the day we met; after all, the opportunity that he gave me to become part of his group has been one of the best experience that I've ever had since my arrival to Germany.

Also, although we haven't work together yet (so I don't know him enough to compliment him as much as I probably should), I would like to thank Christian Weinheimer. His help and encouragement into working extra hard to take advantage of great opportunities just tells me that he is a really thoughtful person. Just as Michael, I find that both are really good influence since their striving to achieve great things can be contagious. I thank Christian for inviting me to be part of his group, I feel really proud of that opportunity.

Last but not least, I'm super grateful with Angela, Patrick, Sonja, Marcel, Saskia, Karol, my family and other people around me that have helped me to get through this experience without even noticed. To be honest the day by day wouldn't have been as fun and entertaining without them.

Abstract

Although Dark Matter (DM) in form of Weakly Interacting Massive Particles (WIMPs) is typically expected to induce nuclear recoils in detector targets, laboratory experiments searching for this scattering off nuclei have so far not been able to establish a discovery [14]. As limits continue to get tighter with no hints of signal detection, it is becoming increasingly worthwhile to consider loosing the assumptions on the WIMP paradigm. In this work, the proposal presented focuses on the mechanism to approach dark matter under the assumption that it induces electronic recoils via inelastic scattering processes when it has scattered against electrons bound in atoms. The practical possibility to detect these electrons interacting with dark matter particles is based on the detectability of the energy released in DM-electron inelastic scattering processes.

In principle, these processes are not considered in the field since it is often assumed that electrons are at rest and therefore, with typical dark matter average velocities of $v \sim 10^{-3}$c, one can realize that the maximal detectable energy is of the order of **eV** (see Appendix A.1); far to low to be distinguishable from background sources and quite challenging for any considered detector in the field. However, since in reality a electron is bound to the atom, even in the case of the atom being at rest, the electron can have a non-negligible momentum p. Hence, interactions of dark matter particles with these high-momentum electrons in an atom at rest can give rise to detectable signals in suitable detectors.

In these processes, the energy transfer to the detector is proportional to the momentum $E_R \sim (pv)$. In principle, an electron momentum $p \sim$MeV would be needed to obtain at least $E_R \sim$KeV, a feasible experimental task. Although such a probability is quite small, is not zero[1], and result after the interaction considered takes place, besides the scattered dark matter particle, the final state can have a prompt electron and a ionized atom or an excited atom plus a possible auger electron/x-ray, as discussed in [21].

[1] As an example, bound electrons in Na(TI) have a probability equal to 1.5×10^{-4} to have a momentum $p \gtrsim$ 0.5 MeV/c [21].

Since dual-phase liquid Xenon detectors have demonstrated sensitivity to such ionization (and scintillation) signals [15], and considering that when writing this work the XENON100 experiment has operated establishing the lowest background experiment achieved among all different dark matter searches (a background control of 5.3×10^{-3} events/Kg/day/KeV [13]) along with some of the tightest exclusion limits for dark matter (a limit on the spin independent WIMP-nucleon cross section in 2012, with a minimum at 2.0×10^{-45} cm^2 for a 65 GeV/c^2 WIMP mass); calculated direct detection limits from this proposed framework are presented and discussed, based on the experimental results from the profile likelihood analysis of 224.6 live days$\times$ 34 Kg exposure of XENON100 experimental data [14, 16].

Additionally, in the context of an effective field theory approach, results from a specialized study of leptophilic interacting dark matter are presented in the scenario of Axial-Vector couplings between dark matter and leptons, where loops diagrams vanish.

Table of contents

List of figures

List of tables

Chapter 1

Introduction to Dark Matter

One of the most extraordinary revelations of the twentieth century is that the majority of the matter in the universe is still unidentified. In fact, only 5% of the mass-energy content of the universe is composed of ordinary baryonic matter, that is, matter made up of protons and neutrons. It seams like a new form of matter, dubbed "*Dark Matter*", fills our universe along with the so-called "Dark Energy"[1].

As asserted by Klasen et al: "If Newton's law of gravity, or general relativity, is valid, then the universe must contain a constituent of unknown nature that betrays its presence only though gravitation. This dark matter may or may not be composed of particles. If so, the absence of a radiative signal or excess scattering of baryonic matter requires that those particles be uncharged and at most weakly interacting." [46].

This Chapter begins by presenting a selective history of dark matter, highlighting at different observational scales some early indications that point out towards its existence. Following, more recent and compiling evidence is presented along with a brief discussion about how these observations fit into the Standard Model of particles. Here are given the conditions to be satisfied by a possible dark matter particle candidate. Lastly, an overview of some of the current detection methods used by experimentalists is presented.

[1] More precisely, nearly 25% correspond to Dark Matter, while the remaining 70% correspond to *Dark Energy*, an unknown and hypothesized form of energy that is believe to permeate all of space and that tends to accelerate the expansion of the universe.

1.1 Early Indications

In the early 1930s, Jan H. Oort studied the motions of stars in the Milky Way and found that their motion hinted at the presence of far more galactic mass than previously predicted [56]. Although he remarked that it could be due to 85% of the light from the galactic center being obscured by dust and intervening matter, his work is considered as an early indication of the presence of dark matter.

Around that time, by studying the Coma Cluster, F. Zwicky[2] found similar indications of missing mass. By assuming only gravitational interaction and Newtonian gravity ($F \propto 1/r^2$) for the galaxies in the Cluster and applying the virial theorem, Zwicky found that the bast majority of the mass of the Coma Cluster was for some reason non-luminous [58]. Roughly 40 years later, Vera Rubin and collaborators measurements of the rotation curves of 60 edge-on spiral galaxies [63] concluded that most stars have the same orbit velocity regardless their distance from the center of the galaxy [64, 24]. This observation extended beyond the optical disk.

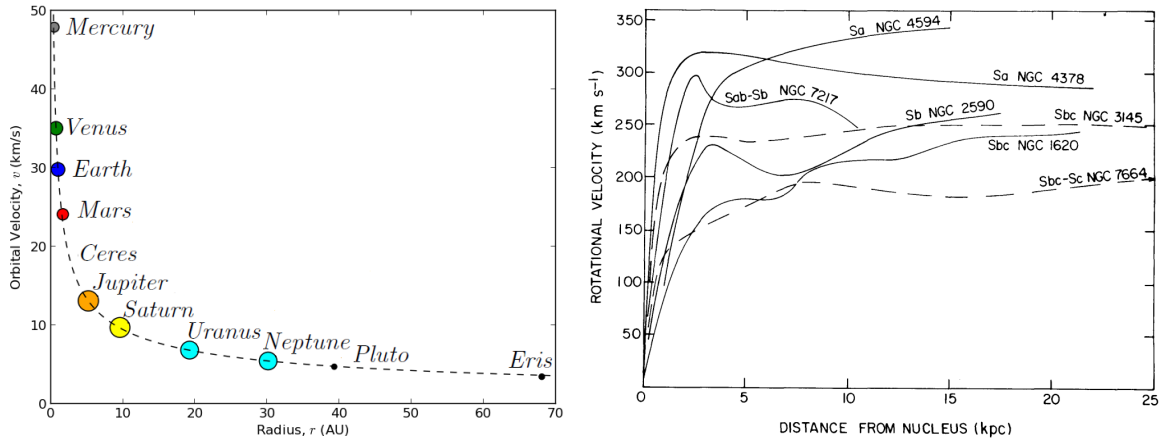

Fig. 1.1 (Left) Rotational velocity curve of the solar system due to the spherically symmetric gravitational potential of the Sun, Source: Matthew Newby, Milkyway@home. (Right) Rotational velocity curves of seven high-luminosity spiral galaxies of different Hubble type, taken from Rubin et al. [65].

As shown in Fig. 1.1, Left, it was assumed that the orbits of the outer stars within a galaxy would approximately mimic the rotation of the planets within our solar system, where the rotation speed of any object at a radius r would be given by $v(r) = \sqrt{G\frac{m(r)}{r}}$, being $m(r)$

[2] In fact, Zwicky's phrase "dunkle (kalte) Materie" is regarded as the origin of the term (cold, i.e. non-relativistic) dark matter.

the total mass contained within r (in our solar system would be essentially the solar mass). However, Rubin's results when assuming Newtonian gravity and luminous matter distribution showed an extreme deviation from the predictions, as it is illustrated in Fig. 1.1, Right. The actual rotational velocity curves found for spiral galaxies hint towards an unexpected fact: with an increasing radius, the mass enclosed must be increasing for the rotational velocities to remain constant. Since the density of luminous mass falls past the central bulge of the galaxy, the missing mass should be somehow non-luminous.

In the 1970s, the direct application of Einstein's theory of relativity in the form of gravitational lensing, the bending and focusing of light and especially the formation of multiple images of a more distant object by a source object acting as a gravitational lens, helped to determine the amount and distribution of dark matter in galaxy cluster. As shown in Fig. 1.2, if a galaxy is located directly behind a cluster, a complete "Einstein ring" appears when looking into the clusters direction (the ring being the image of the more distant object).

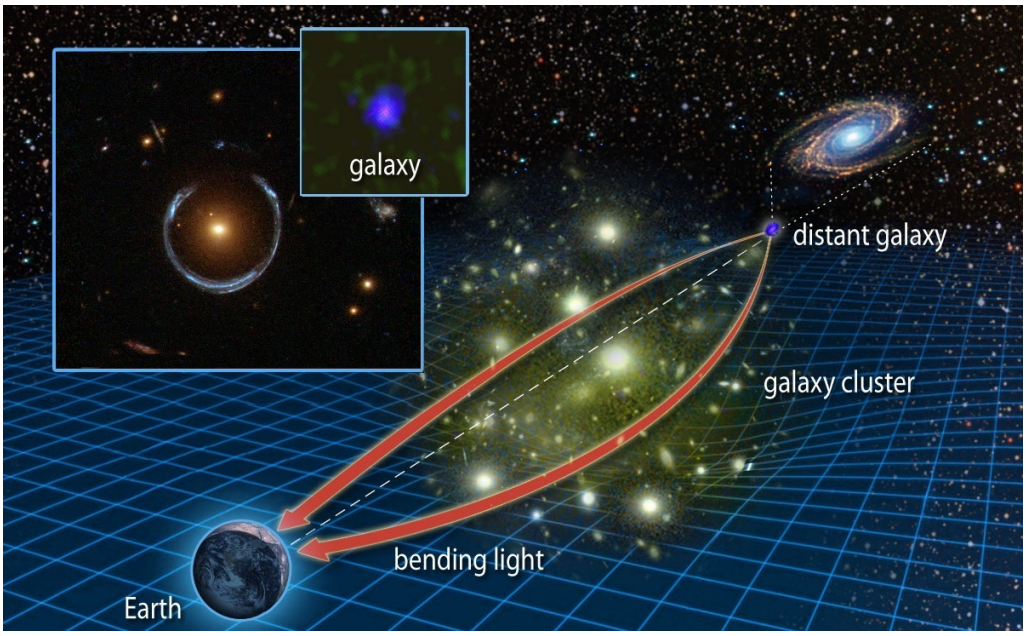

Fig. 1.2 Illustrated effect of gravitational lensing, where the bending of light around a massive object from a distant source. The red arrows show the path of light from the source. Image credit: ESA/Hubble & NASA and Karen Teamura.

A distorted galaxy's image, as shown in Fig. 1.3, can be studied using the expression for the "Einstein radius", Θ_E, which allows to inquire directly the amount of mass causing the

observed lensing, i.e.:

$$\Theta_E = \sqrt{\frac{4GM}{c^2}\frac{d_{LS}}{d_L d_S}},$$

where G is the gravitational constant, M is the mass of the lens, c is the speed of light, and d_{LS}, d_L, and d_S are the distance between the lens and source, the distance to the lens, and the distance to the source, respectively [41]. As calculated by Bergmann et al, [20], different galaxy clusters studied should contain about five times as much as dark matter than the observed baryonic matter.

Fig. 1.3 The galaxy cluster CL0024 1654. This gravitational lens shows strange blue objects stretched, spread in a circle. In reality they are multiple views of a single ring galaxy. Since the likelihood of two appropriately bright and distant objects lining up perfectly is low, distorted galaxies appear as “arclets”, Image credit: ESA/Hubble.

In 1973, as a turning point, the work of Ostriker and Peebles showed that instabilities in models of galaxy disks could be solved by introducing a massive spherical component, a so-called *halo* [57]. Further, along with Yahil, they noted that galaxy masses appear to increase linearly with radius [29]. These results, combined with the latest velocity curves at that time, provided a strong case for the existence of “missing mass” in galaxies.

1.2 Modern Evidence

In order to explain the evidence of dark matter found in different kinds of astrophysical scales through gravitational effects, physicist considered the well known "*dark*" astrophysical objects made of ordinary baryonic matter, such as brown dwarfts, black holes, neutron stars or unassociated planets as first suspects. These candidates were classified as MACHOS[3]. By using gravitational microlensing, the changing brightness of a distant object due to the interference of a nearby object, the EROS-2 survey and the MACHO Collaboration statistically analysed millions of stars for several years. The result was less than 15 possible lensing event candidates in their most promising surveys [5]. Since this low number of MACHOS candidates would only account for a small amount of non-luminous mass, MACHOS were ruled out as baryonic candidates for explaining dark matter.

Most recent and direct evidence for dark matter comes from a system known as the *Bullet Cluster*, the result of a subcluster (the "*bullet*") colliding with the galaxy cluster 1E 0657-56 [51], shown in Fig. 1.4. During their collision, the galaxies between the cluster passed by each other without interacting. However, since the majority of a cluster's baryonic mass exist as a extremely hot gas between galaxies, the collision compressed and shock heated this gas, resulting in huge amount of x-ray radiation observed by NASA's Chandra x-ray observatory.

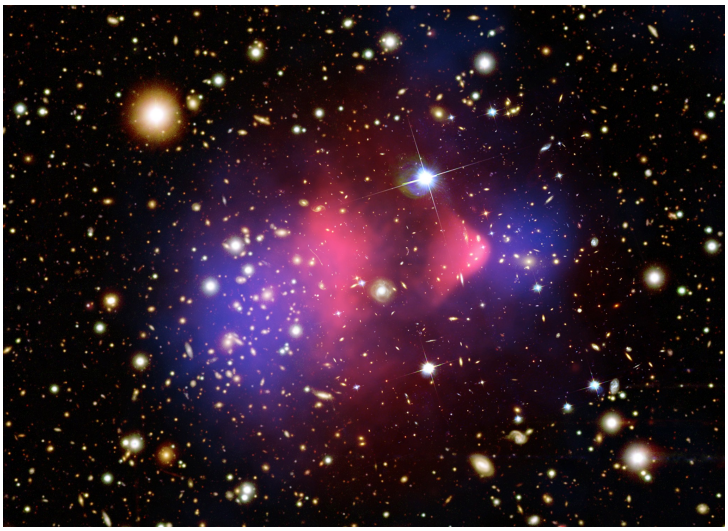

Fig. 1.4 The bullet cluster's individual galaxies are seen in the optical image data, but their total mass adds up to far less than the mass of the two cluster's clouds of hot x-ray emitting gas shown in red. Representing even more mass than the optical galaxies and x-ray gas combined, the blue hues show the distribution of the majority of the mass in the cluster, clearly non-baryonic. Credit: NASA/CXC/CfA/ M.Markevitch et al.

[3]Massive Compact Halo Objects.

When comparing the location of this radiation, which is an indication of the location of the majority of the baryonic mass, to a mapping of the weak gravitational lensing, which is an indication of the location of the total mass, it was exposed that the majority of the mass in the cluster is not concentrated in the areas of strong x-ray emission, revealing that most of the mass must be non-baryonic, as shown in Fig. 1.5.

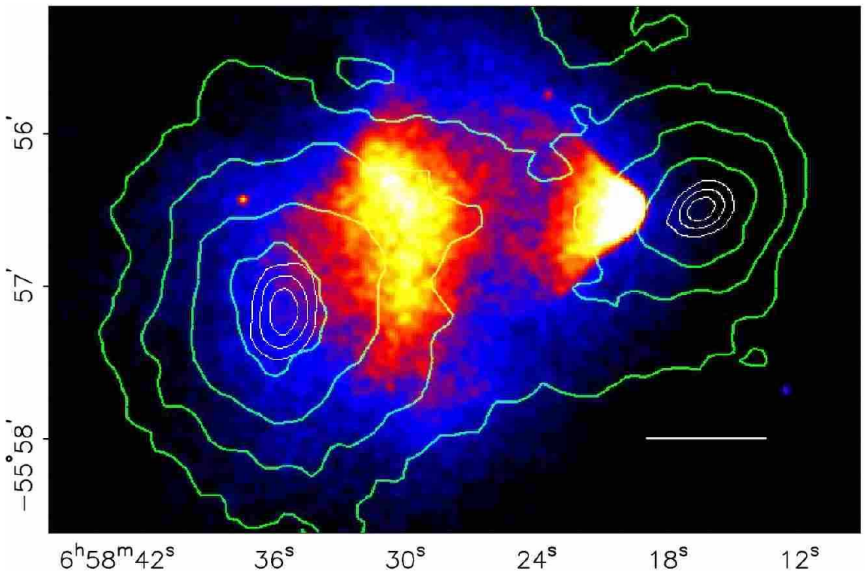

Fig. 1.5 X-ray emission from the "Bullet" cluster of galaxies observed by ground and space telescopes. Colored features correspond to x-ray emission observed by Chandra space telescope, while the green contours correspond to mass reconstruction from weak lensing observations, taken from [43].

Likewise the cosmic microwave background (CMB) provides insight on the composition of the universe. The direct measurements of its spectrum from the COBE [66], the Wilkinson Microwave Anisotropy Probe (WMAP) satellite and most recently from PLANCK[4] has allowed to determine the CMB's temperature anisotropies, $\delta T/T(\theta,\phi) = \sum_{l,m} a_m Y_{lm}(\theta,\phi)$, shown in Fig. 1.6.

[4] A space observatory operated by the European Space Agency (ESA) from 2009 to 2013 [27].

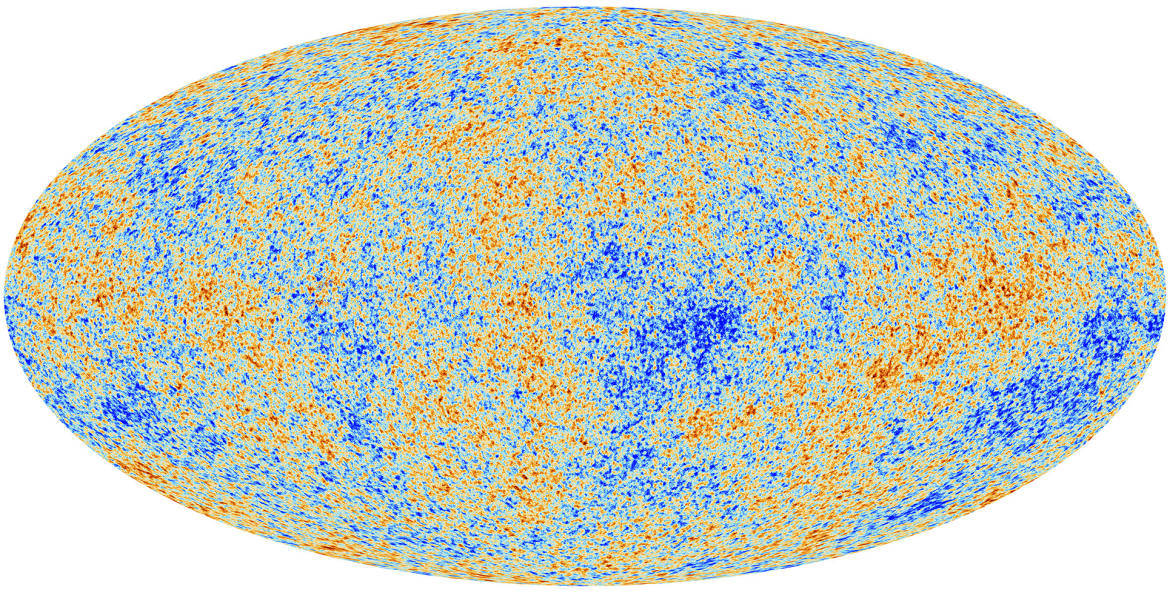

Fig. 1.6 PLANCK map of the microwave sky reveals the primordial anisotropies of the CMB. Taken from [27].

These temperature anisotropies, known as early acoustic fluctuations, can be used to infer the baryonic content of matter in the universe, as shown in Fig. 1.7.

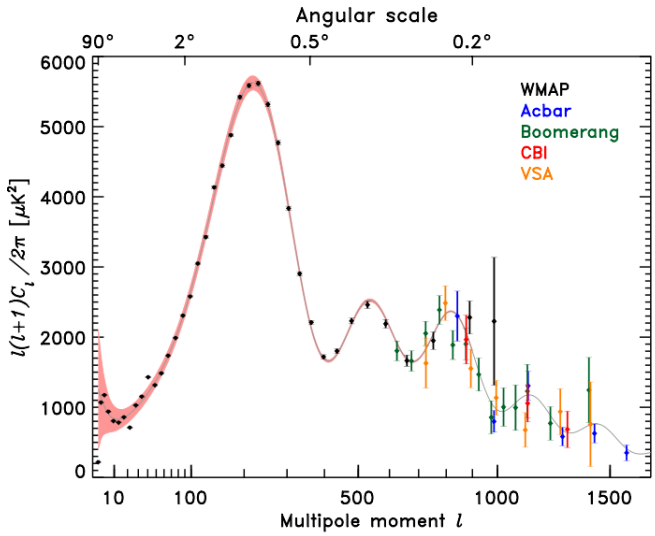

Fig. 1.7 CMB anisotropy power spectrum for various values of Ω_b, from 5 years WMAP data, Credit: NASA/WMAP Science Team.

Here, the first peak in the angular power spectrum of temperature fluctuations indicates the amount of baryonic matter, whereas the other peaks carry information about the non-baryonic mass density. The essential observation once that the results were fitted with the

six-parameter ΛCDM cosmological model [66] indicated the universe is dominated by cold dark matter, having a content of $\Omega_c h^2 = 0.1186 \pm 0.0020$, while having a baryonic content of $\Omega_b h^2 = 0.02226 \pm 0.00023$[5].

Further evidence comes from the requirement of dark matter in cosmology to generate the density perturbations that led to large scale structure [23] and to account for Big Bang nucleosynthesis [45].

1.3 Particle Candidates

Although the existence of dark matter is well motivated by several lines of evidence, its exact nature remains elusive. When looking of the successful Standard Model of elementary particle physics (SM), the quantum field theory that describes three of the four fundamental forces in nature, it is found that despite its huge success, it doesn't contain any particle that can be considered as dark matter.

Although it contains stable, electrically neutral and weekly interacting particles known as *neutrinos*, in principle they are ruled out as the entire solution of the missing mass problem given that neutrinos are relativistic (which would have inhibit the structure formation of the universe) and due to the cosmological constraints from the WMAP (since they constrain the neutrino mass to $m_\nu < 0.23\ eV$, leading to a cosmological density $\Omega_\nu h^2 = 0.0072$, [44]).

Given that there is no direct evidence for dark matter so far, the proliferation of many ideas about its nature has been motivated. However, based on the insights acquired from the observations of the previous sections, one can generalize a considerable number of requirements needed to be fulfilled by a potential dark matter candidate.

First, the candidate *should be dark*, meaning to be non-luminous in order to be in accordance with the current non-observance evidence It *should be stable on cosmological time scales*, as suggested from cosmological observations, regarding the formation of long-lived structures in the universe, such as galactic halos. The candidate *should be non-baryonic*, as suggested by fitting the ΛCDM model to the CMB and after having ruled out MACHOS and neutrinos. Lastly, the candidate *should be cold*, suggested by the formation of large scale

[5]Where $h = 0.678 \pm 0.009$ stands for the present day Humbble constant in units of 100 Km/s/Mpc.

structures in N-body simulations and by the ΛCDM model[6].

The lack of a dark matter candidate, rather than invalidating the SM, provides a motivation to explore Physics beyond the Standard Model (BSM) and suggests that the SM must be extended. Among the wealth of hypothetical candidate particles that could make up dark matter, the most popular dark matter candidates are referred to as Weakly Interactive Massive Particles (WIMPs). WIMPs constituting a large fraction of the dark matter in the universe would be in itself a more appealing solution if these particles were introduced to solve problems related to the SM of particle physics and not the dark matter problem specifically. Nevertheless, as reviewed extensively in [36][7], there is a vast number of viable dark matter candidates that accommodate dark matter properties and that complement SMs problems, including superWIMPs, light gravitinos, hidden dark matter, sterile neutrinos, and axions.

1.4 Detection Schemes

Since the key to determine dark matter properties and its role in the structure in the universe would be to detect it, many experimental probes have searched and are currently searching for a WIMP-like dark matter signals, each one using a different detection method. This section summarizes the main procedures in which experimental dark matter detectives, so called *experimentalists*, are looking for it.

1.4.1 Direct Detection

The basic idea in direct detection is to set up an exceptionally sensitive device containing a large amount of appropriate detection elements. Since dark matter is expected to be slowly traveling everywhere in the universe, then when it would move through the Earth, and therefore through the detection device set up, occasional interactions between the dark matter particles and the detector atoms should take place, leaving as a fingerprint an amount of energy deposited in the detector, as illustrated in Fig. 1.8.

[6]However, this requirement still awaits for a final clarification given that some astronomical observations remained speculative, allowing the cases of cold, warm and hot dark matter to be possible.

[7] Where for each of the candidates their expected production mechanisms, basic properties, and implications for direct and indirect detection, particle colliders, and astrophysical observations are studied.

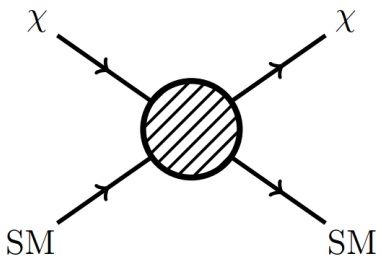

Fig. 1.8 Diagrammatic representation of direct detection for a WIMP from the local dark matter halo interacting with a target nucleus (composed of SM particles) in the detector.

In general, the WIMP signal expected can be recognized given that it should be uniformly distributed throughout the detector[8] and since it should vary at different times of the year due to the Earth moving with or against the velocity of dark matter in the galaxy (i.e. an annual modulation due to the relative motion of the Earth around the Sun [39].) The interaction of the WIMPs within the detector material is classified by being elastic or inelastic, and spin-dependent or spin-independent.

On one hand, in the elastic scattering, the WIMP interacts with the nucleus as a whole, whereas in a inelastic scattering not all the energy goes into nuclear recoil, but instead ends up exciting the nucleus (or some electrons) of the atom.; changing the initial configuration state of the detector and often inducing a decay signal that can be separated from a nuclear recoil event. On the other hand, spin-dependent scattering refers to the coupling of the WIMP's spin with the spin content of the nucleon, whereas spin-independent interactions don't depend on this since such interactions are with the nucleus as a whole.

Furthermore, the recoil events can be categorized depending on the way the energy deposition is measured in the detectors, which can arise in the form of heat (phonons), ionization (electrons) or scintillation (photons). In fact, to discriminate the dark matter signal from background processes and thermal noise, detectors are generally set up to sense two of these signals, such that background events can be recognized on a event-by-event basis.

[8] Since the local dark matter density is thought to be reasonably homogeneous and therefore the cross section would remain constant.

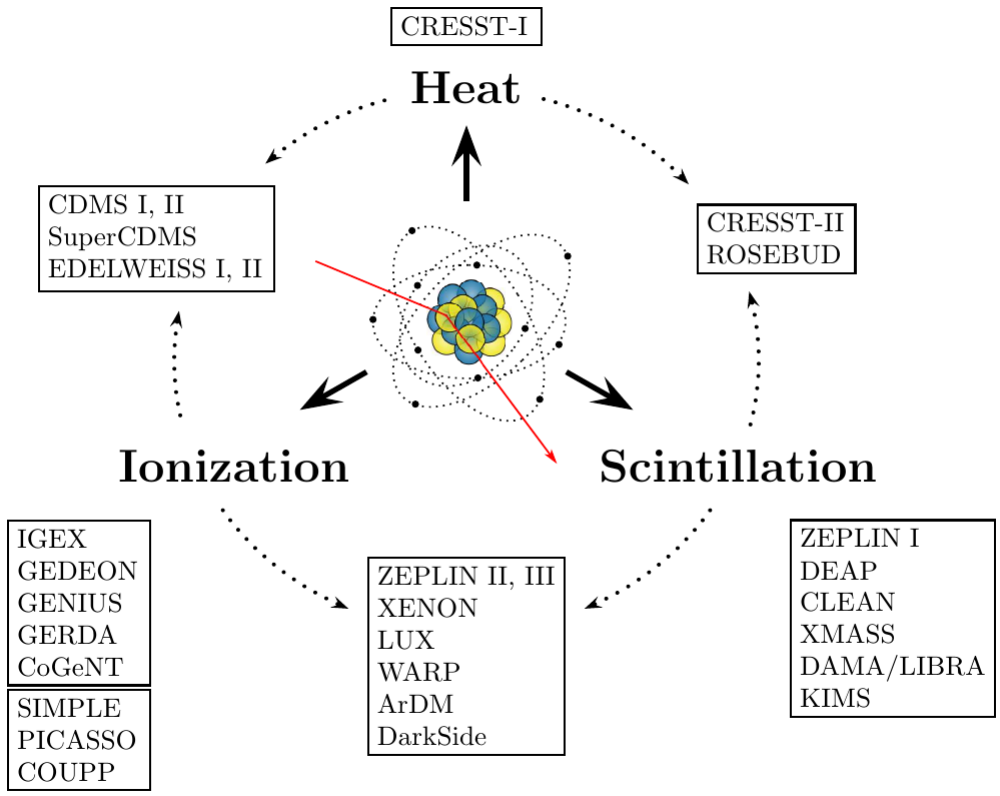

Fig. 1.9 Signal forms detected in undergoing experimental direct detection projects, taken from [59].

As shown in Fig. 1.9, the possible direct detection signals go along with the different measurement techniques that the current experiments implement, with the additional information about the material detector elements used (for a concise review of experiments ongoing and in preparation, see [67]). Additionally, the experiments are placed deep underground in order to shield against all possible background sources.

1.4.2 Indirect Detection

Dark matter cannot only be detected directly in dedicated experiments searching for deposition of energy after it has scattered with a detector, as mentioned before, but it can also reveal its existence indirectly. The goal of this approach is to search for the products of WIMP annihilation or decay. If WIMPs are their own antiparticle, then two WIMPs could annihilate to produce gamma rays or SM particle-antiparticle pairs, as illustrated in Fig. 1.10. Additionally, if the WIMP is unstable, they could decay into SM particles as well.

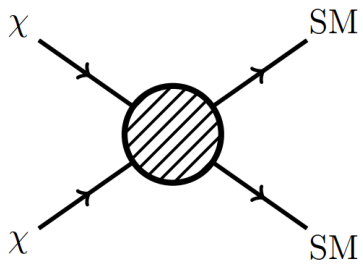

Fig. 1.10 Heuristic diagrammatic representation of indirect detection.

The focus of indirect detection methods lies into the observation of cosmic-rays created by WIMP annihilations in galactic halos and the signatures from WIMP captured in massive bodies such as stars and planets, given that the annihilation rate of WIMPs is proportional to the square of the dark matter density. The natural approach is to investigate places with high WIMP densities, such as the sun, the galactic center or stars. In such places, searches look for product signatures including antimatter (positron and anti-protons), an excess of gamma rays[9] (mono-energetic) and neutrinos.

1.4.3 Collider Production

Direct production, illustrated in Fig. 1.11, is related by crossing symmetries to the direct detection approach. Here dark matter particles may be produced in colliders by collisions of SM. Producing and detecting dark matter in an accelerator would be a crucial step forward to understand the universe better. Since many theories state that dark matter particles are light enough to be produced, for example, at the LHC or at the TEVATRON, several distinctive features in these accelerators are under study.

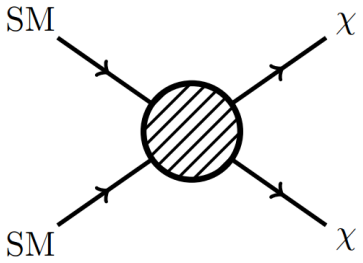

Fig. 1.11 Diagrammatic representation of collider signatures.

Although it wouldn't be possible to detect the dark matter particles directly, they may be detected through missing mass in the collision products. In fact, as it turns out, the

[9] One difficulty when estimating γ-ray rates from dark matter annihilation is the still poorly known distribution of halo dark matter on the smallest galactic and subgalactic scales.

main advantage of dark matter production at colliders is that there is independence from astrophysical uncertainties as well as the sensitivity to very low DM masses; which strongly complements direct and indirect searches. In general, in order to keep analysis as model independent as possible, one usually makes use of the framework of Effective Field Theories (EFT), as will be explained in Chapter 4.

Chapter 2

Direct detection: XENON100

At present, different considerable experiments efforts are under way aiming to uncover the nature of dark matter. Since several extensions of the Standard Model predict dark matter in the form of a stable Weakly Interacting Massive Particle (WIMP), numerous experimental probes are looking for its interactions in terrestrial detectors, where they are expected to scatter off nuclei. At the cutting edge of direct detection strategies, liquified noble gas detectors are currently at the lead of technologies being the most sensitive searches in operation by having the best exclusion bounds achieved so far, while controlling strongly background counting, see [14] and [3]. In particular, liquid xenon (LXe) is a well known suitable target for WIMP direct searches since allows discrimination between nuclear and electronic recoils, it is easily scalable to larger target masses and presents excellent shielding properties against external background sources [7].

Based on the success obtained by the XENON10 experiment [6], the first two-phase xenon time-projection chamber (TPC) developed within the xenon dark matter program [9], the XENON Collaboration (X.C.) designed and built at Laboratori Nazionali del Gran Sasso (LNGS), Italy, an upgraded version of this project by focussing on the detectors performance, component selection and the design of a new TPC with a factor of 10 times more mass and a factor of 100 times less electromagnetic background.

This improved version of the XENON10 experiment is known as the XENON100 experiment, a detector filled with a total of 161 Kg of ultra pure liquid xenon, divided in two concentric cylindrical volumes. The inner target volume of the detector is a two-phase (liquid/gas) TPC of 30,5 cm height and 15,3 cm radius containing a xenon mass of 62 Kg, being surrounded by a optically separated LXe veto of 99 Kg, close on the bottom by a cathode mesh and on the top by a gate and a node mesh.

Given that the goal of this work is to calculated direct detection limits for the dark matter mass under the assumption that it induces electronic recoils via inelastic scattering processes (implementing the experimental results from the profile likelihood analysis of the X.C.), this chapter presents a basic description of the XENON100 experiment, along with relevant details concerning how the analysis of the searched data is performed and how in a general way, standard science data is obtained. More precisely, the aim of this chapter is to provide the sufficient background to understand and recognize how different theoretical constraints can be inferred from the capabilities and characteristics of the XENON100 experiment.

2.1 Principle of the XENON two-phase TPC

The Xenon detectors are basically two-phase (liquid-gas) time projection chambers and their principle of operation is explained and shown schematically in Fig. 2.1, [15]):

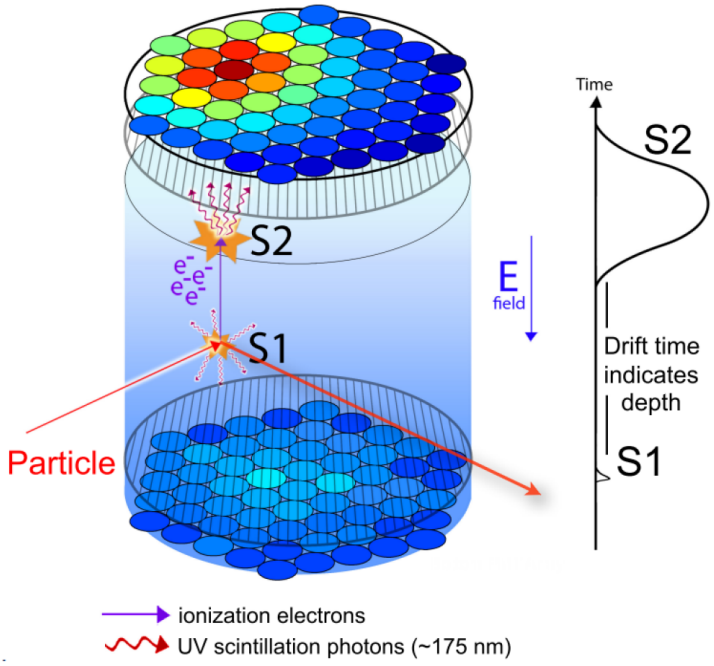

Fig. 2.1 Scheme of the working principle of the XENON two-phase liquid-gas TPC. When a particle scatters in the LXe, the deposited scattering energy leads to excited and ionized xenon atoms, resulting in a prompt S1 signal coming from a scintillation process, and a delayed proportional scintillation signal called S2, coming from the ionised and drifted electrons, taken from [15].

In principle, when a recoiling particle interacts within the active LXe volume it creates a track of excited Xe atoms or free excitons, Xe^*, and electron-ion pairs $Xe^+ + e^-$. After the

creation of the excitons and electron-ion pairs, the scintillation signals is produced, as shown schematically in Fig. 2.2. Here, excitons can form excited states, Xe_2^*, called excimers, when colliding with the surrounding of the Xe atoms [7]. As for ionized atoms, they can also form excimers through a series of recombinations[1], ending also in excimers that subsequently decay into the dissociative ground state, producing scintillation photons in the ultraviolet range, $Xe_2^* \rightarrow 2Xe + h\upsilon$, centered at a wavelength of 178 nm[2].

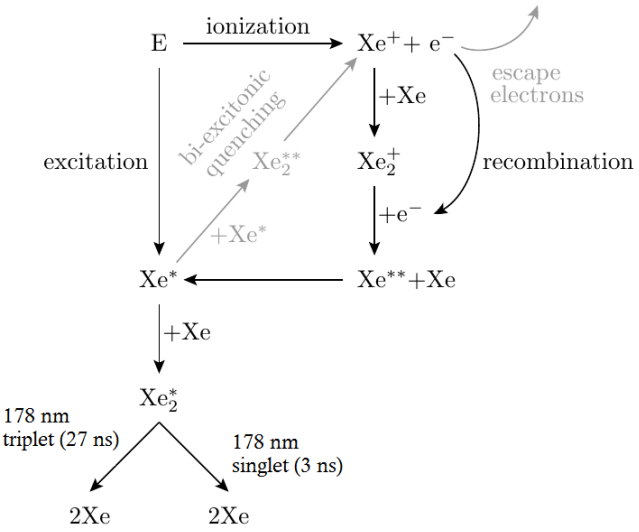

Fig. 2.2 Scintillation mechanism in LXe (black) and different processes that can lead to scintillation light (gray). Taken from [59].

In general, after the interaction of the recoiling particles happens, an electron drift field generated by thin stainless steel foils, resulting in a drift field of 530 V/cm across the TPC, drives a large fraction of the ionized electrons away from the interaction of the LXe phase. The electrons that reach the liquid-xenon interface are extracted into the gas phase by an extraction field of -12 KV/cm[3][3], where the are accelerated to amplify the charge signal into a proportional scintillation signal [30], see Fig. 2.1. As a whole, both the S1 direct and the S2 proportional scintillation light, with 178 nm wavelength, are detected by a concentric circle array of Hamamatsu 8520-06-A1 1" square photomultiplier tubes placed in the top of the detector.

The x- and y- coordinates of the events is inferred from the proportional scintillation hit patterns on the PMTs placed in the gas phase, as shown in Fig. 2.3. The z- coordinate

[1] Specifically, as indicated: $Xe^+ + e^- \rightarrow Xe_2^+$, $Xe_2^+ + e^- \rightarrow Xe^{**} +$ heat, $Xe^* + Xe \rightarrow Xe_2^*$.

[2] The ionization and scintillation signals are thus complementary and anti-correlated as suppression of recombination by an external field results in more free electrons and less scintillation photons.

[3] This field is high enough to obtain an extraction close to 100%.

is proportional to the time difference between S1 and S2 signals, when drifting an electron at a given constant drift field in the TPC. Thus, xenon TPC design translates into a full 3-dimensional vertex reconstruction on an event-by-event basis, providing the ability to fiducialize the target volume, yielding into an inner core with a very low radioactive background.

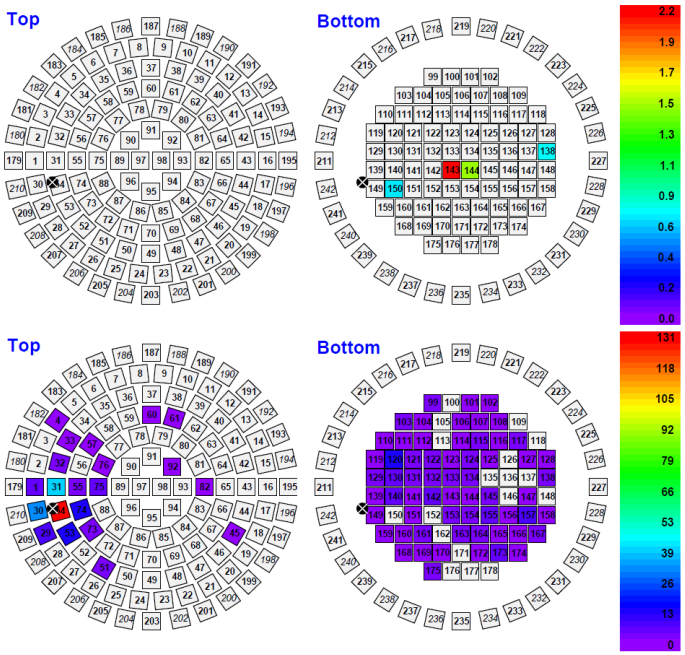

Fig. 2.3 PMTs hit pattern of the event. Here, the numbers indicate individual PMTs, the color code is proportional to the signal (in PE) seen by the respective PMT. (Top) S1 hit pattern (Bottom) S2 hit pattern, taken from [15].

To sum up, Xenon is a natural choice for a direct detection medium due to all its advantages, particularly since among liquid rare gases, LXe has the highest stopping power for penetrating radiation, it has also the highest ionization and scintillation yield, and most importantly due to its particular resulting low-background control due to its self-shielding properties (an extensive survey regarding a detailed description of the instrument selection, design and description of the XENON100 detector and associated systems can be found in [59, 54]).

2.2 From data acquisition to results

Due to the extensive amount of details surrounding the procedures needed in order to overcome the challenge of going from data acquisition, into attain a definitive data set surpassing

all kind of selection criteria, evaluation of cuts acceptance and background estimates; this section presents an overview of different relevant techniques implemented in the analysis of the data collected from the XENON100 experiment.

As illustrated in Fig. 2.4, in the context of direct detection, there is a general "schematic route map" that is followed in order to achieve standard cross-section exclusion limits. This sections describes each step of the route.

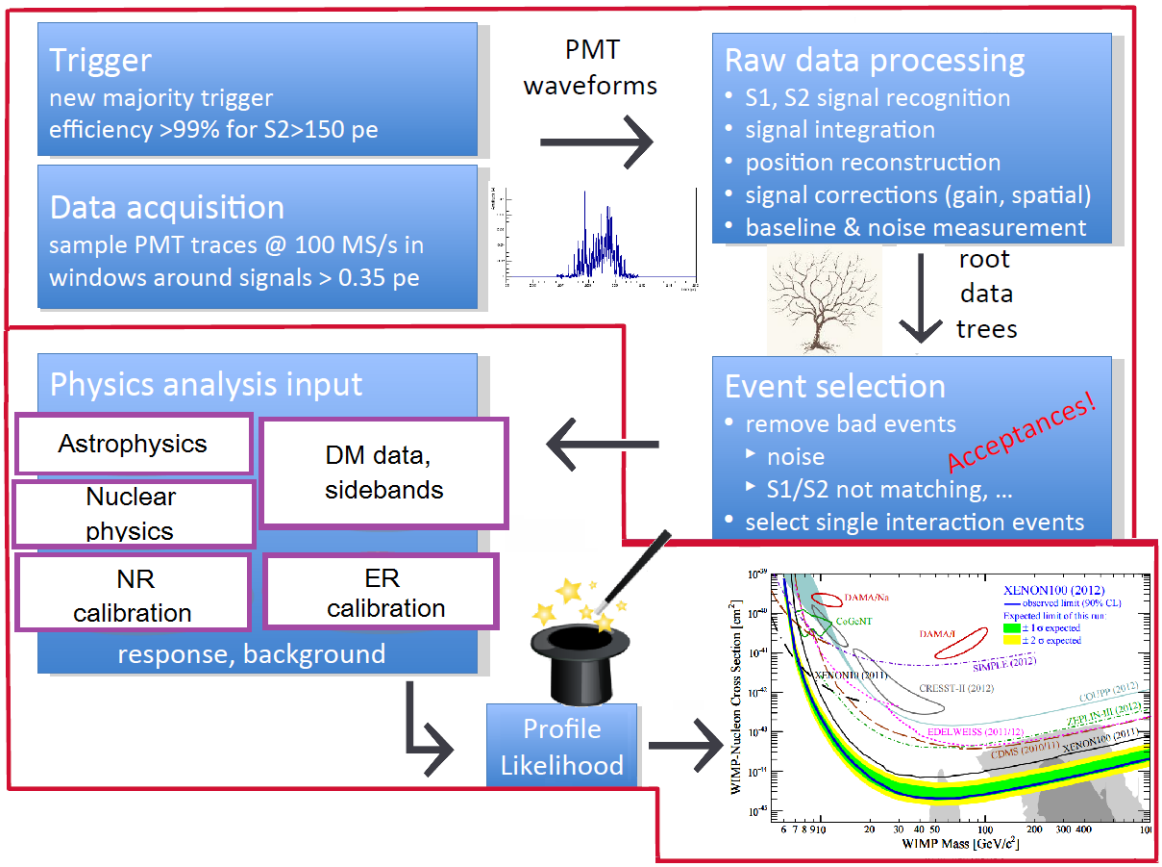

Fig. 2.4 Schematic path from raw data to results, taken from XENON100 Analysis Workshop [55].

2.2.1 Data acquisition

The first stage of this path has to do with the XENON100 data acquisition system (DAQ). In principle, this system is divided by 3 subsystems: *the trigger*, *the waveform acquisition subsystem* and *the rate and time accounting subsystem*.

In that order, the DAQ starts by using a S2-based trigger scheme, then digitalizes the

wave-forms of the 242 PMT taking place in the TPC by using a CAEN VME V174 flash ADCS[4], and lastly, for an easier access to the raw waveforms of a particular event, it records the time of every accepted trigger with microsecond resolution; so the data ends up stored in an indexed file format.

2.2.2 Processing of data

The second stage has to do with the processing of raw data and the extraction of physical parameters from these waveforms recorded. The initial analysis proceeds from the raw data acquired for each event, consisting of 242 waveforms of usually around 40000 samples which get stored in a xenon event data file format called (XDIO) by using the libxdio library. This raw data is essentially converted into physical parameters by using a program specifically written for XENON100, the data processor "xerawdp".

The conversion proceeds in three stages: *preprocessing the waveforms*, *searching for peak candidates* and *computing the reduced quantities associated to each peak candidate*. Respectively, the preprocessing of waveforms starts when the digitized samples from the XDIO event layer are read and converted from ADC counts to volts. By doing this, the waveforms of all targets volume channels are added into a summed waveform that is used to search for S1 and S2 peak candidates, as shown in Fig. 2.5.

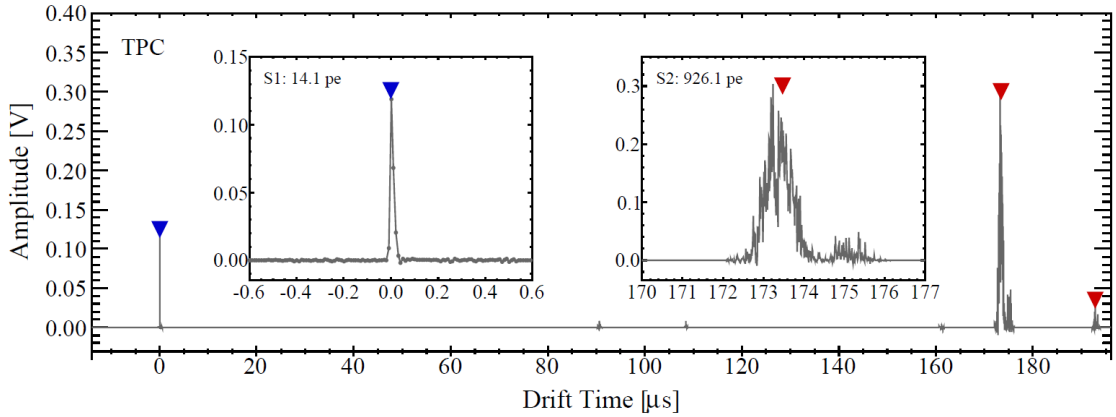

Fig. 2.5 TPC and veto summed waveforms for a typical low-energy event. The blue triangle indicates the S1 peak candidate found and the red triangles the S2 peak candidates, taken from [59].

Proceeding, peak identification is performed by several Root based C++ programs used to distinguish genuine peaks and to derive physical quantities from them. Once that all the

[4] An 8 channel 14 bit flash ADC waveform digitalizer.

peaks candidates are identified, the computations of the quantities of interest for each peak are performed. This is accomplished in five different steps: computation of quantities that don't depend on PMT gains (see Section 2.2.3), computation of quantities that do depend on them, reconstruction of *(x,y)* position for each S2 peak, correction of positions using simulated drift field, correction of the position dependence of the S1 and S2 signals for each peak, and finally the computation of other position dependent quantities within the target volume.

The results concerning all the previous steps can be summarized as follows: for each peak considered, properties like the width, height, mean time arrival, number of PMT coincidences, etc., are calculated, along with a few other parameters from the waveforms: its total area, the total S1 and S2 signal.

After having calculated those reduced quantities, the process is followed by the computing of the (x,y) position of each S2 peak candidate[5] together with the z-coordinate from the time difference $\Delta t = t_{S2} - t_{S1}$ between the prompt S1 and the delayed S2 signal, since in the uniform electric drift field the electrons drift velocity is constant.

2.2.3 Signal corrections

By means of the previous procedures, so far, it has been accomplished S1, S2 signal recognition, signal integration and position reconstruction of events. However, both the light and the charge signals can be attenuated in the process due to the presence of impurities in the LXe, e.g. argon, nitrogen and helium. Consequently, different calibrations have to be incorporated in order to correct and optimize the measured signals.

To begin with, several hardware components of the detector need to be calibrated before they can be used. The most fundamental ones are the providers of the signal, the PMTs, which are calibrated in a single photoelectron regime using a pulse LED[6]; this light level shows a photoelectron signal in the time window considered in the analysis, see Fig. 2.6.

[5] This is made using 3 different position reconstruction algorithms: neural network algorithm, x^2 minimization or support vector machine algorithm CSVM.

[6] The LED intensity is chosen such that most of the events acquired (>95%) in the PMTs don't register a signal.

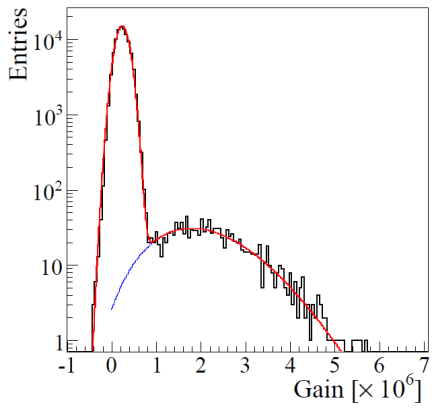

Fig. 2.6 Typical PMT calibration spectrum. The position of the single photoelectron peak in the pulse area is directly proportional to the gain of the tube, taken from [15].

Most remaining basic calibrations throughout the measurement have to do with corrections to the S1 and S2 signals, this is, by introducing calibration sources such as ^{137}Cs, ^{57}Co, ^{60}Co and ^{232}Th, the S1 light yield is obtained, the electron lifetime τ_e is infer[7], and then the response of the S2 signal is optimized by varying some parameters, as the path length of the electron, the electric field, the pressure in the amplification, etc. As a whole, the sum of all these corrections translates into the overall position correction map shown in Fig. 2.7, and into an (r,z) correction map for light collection shown in Fig. 2.8; acquired by guiding the corrections to reach the highest possible light collection efficiency in the TPC.

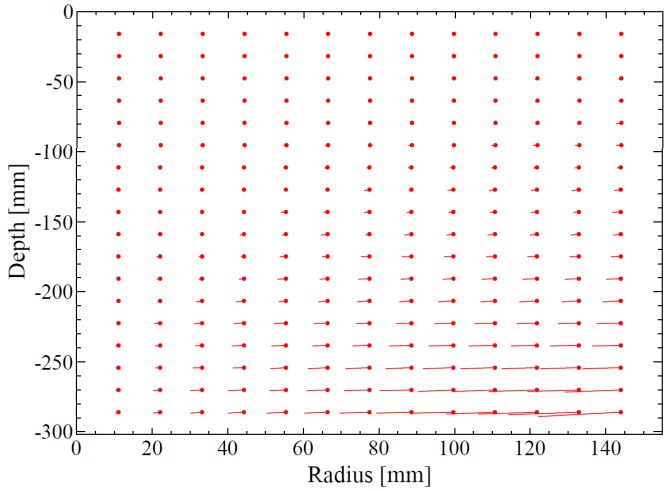

Fig. 2.7 Graphical representation of the position correction at different points within the TPC. The correction uses the inverse of this map to transform reconstructed event positions into physical positions, taken from [15].

[7]Which is the time at which the total number of electrons produced is reduced by $1/e$.

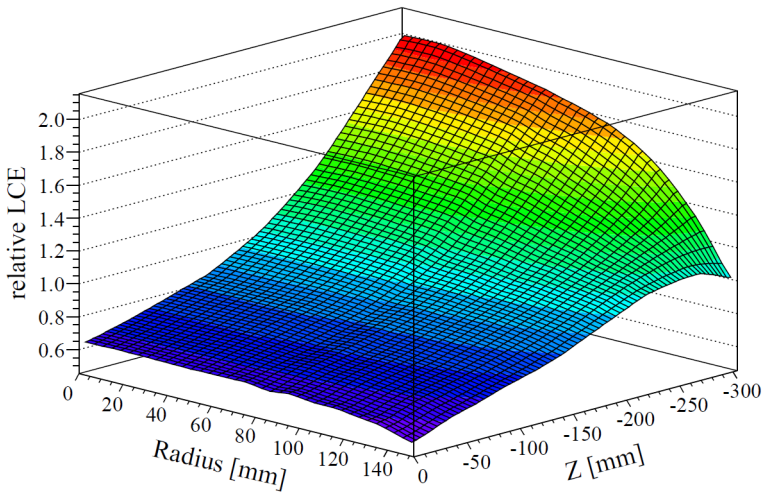

Fig. 2.8 Correction map for the light collection efficiency (LCE) obtained from the 40 keV line: The vertical axis shows the value to correct a measured S1 (light) signal at a given (r,z) position. z=0 mm denotes the top of the TPC, taken from [15].

The impact of all these mentioned corrections on the signals, including many other corrections, is illustrated in Fig. 2.9.

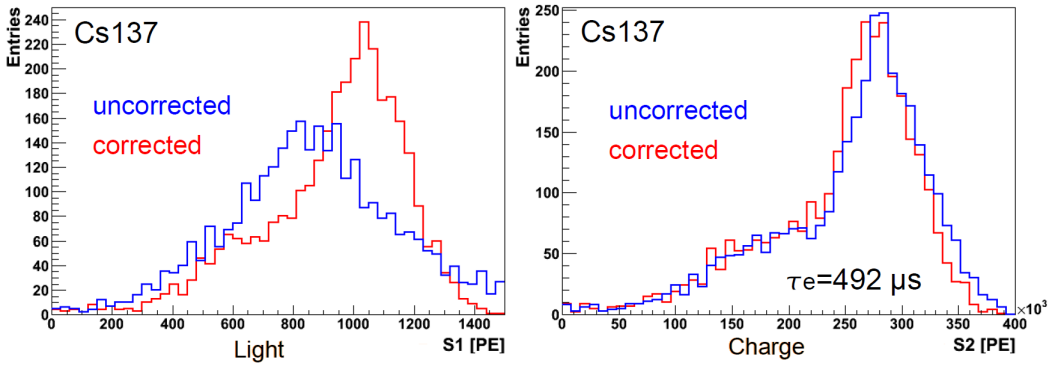

Fig. 2.9 S1 light collection correction dominates over S2 corrections (electron lifetime+LCE), taken from [55].

Lastly, by using the auto-correlation of the light and the charge from signals in LXe, one can obtain an ellipse in the S2-S1 plane, which can be described with a 2D Gaussian in order to determine an anti-correlation angle θ, implemented to attain an improved energy resolution for every calibration line, see Fig. 2.10

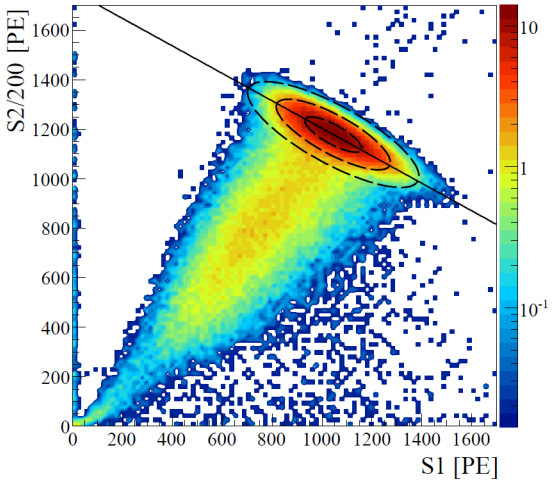

Fig. 2.10 ^{173}Co calibration data in position-corrected S2-S1 parameter space. The signals are anti-correlated and a projection along the anti-correlation ellipse leads to an improved energy resolution. The color scale gives the number of events per bin, taken from [15].

2.2.4 Event selection

This section describes some of the criteria applied to the science data in order to select candidates in the energy region of interest. To attain this goal, different categories of methods must be conducted: basic quality cuts, multiple scatter cuts, fiducal volume cuts and signal consistency cuts. The acceptance of these cuts, meaning the fraction of good events which pass them, is typically high as they are meant to remove erroneous signals. Respectively, basic quality cuts are the starting point and they enforce minimal requirements on the S1 and S2 signals in order to remove noisy or non-physical waveforms, as shown in Fig. 2.11. Four quality cuts are used here, a S1 coincidence cut, a S2 threshold cut, a signal to noise cut and cuts for specific event types.

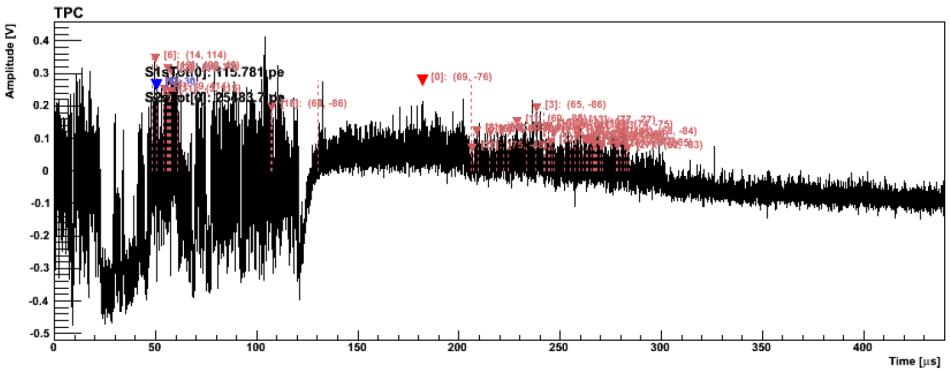

Fig. 2.11 Rejection of non-analyzable waveforms, taken from [55].

The S1 coincidence cut requires a twofold PMT time-coincidence of the S1 signal within a 20 ns time window with a signal size larger than 0.35 PE for each PMT. For the S2 signal, the lower threshold for valid events is >300 PE. The signal to noise cut requires events outside of the detected S1 and S2 signals to contribute less than a specific fraction of the total area of waveform, rejecting in this way events with excessive noise.

Multiple scattering cuts require the presence of a single S1-like peak in the waveform, a single S2 peak above the 300 PE threshold and simultaneously no energy deposited in the veto in coincidence with the signal in the TPC, as shown in Fig. 2.12. The multiple scatter cuts for S1 end up rejecting events with delay or accidental coincidences, while for S2, due to the consistency of the reconstructed (x,y) event positions, from the three previously mentioned algorithms, used up to a radius of r< 14 cm, the fiducial volume cuts translate into choosing a cylinder with a radius of 13.5 cm and 24.3 cm height[8].

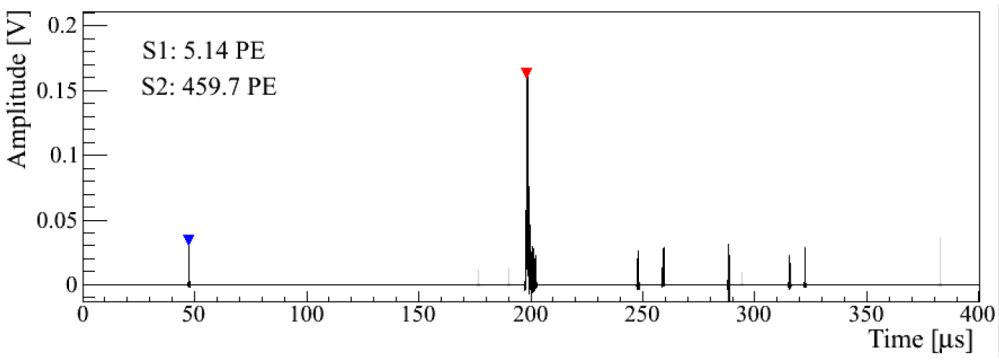

Fig. 2.12 Single scatter selection of only one S2 peak >95%, only one S1 peak >98.8%, rejecting anomalous events or double scatters, taken from [55].

Finally, strong consistency cuts come from x-y position consistency and from the width of S2 pulses. Ionization electrons diffuse as they are drifted through LXe and thus will produce a proportional signal with larger width than for shorter drift times, as illustrated in Fig. 2.13.

[8]Fiducalization reduces the background but also the exposure, hence reduces the sensitivity. The measurements chosen comprise the optimization of the shape and fiducal mass.

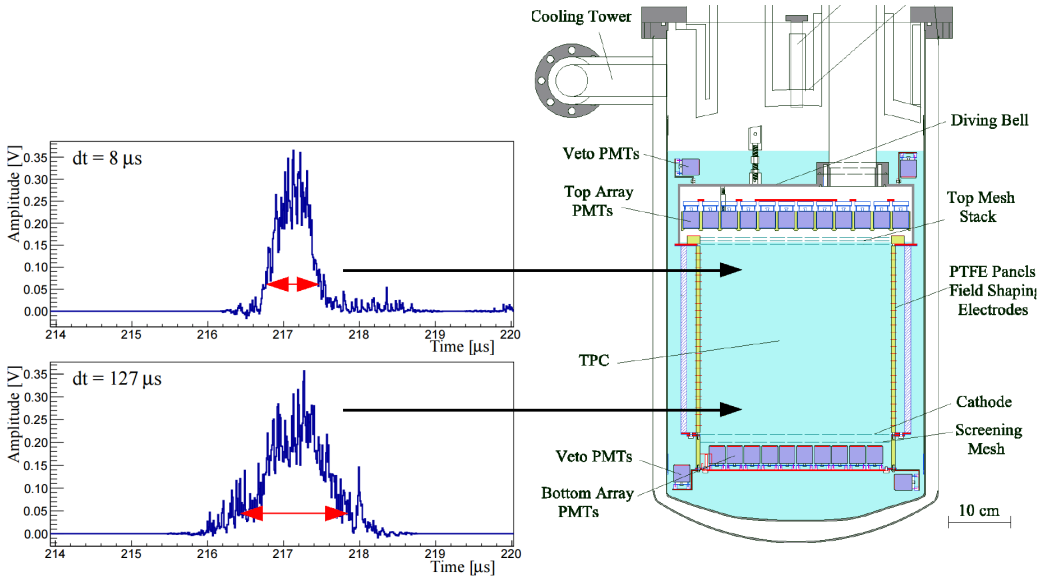

Fig. 2.13 The observed width of the S2 signal (from dispersion of electron cloud) must be consistent with the interaction depth derived from the S1-S2 time distance. Taken from [55].

Then the cut requires the width of the S2 signal to be consistent with the reconstructed event depth. In total, the combined acceptance of the quality cuts as a function of the corrected S1 signal is show in Fig. 2.14.

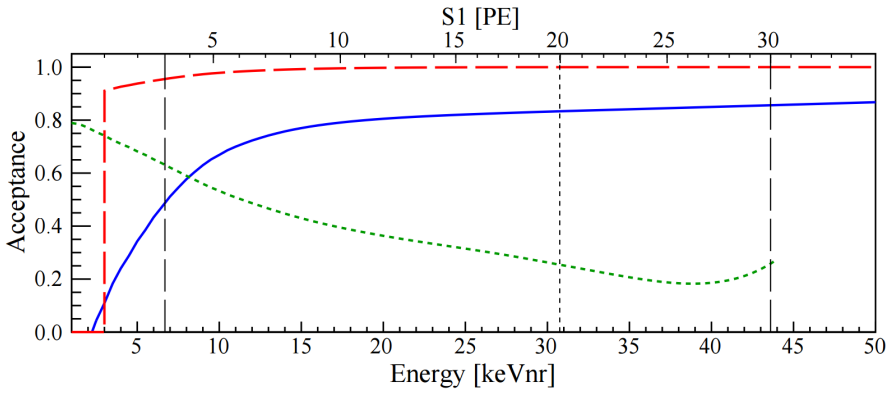

Fig. 2.14 Combined cut acceptance (solid blue). S2 threshold cut S2 >150 PE (dashed red), lower analysis threshold is 6.6 keV_{nr} (3 PE) and extends to 43.3 keV_{nr} (dashed black lines). Taken from [14].

2.2.5 Background expectation and Energy scale

As previously mentioned, XENON100 is installed at the laboratory Nazionali del Gran Sasso (LNGS), at an average depth of 3600 m water equivalent, such that there is an approximate muon flux suppression of 10^6 with respect to the sea level [1]. Despite this natural shielding,

both nuclear and electronic recoil interactions contribute to the expected background of the search.

On one hand, nuclear recoil (NR) backgrounds come primary from muon-induced neutrons, neutrons created in spontaneous fission and (α,n) reactions in the detector material. They are determined by using the measured intrinsic radioactive contamination of all detectors and shielding materials, as well as from the consideration of the muon energy and angular dependence at LNGS [70]. Given the exposure and NR acceptance, the expectation from these neutron sources is $\left(0.17^{+0.12}_{-0.07}\right)$ events.

On the other hand, electronic recoil (ER) backgrounds originate from radioactivity of the detector components and from γ and β intrinsic radioactivity in the LXe target, such as ^{85}Kr and ^{222}Rn. From these two sources, the former source is the most critical one given that it can not be diminished by fiducialization [11]. Instead, this ^{nat}Kr concentration gets lowered by implementing cryogenic distillation[9].

As a whole, ER total background contribution was estimated from ^{60}Co and ^{232}Th calibration data sources. It was found that the majority of ER events consisted of events Gaussian distributed, with a few events leaking anomalously into the NR band[10]. Altogether, ER total background was estimated to be (1.0 ± 0.2) events [14].

Finally, the derivation of a NR energy scale for WIMP expectation analysis, E_{NR}, can be attained from the S1 signal by fitting all direct measurements of the relative scintillation efficiency of NR in LXe, $\mathscr{L}_{eff}$, using the relation $E_{NR} = (S1/L_y)(1/\mathscr{L}_{eff}(E_{NR}))(S_{ee}/S_{nr})$ [59]. Here, $\mathscr{L}_{eff}$ is based on all available direct measurements presented in [11]. The factors $S_{ee} = 0.58$ and $S_{nr} = 0.95$ describe the scintillation quenching[11] due to a electronic field [8], and the Light Yield $L_y = (2.28 \pm 0.04)$ PE/Ke V_{ee} is the updated response from a fit to all 122 KeV γ-rays.

2.2.6 Partial Results

The search data used for the analysis were accumulated over a period of 13 months between February 29, 2011 and March 31, 2012; being interrupted only by regular calibrations to

[9] The cryogenic distillation column set up was designed and tested at the Westfälische Wilhelms-Universität Münster [62].

[10] Mainly, events with incomplete charge collection contribute to the anomalous background.

[11] These quenching factor can be understand in the context of Lindhard theory, the ratio of energy given to the electronic excitation to the total energy.

monitor PTM response, LXe purity and ER background calibration. The results are shown in Fig. 2.15, were the denominated signal (NR) and Background (ER) events are distinguished by their different S2/S1 ratio, were only the S2 signal detected by bottom PMTs, $S2_b$, is used since it requires smaller corrections, [14].

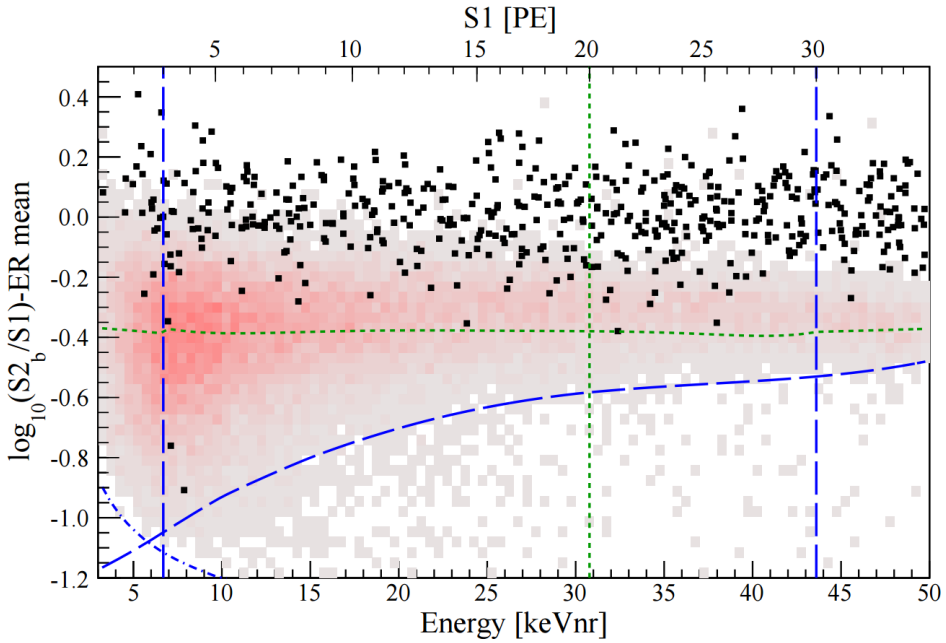

Fig. 2.15 Final distribution of events in the electronic/nuclear recoil discrimination parameter as a function of nuclear recoil energy E_{NR}, taken from [48].

The WIMP search was restricted to the energy window of 3-30 PE, corresponding to 6.6-43.3 KeV_{nr} energy equivalent. A profile likelihood (PL) statistical interference analysis, explained in Appendix C.1, is introduced, so both the signal and the background hypothesis are tested a prior. In order to avoid bias analysis, the dark matter data were blinded from 2-100 PE in S1 by keeping only the upper 90% of the signal region. As it is shown, the benchmark region was limited to an upper threshold of 30.5 KeV (20 PE) chosen to optimize the signal to background ration. The slight impact of the S2>150 PE threshold cut, indicated by the dashed-dotted blue curve, can be observed. Finally, the signal was also restricted by a lower border running along 97% NR quantile (dashed blue curve).

2.3 Analysis

The data obtained at the end of the previous section, after an analysis that is presented now, comprises the science data input for the proposed framework in this work.

2.3.1 Analysis data

From the specified results attained in Fig. 2.15 and given that the NR and ER event signals are distinguishable by the S2/S1 ratio, one begins the analysis by focussing on the data located in the ER event distribution region as shown in Fig. 2.16 (Top), where in order to reject anomalously high events, the signal candidates are required to be inside a 2σ band around the $\log_{10}(S2_b/S1)$ median [14]. Along with this event distribution, the combined acceptance of all selection cuts for ER events is evaluated and presented on calibration data as shown in Fig. 2.16 (Bottom).

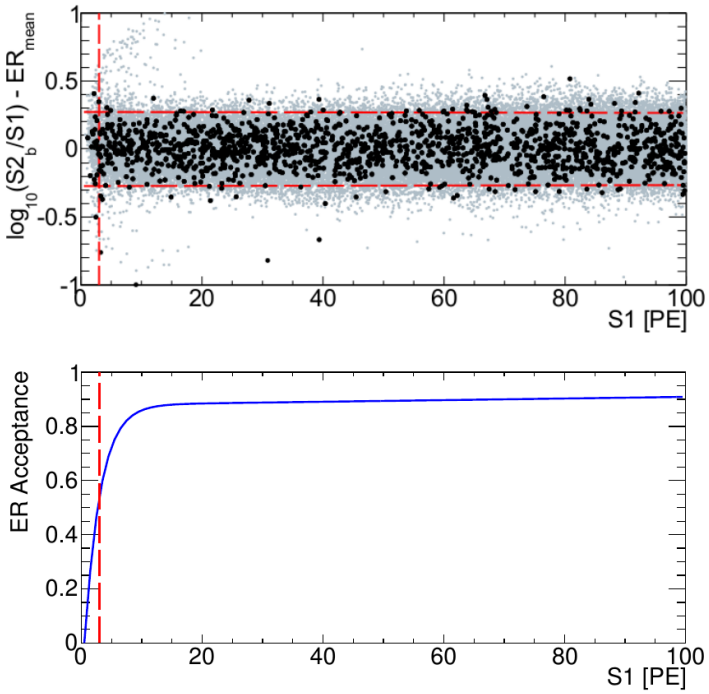

Fig. 2.16 (Top) Event distribution in the flattened $\log_{10}(S2_b/S1)$ vs. S1 space for science data (black points) and calibration (grey points). Here the straight dashed lines show the signal candidates requirement for events to be inside a 2σ band around the $\log_{10}(S2_b/S1)$ median (horizontal red lines) and the 3 PE threshold cut (red vertical line). (Bottom) Global acceptance for electronic recoil events, evaluated on calibration data Taken from [16].

The energy equivalent deposited by each interaction is obtained by using the observed S1 signal. In order to do so, a NEST model[12] (v0.98) [71] that performs the conversion from KeV-PE is incorporated[13]. As presented in Fig. 2.17, the conversion from energy deposition

[12] Stands for Noble Element Simulation Technique (NEST), a comprehensive, accurate and precise simulation of the excitation, ionization and corresponding scintillation of electroluminescence processes in liquid noble elements.

[13] NEST takes into account the scintillation efficiency relative to the 32.1 KeV transition of ^{83m}Kr at zero electric field and the quenching factor $Q(E)$ for a non-zero electric field, [18].

E to the observed signal n^{exp} in PE, is defined as:

$$n^{exp}(E) = R(E) \times Q(E) \times f \times E = L_y(E) \times E,$$

where $f = 3.76$ PE/KeV is the factor from the XENON100 light yield at 32.1 KeV. As expected, the slope of this plot takes basically the values of PE into KeV.

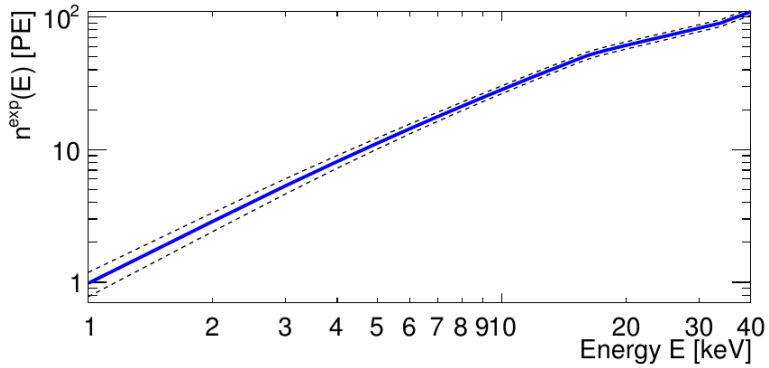

Fig. 2.17 Conversion function between energy recoil S1 in terms of PE and keV. Here n^{exp} is the central value and it's $\pm 1\sigma$ uncertainty is indicated with solid blue and black dashed line, respectively. Taken from [16].

In order to model the fundamental sources producing the majority of the background events from gamma scattering off atomic electrons of the LXe target and from intrinsic beta-background, belonging to ^{222}Rn and ^{85}Kr, ^{60}Co and ^{232}Th, calibration data was used. The total spectrum was then analytically parametrized by using a modified Fermi function $f_b(S1)$, and the result of this background model is presented in Fig. 2.18:

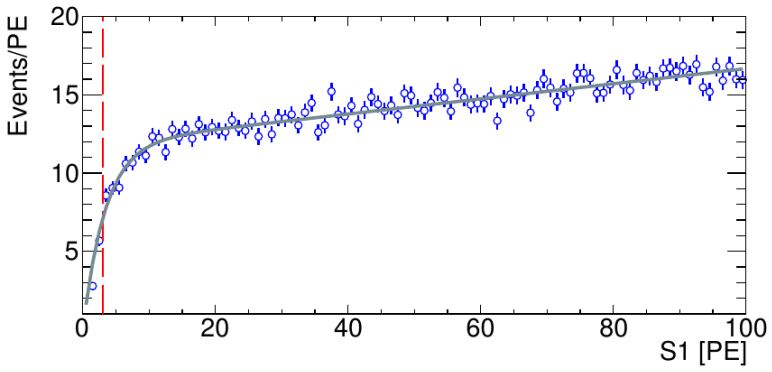

Fig. 2.18 Background model defined by $N_b \times f_b$ (grey line), scaled to the correct exposure, as explained in the text. The analytic function Fermi function f_b is based on the ^{60}Co and ^{232}Th calibration data (empty blue dots). The 3 PE threshold is indicated by the vertical red dashed line, taken from [16].

Here, the spectrum is scaled to the science data exposure by normalizing it to the number of events seen outside the signal region in order to avoid biases, [16].

2.3.2 Results

The spectrum of the remaining 393 events, between 3 and 30 PE and after all the selection cuts, is shown in Fig. 2.19 (Top) as a function of S1. Here, the background model is scaled to the correct exposure, $N_b \times f_b$, the product of the search region N_b and the normalized background probability distribution function f_b.

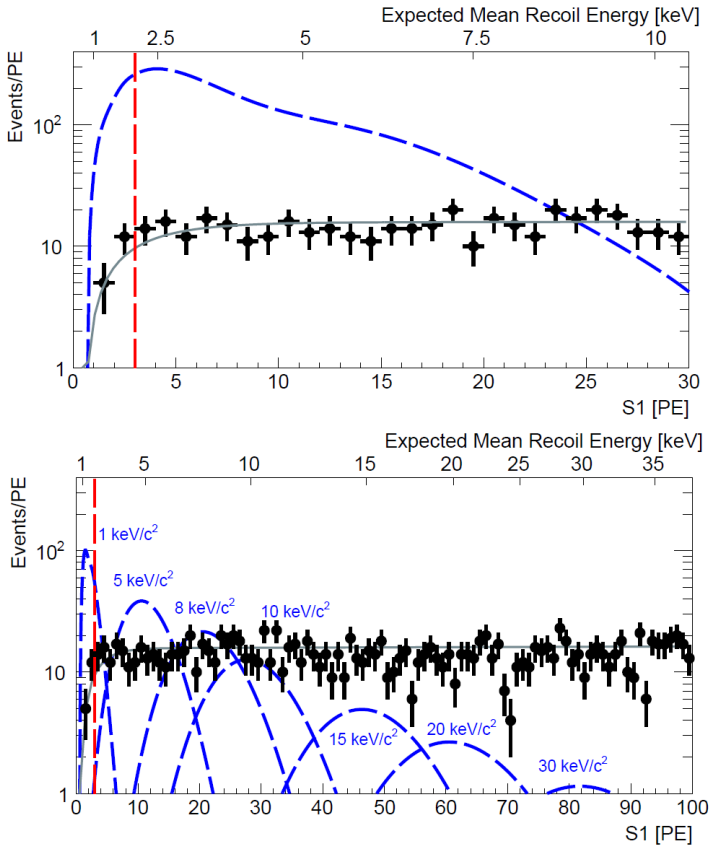

Fig. 2.19 Event distribution of the data (black dots), and background model (grey). (Top) The spectrum of the remaining 393 events, between 3 and 30 PE after all the selection cuts (Bottom) Event distribution in the region between 3 and 100 PE (black dots). Here, the grey line shows the background model used for the PL function. The red dashed line indicates the S1 threshold, taken from [16]).

The data is compatible with the background model, and no excess is observed for the background only hypothesis.

Chapter 3

Framework

This work focuses on signals coming from dark matter recoiling against electrons bound in atoms, emphasizing the practical possibility to detect and analyze the energy released in DM-electron inelastic scattering processes.

Before hand, two aspects of this DM-electron scattering are known to affect the phenomenology of such signals. First, given that the scattering event is inelastic, for an electron scattering event to occur, the minimum velocity that the dark matter must have to excite the electron depends on the bound-state energy of the electron, which in turn depends on the detector target[1]. Because of this, experiments are not as sensitive to lower dark matter velocities. Secondly, the detection rate depends on a ionization form-factor, which describes the likelihood that a given momentum transfer results in a particular electron recoil energy. This form factor can be challenging to calculate, as it depends on the wave function of the scattered electron. This ionization form factor is target-dependent and shapes the energy dependence of the event rate [49].

This chapter presents the formalism of this proposal, presenting in the context of direct detection the needed formulae to calculate electron-scattering event rates for atomic materials, which is achieved by means of analysing ionization in them.

3.1 Basic Scheme

As starting point, it is assumed that dark matter particles scatter through direct interactions with atomic electrons, as illustrated in Fig. 3.1. When the incoming dark matter scatters an

[1] Inelastic scattering events in the context of nuclear excitations have also been explored [33], as well as dark matter scattering to an excited state [73].

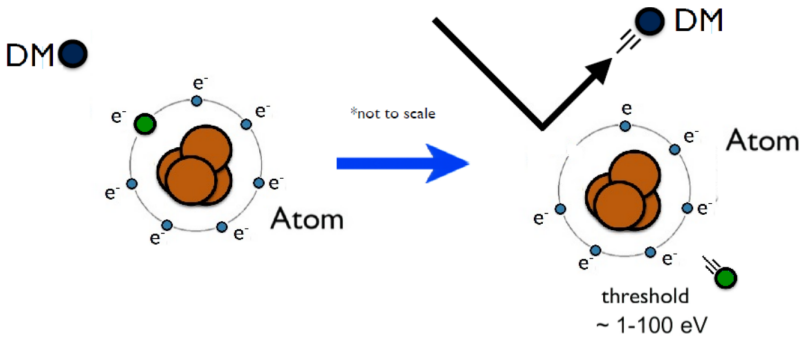

Fig. 3.1 Dark Matter inducing electronic recoils via inelastic scattering processes against electrons bound in atoms.

atomic electron, the whole energy in the process is absorbed by the electron, which can be kicked out of the atom or excited to another energy level; depending on the binding energy of the given scattered electron.

One considers that If the atom is ionized by the DM-electron interaction, the final state consists of the recoil dark matter, the escaping electron and the remaining nucleus. For simplicity in the calculations, it is recommended to model the nuclear final state as a plane wave and unlike standard references [21, 47, 28], the electron inside the atom should not be treated as being effectively free, but instead one considers the presence of a binding potential acting on the target electrons.

Due to the presence of the charged nucleus, the resulting electron wavefunction gets deformed, resulting in a deviation from a simple wavefunction of a scattered electron. This deformation reflects itself by enhancing the cross-section. As a whole, this effect can be approximated by combining a plane wave final state with a moment-dependent enhancement-factor. This factor can be understand as the Fermi-factor considered in the standard treatment of beta decay [53], or in the context of the Sommerfeld enhancement [69], but related to an outgoing state instead of an incoming one.

Formally, this atomic form factor can be found in exactly solving the Dirac equation for a free electron in presence of a Coulomb potential, and then comparing the solution to that of a plane-wave, taking as final form:

$$F(q, Z_{eff}) = \frac{2\pi\eta}{1 - e^{2\pi\eta}}, \qquad \eta = Z_{eff}\frac{\alpha m_e}{p}, \tag{3.1}$$

where Z_{eff} is the effective charge felt by the escaping electron.

In principle, the kinematics of the inelastic process by which an atomic electron is ionized by dark matter is more complicated than the one of dark matter-nuclear elastic scattering, given that the bound electron does not carry a fixed momentum, i.e., as a result of the uncertainty in its initial momentum, the bound electron may escape with a given momentum p after receiving any momentum transfer q. As a consequence, the scattering process can take place with any momentum transfer q between the initial and final dark matter state.

Nonetheless, for the regions of the phase space where q deviates too far from the typical size q_0, associated with the atomic process, there is a significant penalty. If for example $q = |\mathbf{q}|$ is too far above the inverse Bohr radius, the scattering rate receives a strong wavefunction suppression arising from the fact that it is unlikely for the atomic electron to be found with such a high momentum, as illustrated by Fig. 3.2. The relevant momentum

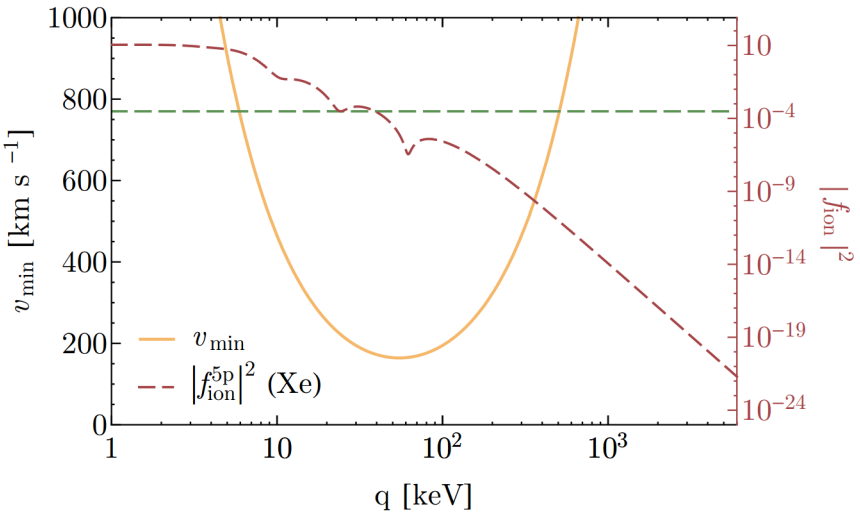

Fig. 3.2 Integration range in the rate computation including values of the momentum transfer q for which v_{min} dips below the Earth-frame escape velocity ($v_{min} = 770$ km/s, dashed green line), along with the ionization form factor $|f_{ion}^{nl}(k',q)|^2$ (with scale on the right) suppression relation against q. The Form factor illustrated is for 100 MeV DM scattering off a 5p shell Xenon electron, taken from [74].

transferred is significantly smaller than the nuclear masses considered, meaning that the nuclear recoil energy does not significantly contribute to energy conservation[2] [74]. For this

[2]Since the typical size of the dark matter velocity is $10^{-3}c$, the transitions in which $\Delta E_B \gtrsim 10^{-3} q_0$ receive a suppression relative to free electron scattering.

reason, energy conservation reads:

$$(\mathbf{p}_\chi + \mathbf{q})^2 = \mathbf{p}_\chi^2 - 2m_\chi(|E_B^{nl}| + E_R), \tag{3.2}$$

where E_R is the electron recoil energy, E_B^{nl} is the binding energy of the bound initial state (labeled by the induces nl), m_χ is the dark matter mass, and $\mathbf{p}_\chi$ is the initial dark matter momentum. Now, for a fixed $\mathbf{q}$, the lowest dark matter speed v_{min} that can induce an electron recoil E_R is found by taking the momentum $\mathbf{q}$ to be anti-parallel to $\mathbf{p}_\chi$ [49],

$$v_{min} = \frac{|E_B^{nl}| + E_R}{q} + \frac{q}{2m_\chi}, \tag{3.3}$$

where $|E_B^{nl}| + E_R$ accounts for the total energy transferred to the electron in terms of the binding and the recoil energy contributions.

Under the assumption of dark matter interacting directly with electrons, one indicates that if the interaction is independent of the momentum transfer q, then it can be completely parametrized by the elastic cross section σ_e, the one of dark matter scattering with a free electron. In the case of a q-dependent interaction, one introduces the non-relativistic DM-electron elastic scattering cross section $\overline{\sigma}_e$, but basically with the 3-momentum transfer q fixed in the matrix element to the reference value αm_e (since it is appropriate for atomic processes), i.e.:

$$\overline{\sigma}_e \equiv \frac{\mu_{\chi e}^2}{16\pi m_\chi^2 m_e^2} \overline{|\mathscr{M}_{\chi e}(q)|^2}\big|_{q^2=\alpha^2 m_e^2}, \tag{3.4}$$

$$\overline{|\mathscr{M}_{\chi e}(q)|^2} = \overline{|\mathscr{M}_{\chi e}(q)|^2}\big|_{q^2=\alpha^2 m_e^2} \times |F_{DM}(q)|^2. \tag{3.5}$$

Here, $\overline{|\mathscr{M}_{\chi e}(q)|^2}$ is the squared matrix element for dark matter-electron scattering averaged over final and initial spin states. As specified in (3.5), this matrix element is described by the dark matter factor $F_{DM}(q)$, which has no directional dependence and can be used to determine the interaction that can take place by this means.

Although, as discussed in [74], the process of ionization always involves transferring an amount of momentum from the dark matter particle to the atomic nucleus[3], a large fraction of the initial kinetic energy associated to dark matter is transferred to a primary ionized electron,

[3]However, the cross-section for such interactions end up being suppressed by the atomic form factor momentum transfer bigger than the inverse of the Bohr radius for the concerned electron.

$E_{DM} = m_{DM}v^2/2 \approx 10$ eV (m_{DM}/20 MeV). By treating the electron from the target material as a single-particle state bound in isolated xenon atoms, it is possible to describe completely its initial state by using the numerical Roothan-Hartree-Fock (RHF) bound wavefunctions tabulated in [25], as explained in Appendix B.1.3.

3.2 Direct detection rates

When dark matter scatters with an electron bound in a energy level nl, it can ionize this electron into an unbound state having a positive energy $E_R = k^2/2m_e$, [21] [47]. By taking into account the density of unbound states, the count rate for DM-induced electron ionization events is proportional to the velocity-averaged differential ionization cross section for electrons in the (n,l) shell times the dark matter velocity:

$$\frac{d\langle\sigma^{nl}_{ion}v\rangle}{d\ln E_R} = \frac{\overline{\sigma}_e}{8\mu^2_{\chi e}}\int q|f^{nl}_{ion}(k',q)|^2|F_{DM}(q)|^2\eta(v_{min})dq. \tag{3.6}$$

Here, $\mu_{\chi e}$ is the reduced mass of the dark matter-electron system, $\overline{\sigma_e}$ is the normalized cross section that depends on a given model, such as it is the dark matter form factor $F_{DM}(q)$[4]. Also, as specified by eq (3.3), $v_{min} = (|E^{nl}_B| + E_R)/q + q/2m_\chi$ and $\eta(v_{min})$ corresponds, in the sense of $\langle\frac{1}{v}\Theta(v - v_{min})\rangle$, to the velocity distribution of dark matter in the laboratory frame, meaning that it has been taken into account the Earth's average velocity $\vec{v_E}$ through the galaxy, as explained in Appendix A.2, specified by eq (A.13). The conventional Maxwellian distribution with circular velocity $v_0 = 220$ Km/s and a hard cutoff at $v_{esc} = 544$ Km/s is used, [50].

Lastly, to completely define eq (3.6), one specifies the form-factor for ionization of an electron in the (n,l) shell as

$$\begin{aligned}|f^{nl}_{ion}(k',q)|^2 &= \frac{2k'^3}{(2\pi)^3}\sum_{\substack{nlm,\\ n'l'm'}}|\langle n'l'm'|e^{iq\chi}|nlm\rangle|^2 \\ &= \frac{2k'^3}{(2\pi)^3}\sum_{\substack{\text{degenerated}\\ \text{states}}}\left|\int d^3x\widetilde{\psi}^*_{k'l'm'}(\mathbf{x})\psi_i(\mathbf{x})e^{i\mathbf{q}\cdot\mathbf{x}}\right|^2.\end{aligned} \tag{3.7}$$

[4]This dark matter form factor may be calculated from the relevant matrix element for DM-free-electron scattering. The cases $F_{DM} = 1$ and $F_{DM} = (\alpha m_e)^2/q^2$ would represent generically heavy and light mediator models, respectively.

The sum is performed over all the final angular variables and degenerated, occupied initial states[5].

In practice, however, the computation of the unbound wavefunctions is quite difficult. One way to proceed is to approximate the outgoing electron as a free plane wave. In that case, for a symmetric atom with full shells, the form-factor reduces to

$$|f_{ion}^{nl}(k',q)|^2 = \frac{(2l+1)k'^2}{(4\pi^3 q)} \int_{|k'-q|}^{|k'+q|} kdk|\chi_{nl}(k)|^2. \tag{3.8}$$

In this expression, χ_{nl} is the radial part of the momentum-space wavefunction for the bound electron in the nl shell, normalized to $\int k^2|\chi_{nl}(k)|^2dk = (2\pi)^3$ [34]. As an example, Fig. 3.2 shows the ionization form factor for the 5p state for Xenon (dashed red)(RHF) ground-state wave functions with fixed $E_R = 5$ eV.

As crossed check for this approximation, one can make the numerical evaluation of the atomic matrix element by expanding the factor $e^{i\mathbf{q}\cdot\mathbf{x}}$ in spherical harmonics and rewriting the angular integral over the product of three spherical harmonics in terms of the Wigner-3j symbol, as explained in Appendix B.1.2. This translates to:

$$\begin{aligned}|\langle n'l'm'|e^{iq\chi}|nlm\rangle|^2 = 4\pi \int r^2 dr R_{k'l'}(r)R_{nl}(r) \sum_{L,M} j_L(qr)Y_{LM}(\theta_q,\phi_q) \\ \times \frac{(-1)^m}{\sqrt{4\pi}} \sqrt{(2l+1)(2l'+1)(2L+1)} \begin{pmatrix} l & l' & L \\ 0 & 0 & 0 \end{pmatrix} \begin{pmatrix} l & l' & L \\ m & m' & M \end{pmatrix},\end{aligned} \tag{3.9}$$

where j_L is a spherical Bessel function of the first kind and θ_q, ϕ_q are the angular components of q.

Ultimately, by introducing this result, eq (3.7) can be written as:

$$\begin{aligned}|f_{ion}^{nl}(k',q)|^2 &= \frac{2k'^3}{(2\pi)^3} \sum_{\substack{nlm, \\ n'l'm'}} |\langle n'l'm'|e^{iq\chi}|nlm\rangle|^2 \\ &= \frac{4k'^3}{(2\pi)^3} \sum_{L,M} (2l+1)(2l'+1)(2L+1) \begin{bmatrix} l & l' & L \\ 0 & 0 & 0 \end{bmatrix}^2 \\ &\times \left| \int r^2 dr R_{k'l'}(r)R_{nl}(r) j_L(qr) \right|^2.\end{aligned} \tag{3.10}$$

[5]The unbound wavefunctions are normalized to $\langle \widetilde{\psi}_{k'l'm'}|\psi_{klm}\rangle = (2\pi)^3 \delta_{ll'}\delta_{m'm}\frac{1}{k^2}(k'-k)$.

where were used the symmetry and the orthogonality relations for the $\big[...\big]$ Wigner-3J symbols. The initial state wavefunctions $R_{nl}(r)$ are given by eq (B.5). The constants value entries for this function are found in [25], or in the Appendix B.1.3, where an explanation of how to read the tabulated numerical RHF list of coefficients of the xenon wavefunction is presented.

As for the outgoing radial wavefunctions $R_{k'l'}(r)$, these are also found by numerically solving the radial Schrödinger equation with a central potential $Z_{eff}(r)/r$, where $Z_{eff}(r)$ can be determined from the initial electron wavefunction, assuming it to be a bound stated of the same potential (see Appendix B.2). Under this approach, the form-factors are numerically evaluated by cutting off the sum at large l', L once it converges, and only the ionization rates of the 3 outermost shells (5p, 5s and 4d, with binding energies of 12.4, 25.7, and 75.6 eV, respectively) are found to be relevant.

The electron recoils with energy E_R, with a differential ionization rate:

$$\begin{aligned}\frac{dR_{ion}}{d\ln E_R} &= N_T \frac{\rho_\chi}{m_\chi} F(q, Z_{eff}) \frac{d\langle \sigma^{nl}_{ion} v\rangle}{d\ln E_R} \\ &= \frac{6.2}{A}\frac{\text{events}}{\text{kg}\cdot\text{day}}\left(\frac{\rho_\chi}{0.4GeV/cm^3}\right)\left(\frac{\overline{\sigma}_e}{10^{-40}cm^2}\right)\left(\frac{10MeV}{m_\chi}\right) \\ &\times F(q, Z_{eff})\frac{d\langle \sigma^{nl}_{ion} v\rangle / d\ln E_R}{10^{-3}\overline{\sigma}_e},\end{aligned} \tag{3.11}$$

where N_T is the number of target nuclei per unit mass, A is the mass-number of the target material, and ρ_χ is the local density of dark matter. To conclude, the rate computed can be corrected by using the Fermi-factor, given by eq (3.1), when taking a slightly conservative choice $Z_{eff} = 1$, given that the outer-shell electrons dominate the total rate[6].

[6]For practical purposes, in different calculations, one can use also the fact that $d\ln E_R = \frac{1}{E_R} dE_R$, such that one can rewrite $\frac{dR_{ion}}{d\ln E_R} = \frac{1}{E_R}\frac{dR_{ion}}{d\ln E_R}$.

Chapter 4

Analysis

Summarizing up to this point, in order to understand better the overall picture when one searches dark matter in the context of direct detection, *first* one needs to acquire a "super" science data set that surpasses the most rigorous quality controls within the best experimental set up attainable (achieved by means of studying the results obtained by the XENON100 experiment, along with the data analysis performed by the X.C., as it was presented in Section 2.3). Following, one needs to define a well motivated framework containing all physical inputs of dark matter that are known to the date, which intends to link all the consistent knowledge gathered from all kind of branches of physics; from astrophysics, particle physics and cosmology, to nuclear physics and more; in order to systematically predict and understand the properties and the nature of dark matter (addressed by means of the proposal presented in Chapter 3). The overall picture is summarized in the scheme of Fig. 2.4, Chapter 2.

Now, although from the framework established so far one can obtain model independent results, given that so far one doesn't rely on any distinctive realization of an effective interaction[1], at this stage there are different useful hints than can be consider in order to extend the scope of application of this model. On one hand, one can consider the results of several experiments searching indirectly for dark matter through its annihilation via protons/antiproton and electron/positron. In PAMELA[2] for example, a satellite based experiment, there seems to be a considerable excess in the electron/positron channel that starts around 10 GeV and continues up to 100 GeV. In ATIC[3], it was found also an excess peaking around 400-500

[1] Aside from keeping the natural choice of $F_{DM} = 1$, as shown in Appendix D.1.

[2] PAMELA is a satellite particle identifier that uses a permanent magnet spectrometer along with specialized detectors, and looks to measure the abundance and energy spectra of cosmic rays electrons, positrons, antiprotons and light nuclei over a large range of energy [52].

[3] A ballon experiment collaboration that measures the flux of electrons plus positrons out to energies of the order of 1 TeV.

GeV, which also agrees with the balloon experiment PPB-BETS [72].

These excess over what is expected from cosmic rays may be related to astrophysical processes, or they could come from annihilation of dark matter coming from the galactic neighborhood. If one considers the letter as the explanation, the results found suggests that the main annihilation is to electron/positron, and *not* to hadronic final states. As discussed in [38], this could happen if dark matter doesn't annihilate directly to SM particles, but instead annihilates first into a lighter state that the proton, which in turn decays to SM states containing only leptons.On the other hand, it is clear that direct detection experiments that require DM-nucleon interactions haven't been able to report a dark matter signal and that their placed limits on DM-nucleon cross-sections are approaching the neutrino wall. However, it is important to highlight that the exclusions from these experiments are based on DM-hadron interactions, which would hints that either the dark matter does not interact in such a way, or that such interactions may be suppressed.

One standard approach that incorporates these observations is base on relaxing the constraints on the dark matter parameter space, and consists in consider an alternate framework where direct DM-hadron interactions don't occur, but instead the dark matter ends up coupling exclusively to Standard Model leptons at tree level. This approach is referred to as *Leptophilic Dark Matter* (LDM) [19]. Within the context of this work, a further specialized study on leptophilic interacting dark matter is conducted in this chapter, based in the discussions presented in [47] and [40].

4.1 DAMA/LIBRA and LDM

Proposed as an explanation for the annually modulated scintillation signal reported at 2010 by DAMA/LIBRA [28] against the absence of a signal from nuclear recoils in experiments like CDMS or XENON10, in the work presented in [47] it is consider the hypothesis that dark matter sector has no direct couplings to quarks, only to leptons, in particular to electrons. In such a framework, where dark matter recoils against electrons bound in atoms, it has to be exploited the tail of their momentum distribution given that, as explained in Appendix A.1, dark matter scattering off electrons at rest can't provide enough energy to be detected in current technologies.

4.1.1 Effective dark matter interactions

The analysis presented uses an effective field theory approach and starts by introducing an effective Lagrangian for DM-lepton interactions under the assumption that dark matter particles couple directly only to leptons, not to quarks.

The most general six four-Fermi effective interactions can be written as:

$$\mathscr{L}_{eff} = \sum_i G(\overline{\chi}\,\Gamma^i_\chi\,\chi)(\overline{\ell}\,\Gamma^i_\ell\,\ell) \quad \text{with} \quad G = \frac{1}{\Lambda^2} \tag{4.1}$$

where Λ is the cut-off scale for the effective field theory description and the sum is performed over all the Γ_χ, Γ_ℓ possible Lorentz structures that can take place (see Table 4.2 for a recount of the possibilities and Fig. 4.1 for a pictorial example of how can be generated and effective local dark matter electron interaction vertex for the effective theory to take place).

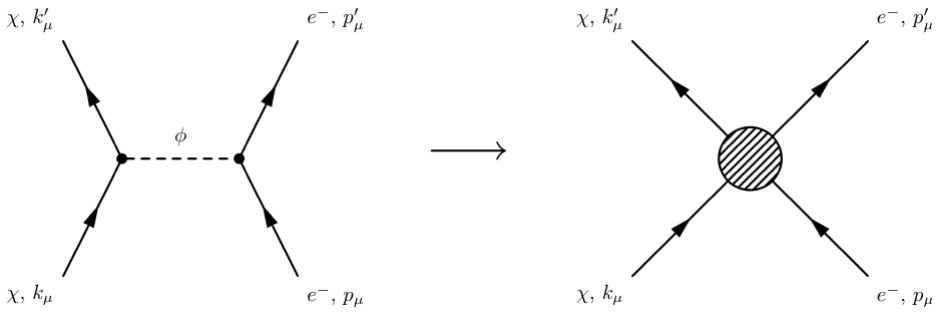

Fig. 4.1 Example of the schematics for generating an effective local DM-electron interaction (Left) analysis when the exchange of a mediator particle ϕ takes place (right) when considering an effective interaction vertex, taken from [47].

The complete set of Lorentz structures consist of:

Scalar-type:	$\Gamma_\chi = c_S^\chi + ic_P^\chi \gamma_5$	$\Gamma_\ell = c_S^\ell + ic_P^\ell \gamma_5$
Vector-type:	$\Gamma_\chi^\mu = (c_V^\chi + ic_A^\chi \gamma_5)\gamma^\mu$	$\Gamma_{\ell\chi} = (c_V^\ell + ic_A^\ell \gamma_5)\gamma_\mu$
Tensor-type:	$\Gamma_\chi^{\mu\nu} = (c_T + ic_{AT}\gamma_5)\sigma^{\mu\nu}$	$\Gamma_{\ell\chi\nu} = \sigma_{\mu\nu}$

Table 4.1 The complete set consist of scalar (S), pseudo-scalar (P), vector (V), axial-vector (A), tensor (T), and axial-tensor (AT) currents.

where $\sigma^{\mu\nu} = \frac{i}{2}[\gamma_\mu, \gamma_\nu]$[4]. Here it is assumed that the interactions induced can take place by the exchange of an intermediate particle whose mass is much larger or much smaller than the recoil momenta that it is of the order of a few MeV, see Appendix D.1.

4.1.2 Signals

As discussed in [32], when considering "leptophilic" dark matter particles interacting in a detector, there arise the different distinguishable types of signals:

- WIMP-electron scattering (WES): here the whole recoil energy is absorbed by the outer-shell electrons, resulting in them being kicked out of the atom in which are bound.
- WIMP-atom scattering (WAS): here the inner-shell electrons on which the dark matter particle scatters remains bound and the recoil is taken up by the whole atom. Specifically, this can take place elastically or inelastically[5].
- Loop-induced WIMP-nucleus scattering (WNS): lastly, even when by assumption dark matter couples only to leptons at tree level, an interaction with quarks is induced at loop level by coupling a photon to virtual leptons[6]. The diagrams that can arise at one and two-loop order are shown in Fig. 4.2. These interactions lead to the scattering of the dark matter particles off nuclei.

[4] $\sigma^{\mu\nu}\gamma_5 = \frac{i}{2}\varepsilon_{\mu\nu\alpha\beta}\sigma_{\alpha\beta}$ implies that the $AT \otimes AT$ coupling is equivalent to $T \otimes T$ and $T \otimes AT = AT \otimes T$.

[5] If the process is elastic (el-WAS), the electron wave function remains the same, whereas if it is inelastic (ie-WAS), the electrons can be excited to an outer shell remaining bound.

[6] Similar diagrams with a photon replaced by a Z^0 or a Higgs boson are power suppressed by $(k-k')^2/M_{Z^0}$ and thus negligible.

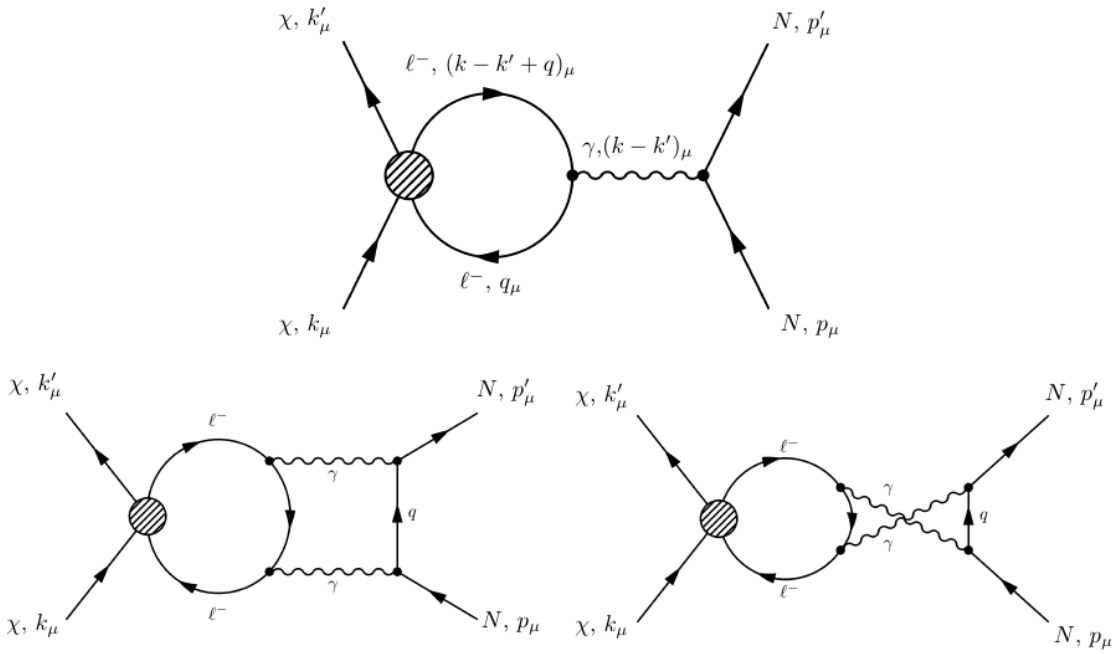

Fig. 4.2 DM–nucleus interaction induced by a charged lepton loop and photon exchange at (top) 1-loop and (bottom) 2-loops, taken from [47].

The main point of this analysis is to find when WES is the dominant mechanism taking place, given that is the expected signal for the framework of this work, and since it might explain the absence of signal in CDMS and XENON (given that these two experiments reject pure electron events by aiming to get a (close to) background free search for nuclear recoils). However, if WAS or WNS were found to be the dominant signal, then the leptophilic nature of dark matter would not help to resolve the tension between DAMA and the remaining experiments.

4.1.3 DM scattering on electrons

As mentioned before, just from kinematics, it is already known that WES is competent only when exploring the scattering off bound electrons with non-negligible momentum (see Appendix A.1). Additionally, it carries a suppression form factor from the wave function, as discussed in Section 3.1 (see Fig. 3.2). Similarly, WAS is also suppressed by the overlap of atomic wave functions of the initial and final states of the electron. As presented in

Appendix.C of [47], either for the elastic case, el-WAS, where:

$$\begin{aligned}\sum_m |\langle nlm|e^{i\mathbf{K}\cdot\mathbf{x}}|nlm\rangle|^2 &= \sum_m \int dr\, d\Omega\, r^2 [R_{nl}(r)]^2 Y^*_{lm}(\theta,\phi) Y_{lm}(\theta,\phi) e^{iKr\cos\theta} \\ &= (2l+1)\int dr\, r^2 [R_{nl}(r)]^2 \frac{\sin Kr}{Kr},\end{aligned} \tag{4.2}$$

or in the inelastic case, ie-WAS, where:

$$\begin{aligned}\sum_{mm'} |\langle n'l'm'|e^{i\mathbf{K}\cdot\mathbf{x}}|nlm\rangle|^2 = (2l+1)(2l'+1)\sum_L (2L+1)\begin{pmatrix} l & l' & L \\ 0 & 0 & 0\end{pmatrix}^2 \\ \times \left|\int r^2 dr R_{k'l'}(r) R_{nl}(r) j_L(Kr)\right|^2.\end{aligned} \tag{4.3}$$

the final suppression is of the order of magnitude:

$$\sum |\langle n'l'm'|e^{i\mathbf{K}\cdot\mathbf{x}}|nlm\rangle|^2 \sim 10^{-19}, \tag{4.4}$$

where the functions R_{nl} are given by eq (B.5) and their coefficients can be found in Appendix B.1.3. As for the final state wave functions $R_{k'l'}(r)$, one can use the hydrogen-like approximation, along with $K = |\mathbf{k} - \mathbf{k}'|$.

However, loop induced WNS does not undergo through any wave function suppression, but instead carries a loop factor. At 1-loop, for example, the suppression is of the order of $(\alpha_{em} Z/\pi)^2$, where Z is the charge number of nucleus. One can obtain a rough estimate for the ratios of WAS, WES and WNS induced rates when neglecting order-one factors and different possible v dependencies:

$$R^{WAS} \,:\, R^{WES} \,:\, R^{WNS} \sim 10^{-17} \,:10^{-10} \,:1\,. \tag{4.5}$$

From these estimations, it is clear that whenever there is a loop induced cross section, it will dominate the rate in direct detection experiments. In fact, this holds as well for 2-loop cross sections, since the suppression will have another factor $(\alpha_{em} Z/\pi)^2$ relative to the 1-loop.

In order to determine the pertinent scenario where WES is relevant, one can start by looking into the dark matter scattering on electrons at rest scattering cross section (this approximation

simplifies a lot the calculations). Assuming that all the particles are non-relativistic:

$$\begin{aligned}
\text{scalar-type:} &= \sigma = \sigma^0_{\chi e}\left\{(c_S^\chi c_P^e)^2 + \left[(c_S^\chi c_P^e)^2 + (c_S^\chi c_P^e)^2\frac{m_e^2}{m_\chi^2}\right]\frac{v^2}{2} + \frac{(c_S^\chi c_P^e)^2}{3}\frac{m_e^2}{m_\chi^2}v^4\right\},\\
\text{vector-type:} &= \sigma = \sigma^0_{\chi e}\left\{(c_V^\chi c_V^e)^2 + 3(c_A^\chi c_A^e)^2 + [(c_V^\chi c_A^e)^2 + 3(c_A^\chi c_V^e)^2]\frac{v^2}{2}\right\},\\
\text{tensor-type:} &= \sigma = \sigma^0_{\chi e}\left\{12c_T^2 + 6c_{AT}^2 v^2\right\}.
\end{aligned} \tag{4.6}$$

These are the cross sections for each Lorentz structure given to leading order, expressed in terms of two suppression factors; the velocity of dark matter in the halo $v \sim 10^{-3}c$ and the ratio m_e/m_χ. Based on these results, up to the electron mass or velocity suppression, the typical size of the scattering cross section is given, as calculated in Appendix D.2 and showed in the result found in eq (D.29), by:

$$\sigma^0_{\chi e} = \frac{\overline{|\mathscr{M}_{V\pm A}|^2}\Big|_{\mathbf{p}=0}}{16\pi m_\chi^2} = \frac{16G^2 m_\chi^2 m_e^2}{16\pi m_\chi^2} \equiv \frac{G^2 m_e^2}{\pi} = \frac{m_e^2}{\pi\Lambda^4}. \tag{4.7}$$

The results of eqs. (4.6) and (4.7) are summarized in the Table 4.2, along with the results that can be obtained as well at loop level when considering the calculation of the 1-loop and 2-loop cross sections for dark matter scattering on a nucleus, see Section II.B from [47].

	Fermionic Dark Matter		
$\Gamma_\chi \otimes \Gamma_\ell$	$\sigma(\chi e \to \chi e)/\sigma^0_{\chi e}$	$\sigma(\chi N \to \chi N)/\sigma^1_{\chi N}$	
$S \otimes S$	1	α_{em}^2	[2-loop]
$S \otimes P$	$\mathscr{O}(v^2)$	-	
$P \otimes S$	$\mathscr{O}(r_e^2 v^2)$	$\alpha_{em}^2 v^2$	[2-loop]
$P \otimes P$	$\mathscr{O}(r_e^2 v^4)$	-	
$V \otimes V$	1	1	[1-loop]
$V \otimes A$	$\mathscr{O}(v^2)$	-	
$A \otimes V$	$\mathscr{O}(v^2)$	v^2	[1-loop]
$A \otimes A$	3	-	
$T \otimes T$	12	q_ℓ^2	[1-loop]
$AT \otimes T$	$\mathscr{O}(v^2)$	$q_\ell^2 v^{-2}$	[1-loop]

Table 4.2 Cross section σ suppression by small parameters for WES and WNS for all possible Lorentz structures, where $r_e = m_e/m_\chi$.

The results shown in Table 4.2 imply that whenever WNS at 1-loop or 2-loop is generated, it will be the dominating signal in direct detection experiments. However, in the $A \otimes A$ coupling where no DM-nucleus loop interaction is induced, it is found simultaneously that the WES cross section is not suppressed by any term.

This analysis leads to chose the $A \otimes A$ coupling as the representative scenario where WES will dominate the event rate and will be relevant. Section 5.3 will present the results from this choice and the corresponding implications.

4.2 LDM in lepton interactions at LEP and ILC

Although direct detection searches (aiming to observe interactions between dark matter and atomic nucleus), along with indirect detection searches (scanning the astrophysical sky for unexplained fluxes product of dark matter annihilation or decay) are the most well known searches of dark matter, particle colliders on the Earth play an important role likewise.

In the particle collider context, since WIMPs are expected to be neutral and weakly interacting, the strategy to detect them relies on producing particles in combination with the dark matter candidates (leptophilic models stem from searches for mono-photon events, such as the characteristic signature $e^+e^- \to \chi\chi\gamma$). If dark matter can be produce directly, one possibility is to use the state of radiation, such as photons or gluon jets, that would recoil against the WIMPS [31]. The idea has been explored at the Large Electron-Positron collider (LEP), and their data has been reanalyzed to reinterpret and to determine the corresponding constraints [37]. A same approach has been thought to be conducted at the International Linear Collider (ILC),using mono-photon events in a non-relativistic approximation [22], which with a center of mass energy of 500 GeV - 1 TeV would improve the constraints. In addition, similar signatures have been studied at the Large Hadron Collider (LHC) and at the Tevatron, using mono-jet signals [75]. In general, the specific bounds depend on the mass, spin and couplings of the dark matter particles and the exchanged particles that mediates the iteractions between the SM and the dark matter particles.

In the work presented in [40], limit bounds from the analysis of four-lepton contact interactions contributing to the process $e^+e^- \to \ell^+\ell^-$, being $\ell = e,\ \mu,\ \tau$, are studied and discussed, comparing them to the limits expected from the ILC.

4.2.1 Model

In order to produce dark matter at LEP it must couple to electrons, therefore this study uses a model-independent framework where the SM is extended by a single dark matter field and a single heavy mediator[7]. In principle, the phenomenology of these processes can be described in an effective field theory where it is assumed that the dark matter particles can only interact with the SM leptons.

To properly define the framework for this leptophilic dark matter, one starts from different fundamental theories [2] with established renormalisable interactions between SM fermions and dark matter particles, considering the exchange of a heavy mediator. From them, effective 4-particle-vertices can be deduce and by working with effective operators, it is possible to infer different information related to the effective couplings and to extend this information to the parameters of the underlying fundamental theory.

Starting with the list of fundamental Lagrangian from [2] and using the path integral formalism approach from [Haba et al.], a full list of viable models along with the form of their interactions is summarized in Table 4.3. In these models one introduces the dark matter particle denoted as χ, along with a mediator particle denoted as η. The spins of χ and η are specified by the letters "S" (scalar), "F"(fermion) and "V" (vector) (corresponding to 0, 1/2 and 1). Given that in some models η will appear either in the s- or t- channel of the annihilation diagram $\chi\chi \to \ell^+\ell^-$, e.g. if η is a bosonic mediator, the t-channel mediation will be denoted by "tS" or, "tV", and the same notation will be used for the s-channel.

Additionally, in order to limit the size of the parameter spacer, given that the full range of parameters leads to an excessive amount of scenarios, this analysis restricts to specific benchmark models with constraints on the individual couplings (see Table 4.3). The effective coupling constant G for each model is defined as $G \equiv g_i g_j / M_\eta^2$ Lastly, it is assumed that the mediator η couples to leptons of all generations with the same strength, but the coupling with the SM quarks remains as zero.

[7] In this context, heavy in comparison to the the e^+e^- center of mass energy, so the mediator is usually assumed to be too heavy to be produced directly at the ILC, and therefore can be integrated out.

DM χ	Med η	Diagram	Coupling to SM $(-\mathscr{L}_{\text{int}})$	Benchmark Scenarios
S	S	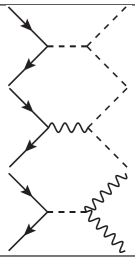	$g'\chi^{\dagger}\chi\eta + \overline{\psi}(g_s + g_p\gamma_5)\psi\eta$	$g_p = g'_p = 0$ (scalar) $g_s = g'_s = 0$ (pseudoscalar)
F	S		$\overline{\chi}(g'_s + g'_p\gamma_5)\chi\eta + \overline{\psi}(g_s + g_p\gamma_5)\psi\eta$	
V	S		$g'\chi_\mu\chi^\mu\eta + \overline{\psi}(g_s + g_p\gamma_5)\psi\eta$	
S	V	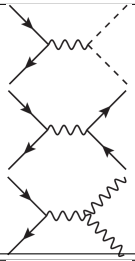	$g'\chi^{\dagger}\overset{\leftrightarrow}{\partial_\mu}\chi\eta^\mu + \overline{\psi}\gamma_\mu(g_v + g_a\gamma_5)\psi\eta^\mu$	$g_a = g'_a = 0$ (vector) $g_v = g'_v = 0$ (axialvector)
F	V		$\overline{\chi}\gamma_\mu(g'_v + g'_a\gamma_5)\chi\eta^\mu + \overline{\psi}\gamma_\mu(g_v + g_a\gamma_5)\psi\eta^\mu$	
V	V		$ig'(\eta_\mu\chi^{\dagger}_\nu\chi^{\mu\nu} + \chi_\mu\eta_\nu\chi^{\dagger\mu\nu} + \chi^{\dagger}_\mu\chi^\nu\eta^{\mu\nu})$ $+\overline{\psi}\gamma_\mu(g_v + g_a\gamma_5)\psi\eta^\mu$	
S	F	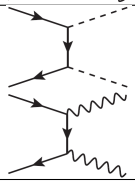	$\overline{\eta}(g_l P_L + g_r P_R)\psi\chi + h.c.$	$g_l = 0$ (right-handed) $g_r = 0$ (left-handed)
V	F		$\overline{\eta}\gamma_\mu(g_l P_L + g_r P_R)\psi\chi^\mu + h.c.$	
F	tS	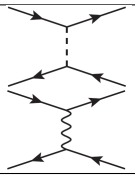	$\overline{\chi}(g_l P_L + g_r P_R)\psi\eta + h.c.$	$g_l = 0$ (right-handed) $g_r = 0$ (left-handed)
F	tV		$\overline{\chi}\gamma_\mu(g_l P_L + g_r P_R)\psi\eta^\mu + h.c.$	

Table 4.3 List of models involving a dark matter field χ, a mediator η and a standard model lepton ψ. The fields have the associated spin 0,1/2 or 1, denoted by S(calar), F(ermion) and V(ector), respectively. Here $P_{L,R} = (1 \pm \gamma_5)/2$ is used to project onto chiral fermion states.

Chapter 5

Results

This chapter presents the agreement of the results produced by using the computational tools introduced in Chapter 3, along with the calculated direct detection limits for dark matter when considering electronic recoils as being induced by dark matter via inelastic scattering processes. The results obtained were based on the experimental results from the profile likelihood analysis of 224.6 live days$\times$34 Kg exposure of XENON100 experiment data. Additionally, in the context of the analysis presented in Chapter 4, results from a specialized study of leptophilic interacting dark matter are also presented in the scenario of Axial-Vector couplings between dark matter and leptons, where loops diagrams vanish.

5.1 Framework agreement

The starting point to analyze the scenario proposed is to determine the consistency of the computational tools that were introduce in Chapter 3. The realization of this task is done by comparing the declaration's model cross section exclusion reach for 1 kg·year of exposure of against the same calculated results published on [35] and [49]. An initial step to arrive to the comparison is to look first into the behavior of the ionization form factor $|f_{ion}^{nl}(k',q)|^2$. It is straightforward to reconstruct the same suppression effect of the ionization form factor (presented in Fig. 3.2) as it is shown in Fig. 5.1, by just using the input data from the (RHF) bound wavefunctions tabulated in [25] for the 5p shell Xenon electron along with eq. (3.7).

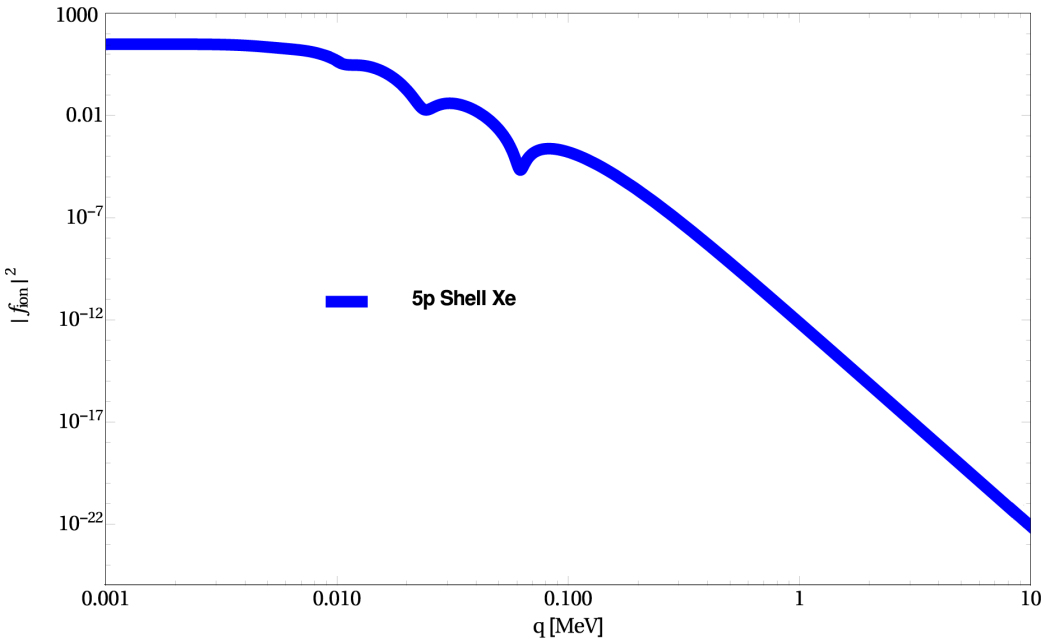

Fig. 5.1 Reproduced ionization form factor $|f_{ion}^{nl}(k',q)|^2$ suppression relation against the transfer momentum q. The Form factor illustrated in both cases stands for 100 MeV DM scattering off a 5p shell Xenon electron.

This initial agreement, within 90% in comparison to the expected results published, motivates to continue the procedure and to declare in a similar way the plane-wave final states for the scattered electrons, what in consequence grants validity to the definition used to calculate the ionization form factor for spherically symmetric full shells. For this result it is important to notice that the form factor falls steeply with the momentum recoil transfer, meaning that when the momentum $q = |\mathbf{q}|$ happens to deviates way too far above the inverse of the Bohr radius, $a_0^{-1} \approx 3.7$ keV, so it does the scattering rate given that it will end up experiencing a strong wave-function suppression from the fact that it unlikely for any atomic electron to be found with such a high momentum.

In order to proceed, the results from [35] (showed side by side in the Fig. 5.2) are considered as the ideal limits to reach. From them, 2 different verifications can be done, both the differential scattering rate dR/dE_R and the cross section exclusion limits in terms of the dark matter mass, whether for the form factor $F_{DM} = 1$ or for $F_{DM} = (m_e\alpha)^2/q^2$.

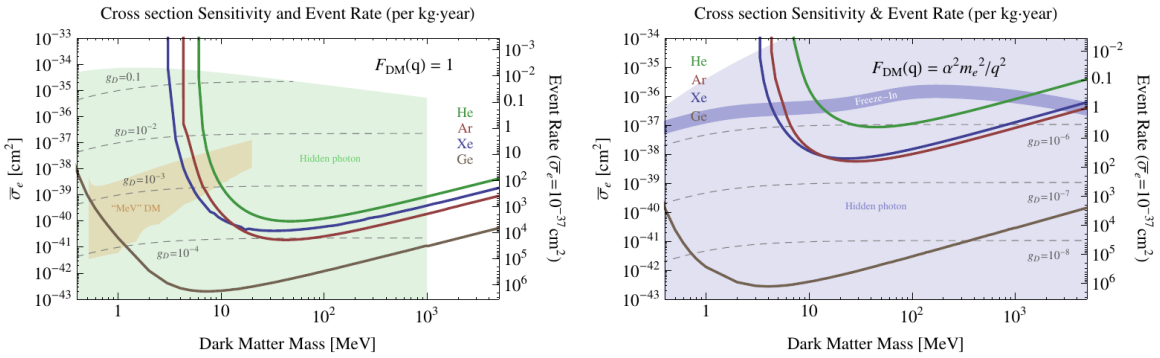

Fig. 5.2 Differential scattering rates dR/dE_R against the dark matter mass at 95% confidence level, for the form factors (Left) $F_{DM} = 1$ and (Right) $F_{DM} = (m_e\alpha)^2/q^2$ when assuming a cross section of $\overline{\sigma}_e = 10^{-37}$ cm^2, taken from [35].

First, the calculated results for both differential scattering rates dR/dE_R are shown in Fig. 5.3. The plots were produced by taking 1 kg·year of exposure while assuming only a irreducible neutrino background (which contribution is expected to be negligible for this exposure), and as indicated by taking a cross section value of $\overline{\sigma}_e = 10^{-37}$ cm^2. The agreement found for both values of F_{DM} succeeds the requirements to proceed without altering the definitions and computational approach.

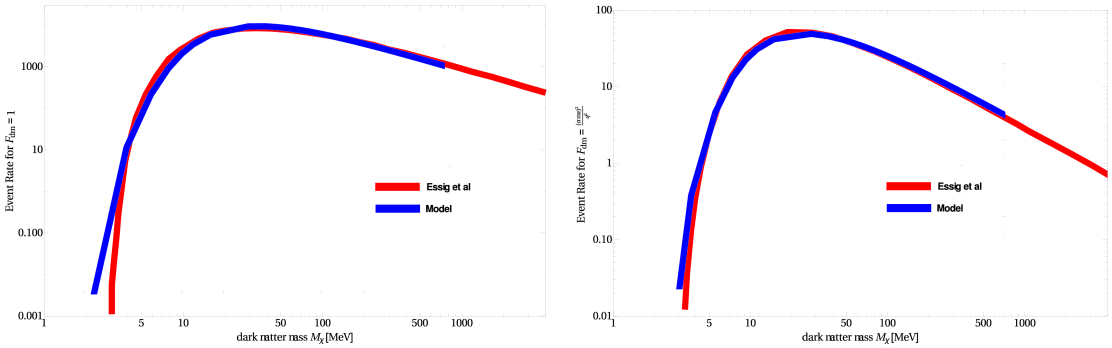

Fig. 5.3 Comparison of the differential scattering rates calculated dR/dE_R against dark matter mass at 95% confidence level, for the form factors (Left) $F_{DM} = 1$ and (Right) $F_{DM} = (m_e\alpha)^2/q^2$, when assuming a cross section of $\overline{\sigma}_e = 10^{-37}$ cm^2.

With the previous agreement reached, the following and last comparison that has to be done is the one for the cross section exclusion limits. The results are shown in Fig. 5.4, for the form factor $F_{DM} = 1$, and in Fig. 5.5 for $F_{DM} = (m_e\alpha)^2/q^2$.

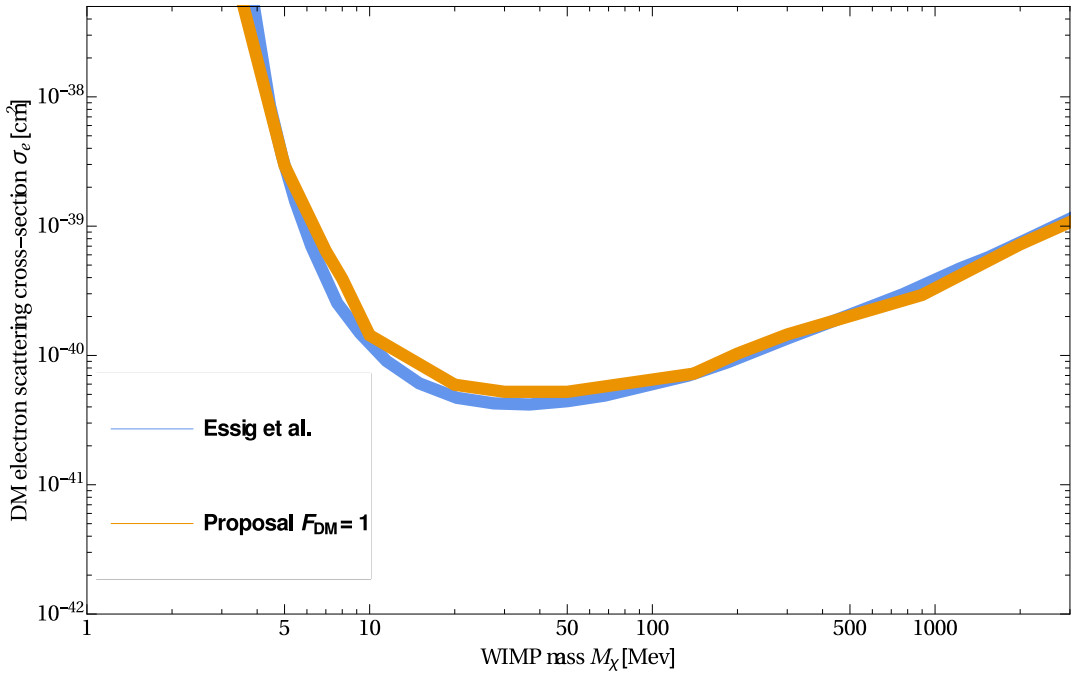

Fig. 5.4 Comparison of the expected dark matter electron scattering cross section limits at 95% C.L. for the form factors $F_{DM} = 1$.

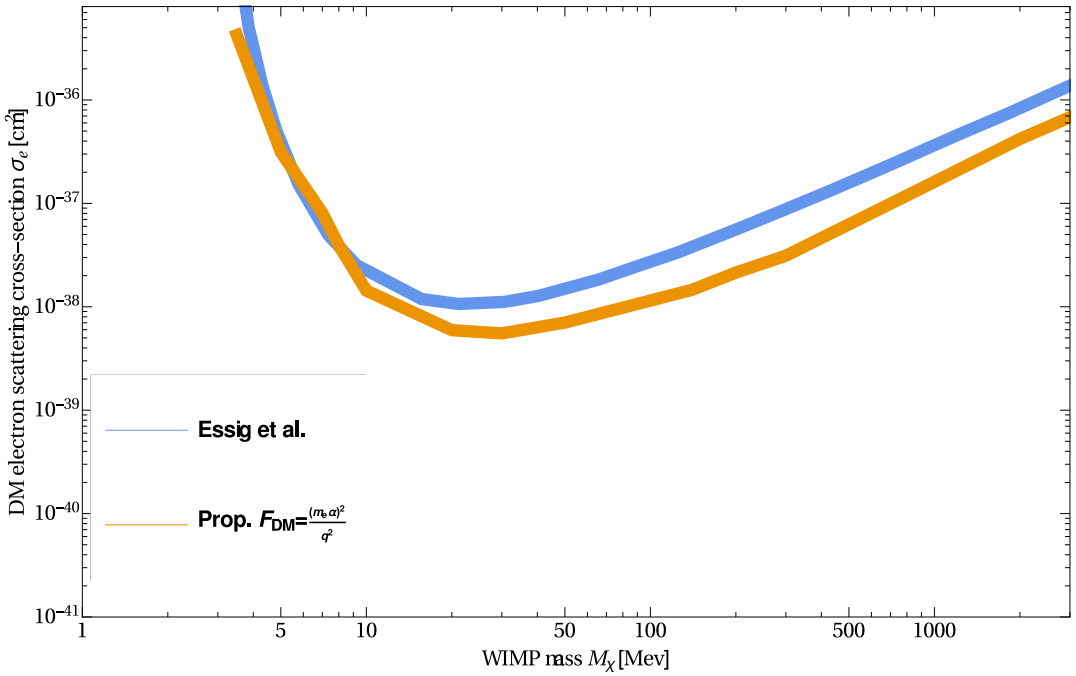

Fig. 5.5 Comparison of the expected dark matter electron scattering cross section limits at 95% C.L. for the form factors $F_{DM} = (m_e\alpha)^2/q^2$.

The set of calculated points presented for both dark matter form factors consist of 16 points. Although the agreement could have been more noticeable by taking more point, given that each point took approximately 34.1 hours for its calculation after having chosen an optimal integrative method in Wolfram Mathematica, and given that the agreement was quite noticeable for these values already, these modest amount of points is justified.

Regarding the results found, before continuing, several observations can be done. First, it is worth to notice that for small values of dark matter masses the reach falls as the energy available approaches the ionization threshold. This result suggests that typically small dark matter masses are only able to ionize $5p$ outer-shell electrons (which have a binding energy of $E_B^{5p} = 12.4$ eV). As the mass increases, it becomes more likely to continue the ionization of the remaining outer orbitals, in order first the $5s$ ($E_B^{5s} = 25.7$ eV) and/or the $4d$ ($E_B^{4d} = 75.6$ eV) shell level. Subsequently, at heavier values of mass, recoiling electrons are increasingly likely to have enough energy to produce secondary ionizations. As expected, the rate decreases for larger mass values, as the cross section saturates and the reach falls linearly with the decreasing number density.

As results from this section, the consistency of the computational tools developed was check to be successful and a further implementation was not just well motivated but completely justified.

5.2 Model-independent

The implementation of the tools developed within the context of the published results from the analysis of 224.6 live days$\times$34 Kg exposure made by the XENON100 Experiment begins by calculating the differential ionization rate against the electron recoil energy, including the acceptance of the experiment, for different values of the mass (such as $m_\chi =$ 1 Gev, 10 Gev, 100 Gev, 1 TeV.), for $F_{DM} = 1$. The idea is to vary the values of $\overline{\sigma}_e$ in order to find where the rate is above the background profile model presented (blue dashed lines), when looking to the right of the threshold cut point of 3 PE (around 2 KeV). Fig. 5.6 shows the plot for the assumed value $\overline{\sigma}_e = 10^{-32}$ cm^2, as example, such that the rate of all the masses are above the background profile.

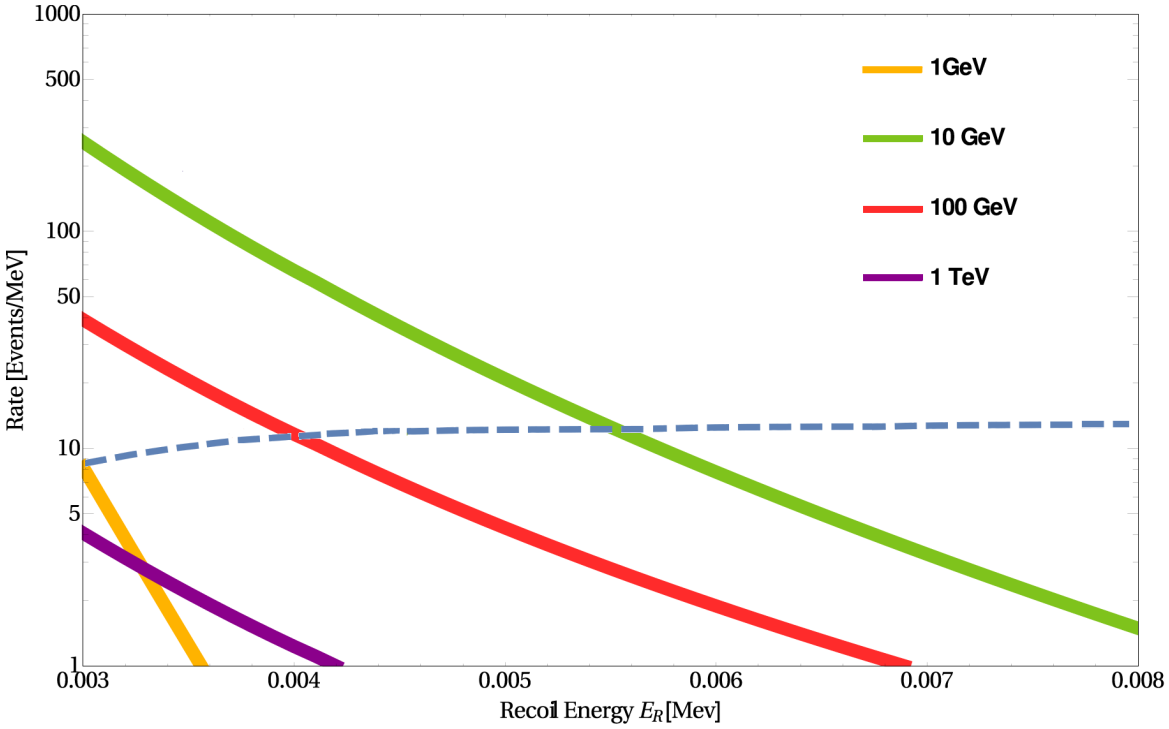

Fig. 5.6 Differential rate versus electron recoil energy for different values of the values $m_\chi =$ 1 Gev, 10 Gev, 100 Gev, 1 TeV.

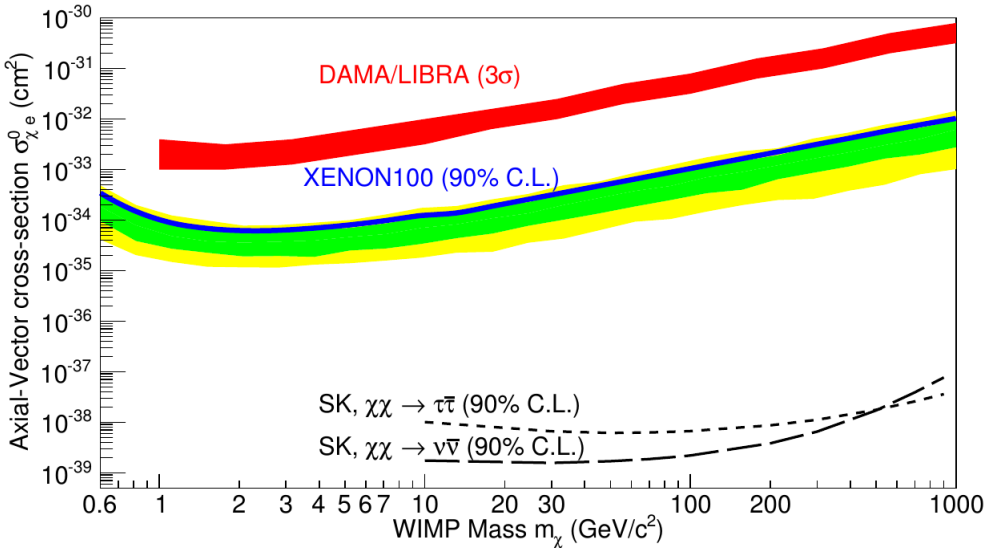

Fig. 5.7 XENON100 upper limit at 90% C.L., indicated by the blue line along with the green/yellow bands that indicate the 1σ and 2σ sensitivity, taken from [17].

After obtaining a slight idea of the order of magnitude needed for $\overline{\sigma}_e$ to surpass the condition of the background profile, one can based the subsequent analysis having as reference

the XENON100 X.C. limits published in [17], see Fig. 5.7. A further estimation of the exclusion limits is presented in Fig. 5.8, done by fixing the value of the electron recoil energy to 3 PE[1].

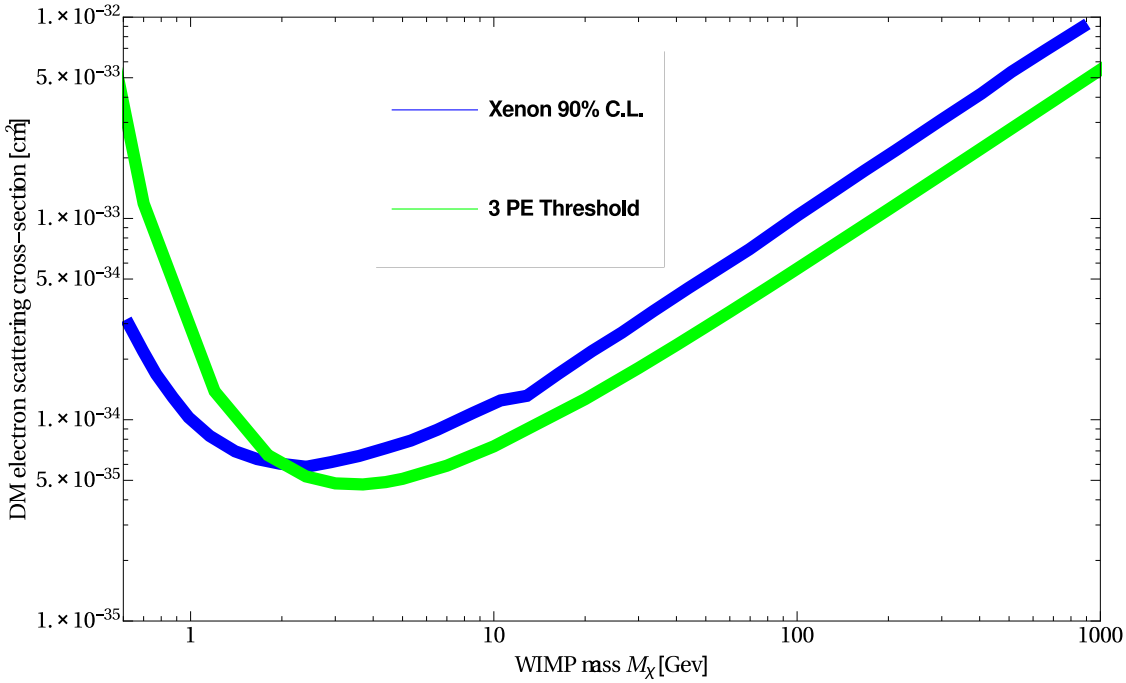

Fig. 5.8 Estimated scattering cross section limit results against dark matter mass, for a 3 PE threshold energy value against the cross section limits established by the X.C.

This evaluation indicates in principle how robust can one get limits of exclusion when considering electron recoil in the context of the XENON100 estimated background. However, the realization of a cross section exclusion limit under their experimental data under a specified confidence level has to be performed by using, as explained in Appendix C.2, a Pearson's chi-squared test, which would implement in a proper manner the data of interest, found it to be from Fig. 2.19, the data results after the threshold cut . By introducing an effective χ^2 hypothesis test for 5 degrees of freedom at 90 % confidence, the results of a model independent analysis are shown in Fig. 5.9.

[1]The threshold cut of 3 PE energy is chosen motivated by the connection to the DAMA/LIBRA signal, as explained in [17], such that the reasonableness and sturdiness of the results can be put to the test still keeping $F_{DM} = 1$.

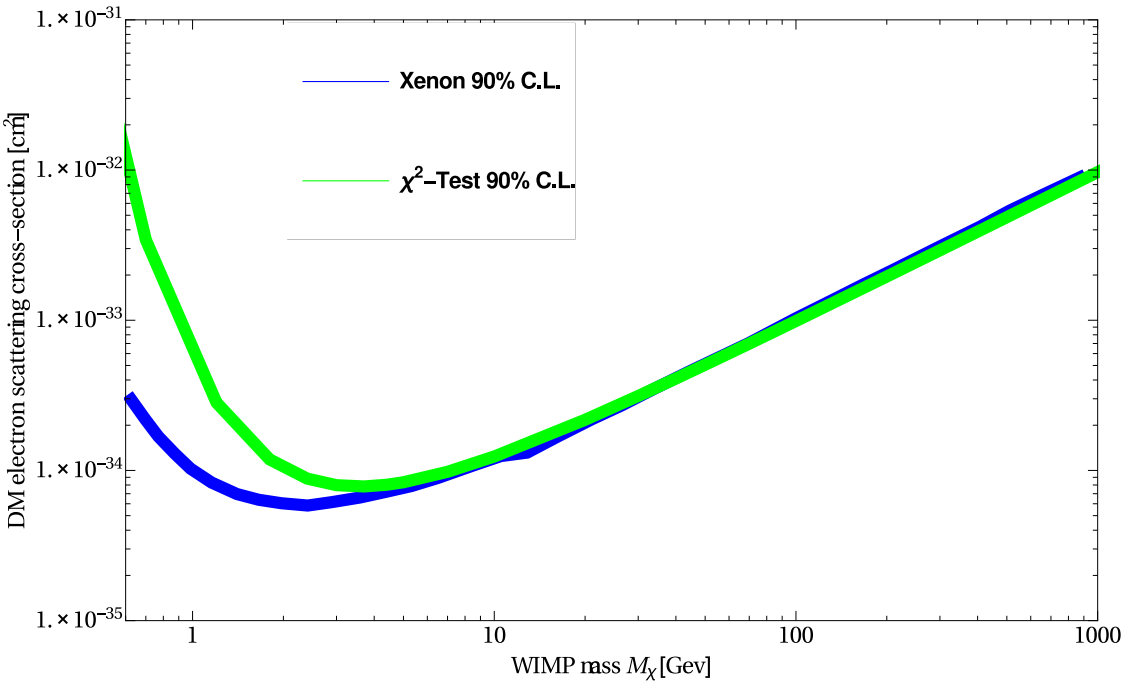

Fig. 5.9 Predicted scattering cross section limit results against dark matter mass, based on the experimental results from the profile likelihood analysis of 224.6 live days$\times$34 Kg exposure of XENON100 experiment data, produced by employing a χ^2 hypothesis test at 90 % C.L. against the cross section limits established by the X.C.

Here it is important to indicate that the result from the X.C., based on the calculations presented in [47], differ from the result of the proposal developed at low values of mass given that the electron inside the atom considered is incorrectly treated as being free after the scattering. The proposal considers the binding energy of the electrons along with the binding potential on the recoiling electron dropped. This affect influences the scattering rate for relatively low recoil energies, explaining the slightly differences on the shape on the results. Nevertheless, the agreement seems to be favorable and the match is almost superb at higher masses.

Lastly, as an indication, all procedures and methods used to calculate all the results showed in this sections are extensively described in the Appendix B.2 and can be found in the Mathematica notebook used.

5.3 DAMA/LIBRA and LDM

As previously discussed, there is no proposed standard model explanation for the DAMA signal, since it is found that all calculated modulation amplitudes are much too small to explain it. In order to try to conciliate leptophilic dark matter with DAMA, in the context of the $A \otimes A$, one start noticing that the interactions WIMP-nucleus scattering is absent, so the dominant signal is the less suppressed one coming from the WIMP-electron scattering along with much weaker signal (negligible) coming from inelastic WIMP-atom scattering. In order to proceed one needs to perform a fit of the DAMA data for the event rate for WES (this has been already done in [47]). From this at their best fit, the predicted modulated and unmodulated DAMA event rates are presented in Fig. 5.10. The study performed using the data from 2–8 keV showed that the spectral signal shape of the modulated signal strongly disfavours this scenario, given the bad fit around $\frac{\chi^2}{dof} = 55.9/10$ (corresponding to a probability of 2×10^{-8}), so as an improvement the first bin of data was dropped, achieving $\frac{\chi^2}{dof} = 20.6/10$, which corresponds to a probability of 1.4%.

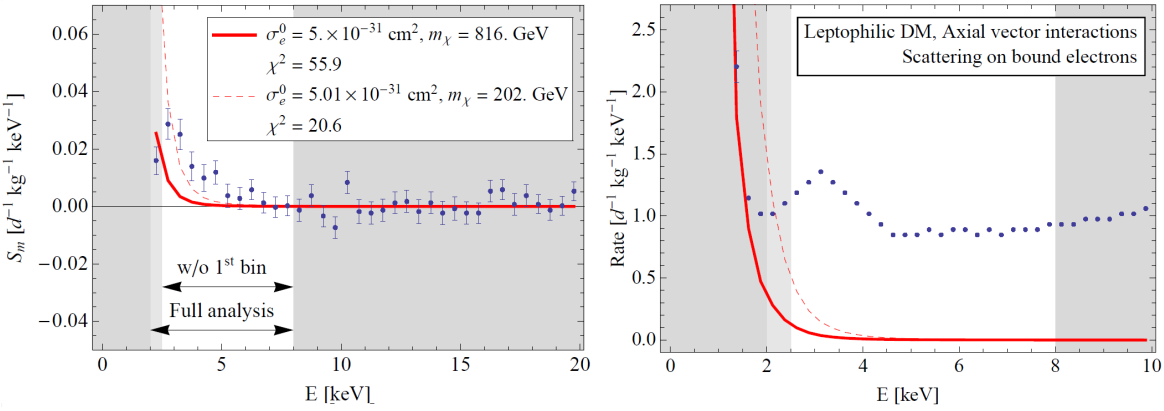

Fig. 5.10 Expected spectrum for the modulated (Left) and unmodulated (Right) event rate in DAMA at the best fit point when one assumes WIMP–electron scattering resulting from axial vector-like DM–electron couplings. Here the solid curve has been fitted to the DAMA data from 2–8 keV, while for the dashed curve, the first energy bin has been neglected. Taken from [47].

Ignoring the problem of the spectral fit, one can analyze the allowed region in the plane of m_χ and $\sigma_{\chi e}$ relative to the best fit. The produced signal from DAMA is shown in Fig. 5.13 along with the results calculated by the X.C. and with the results produced in this work.

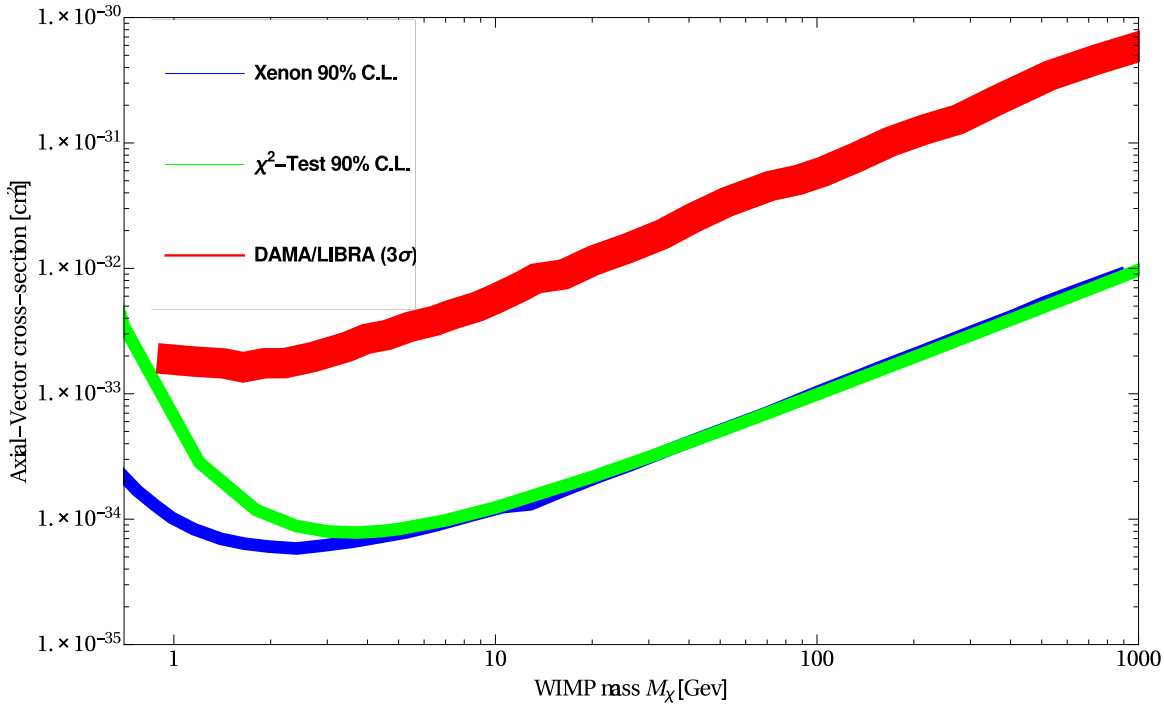

Fig. 5.11 Conciliation of leptophilic dark matter model when having an Axial-Vector coupling with the results of DAMA/LIBRA and the X.C.

According to this, WES has several problems to explain the spectral shape of the modulated and unmodulated component of DAMA. In fact, this class of model completely rules out DAMA/LIBRA results.

Furthermore, in the context of the results obtained by this proposal, it can be observed that at very large cross sections

$$\sigma_{\chi e} \sim 10^{-33} cm^2 \times (\frac{m_\chi}{100\ GeV}),$$

for $m_\chi \gtrsim 10$ GeV. From the observation from Table 4.2 and eq. 4.7, one can find that to realize a cross section with a similar order of magnitude, a low scale for physics of $\Lambda \lesssim 0.12$ GeV would be required[2] (the scale dependence on m_χ is plot along the results to illustrate this better in Fig. 5.12).

[2]Allowed only if there is no $\chi\chi \to \tau\overline{\tau}, \nu\overline{\nu}$.

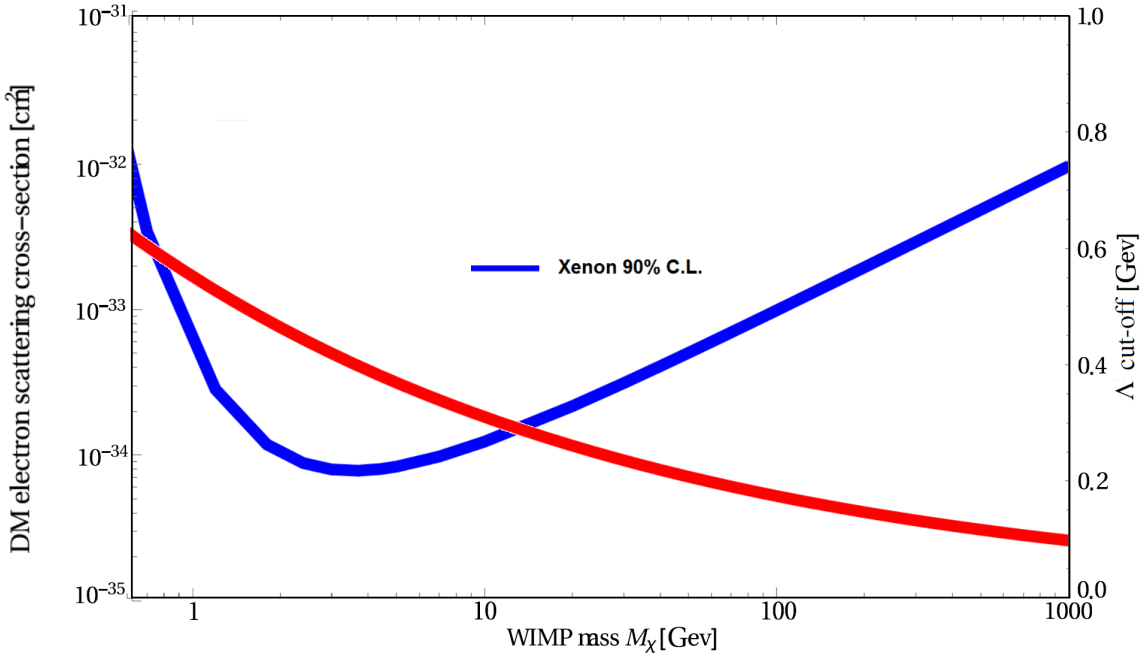

Fig. 5.12 Leptophilic dark matter model results when having an Axial-Vector coupling along with the scale dependence for the effective field theory description.

This procedure provides a lower bound on Λ in order to describe the interactions when using a effective theory approach.

5.4 LDM in lepton interactions at LEP and ILC

As presented in [40], from the list of simplified models presented in Table. 4.3, foremost the first models are characterized because dark matter annihilation is mediated by the exchange of a scalar or vector boson, which leads to a tree-level contribution to the four lepton processes $e^+e^- \to \ell^+\ell^-$. The bounds from the four-lepton interactions at LEP on these models, when considering a spin-1 mediator at 90 % C.L., are for the relevant case of this study (axial-vector case)[3]:

$$\begin{aligned} \frac{g_a}{M_\eta} &< 2.4 \times 10^{-4}\ GeV^{-1} \quad \text{for } M_\eta > 200\ GeV \\ \frac{g_a}{M_\eta} &< 6.9 \times 10^{-4}\ GeV^{-1} \quad \text{for } 100\ GeV\ < M_\eta < 200\ GeV. \end{aligned} \tag{5.1}$$

These bound are found to be independent of the dark matter mass m_χ.

Next, the exclusion bounds at 90 % C.L. for the effective coupling constant in the benchmark

[3] Similar bounds have been obtained in the vector case, and for a spin-0 mediator, [19].

models at the ILC, increased in comparison to the ones of the LEP due to the use of a center of mass energy up to 1 TeV, are estimated by re-scaling the LEP limits. Concretely, the reduction of statistical uncertainty for the constrains in the four-fermion contact at ILC leads to improved limits on the Wilson coefficients C_i (which contain all information about short-distance physics) used to specified an effective Hamiltonian describing the four-lepton interactions. The impact is given in terms of

$$|C_{LL,RR}|^{max}_{ILC} = |C_{LL,RR}|^{max}_{LEP} \times \left[\frac{s_{ILC}}{s_{LEP}} \times \frac{\mathscr{L}_{ILC}}{\mathscr{L}_{LEP}}\right]^{-1/2} \times \sqrt{r_B}/r_s, \tag{5.2}$$

where for the ILC $\sqrt{s_{ILC}} = 1$ TeV and it's luminosity is taken as $\mathscr{L}_{ILC} = 500$ fb^{-1}, while for the LEP $\sqrt{s_{LEP}} \approx= 200$ GeV and $\mathscr{L}_{LEP} = 4 \times 0.75\ fb^{-1}$. Additionally, $r_{S,B}$ denotes the signal and background enhancement achieve due to the beam polarization, which values can be found in [40]. In this way, the LEP limits for the four-lepton contact interaction via the exchange of a scalar or vector boson, s-channel, are projected onto the the ILC setup by using eq. (5.2). The bounds from the four-lepton interactions at ILC on these models, when considering a spin-1 mediator at 90 % C.L, are for the relevant case of this study (axial-vector case):

$$\begin{aligned} \frac{g_a}{M_\eta} &< 2.7 \times 10^{-5}\ GeV^{-1} \quad \text{for } M_\eta > 1\ TeV \\ \frac{g_a}{M_\eta} &< 7.6 \times 10^{-5}\ GeV^{-1} \quad \text{for } 100\ GeV\ < M_\eta < 1\ TeV. \end{aligned} \tag{5.3}$$

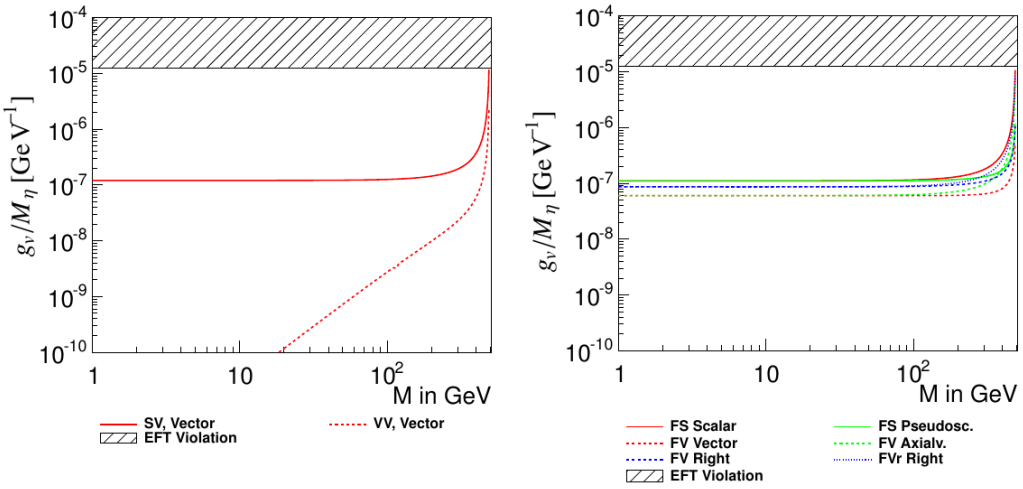

Fig. 5.13 90 % exclusion limits on the effective coupling g/M_η accessible at the ICL for s=1 TeV. The hashed area denotes the region violates the tree level approach with a too large domensionless coupling constant g< 4 π, or bz having a too small mediator mass, i.e. $m_\eta <$ 1 TeV.

The further combinated results to create the maximum exclusion bounds with the XENON100 limits obtained are analize are presented in the Mathematica notebook , as specified in Appendix. B.2.

Chapter 6

Conclusions

In this work the nature of dark matter was investigated under the assumption that it induces electronic recoils via inelastic scattering processes when it has scattered against electrons bound in atoms. This framework was found to reproduced, before calculating physical quantities with science data, in complete agreement with the results from other published works. Following, for this proposed framework, calculated direct detection limits are presented and discussed, based on the experimental results from the profile likelihood analysis of the 224.6 live days$\times$ 34 Kg exposure of XENON100 experimental data [14, 16]. The results achieved present a strong agreement with puplished ones by the XENON COLLABORATION [17].

Furthermore, motivated to try to reconcile the DAMA annual modulation signal found with the constraints for electron recoils from dark matter scattering, the proposal presented considered the hypothesis that dark matter could have tree level coupling to leptons, but not to quarks. However, the results point out that this hypothesis doesn't provide a satisfactory solution to explain the DAMA modulation signal. In one hand, whenever the Dirac structure of the DM-lepton coupling concedes an interaction with quarks at a loop level, WIMP-nucleus scattering will dominate the rate in direct detection experiments, which translates into the unsolved tension between DAMA/LIBRA signal and different constraints from searches for nuclear recoils from dark matter scattering. In the other hand, under the scenario of axial vector like coupling for DM-leptons, the analysis made points out that this model would be strongly disfavored as a conciliation with the DAMA/LIBRA signal.

In fact, under the results achieved, confirmed to be almost the same that the published by the X.C. [17], following the considerations performed in that study it would be straightforward to conclude that this proposal completely excludes the DAMA/LIBRA signal, and simultaneously sets one of the strongest direct limit on the cross section of WIMPs coupling

to electrons through axial-vector interactions, excluding cross-sections above 7×10^{-35} cm^2 for particle masses of $m_\chi = 3$ GeV.

These conclusions were achieved by having introduced an effective field theory framework that allowed to analyze the characteristics of this possible leptophilic nature of dark matter. This effective approach was used since it allowed to reduce the dimensionality of the parameter space and to compare the different bounds for dark matter obtained in different experimental searches, as bounds in the LEP or ILC colliders.

References

[1] Aglietta, M. et al. (1998). *Phys. Rev. D58 , 092005*.

[2] Agrawal, P. et al. (2010). A classification of dark matter candidates with primarily spin-dependent interactions with matter. *arXiv:1003.1912*.

[3] Akerib, D. S. et al. (2014). *Phys. Rev. Lett. 112. 091303*.

[4] Akimov, D. et al. (2001). Measurements of scintillation efficiency and pulse-shape for low energy recoils in liquid xenon. *arXiv:hep-ex/0106042*.

[5] Alcock, C. et al. (2000). The macho project: microlensing results from 5.7 years of large magellanic cloud observations. *ApJ. 542*, pages 281–307.

[6] Angle, J. et al. (2008). First results from the xenon10 dark matter experiment at the gran sasso national laboratory. *Phys. Rev. Lett. 100, 021303*.

[7] Aprile, E. and Doke, T. (2010). Liquid xenon detectors for particle physics and astrophysics. *Rev. Mod. Phys. 82, 2053*.

[8] Aprile, E. et al. (2006). Simultaneous measurement of ionization and scintillation from nuclear recoils in liquid xenon as target for a dark matter experiment. *Phys.Rev.Lett. 97 081302*.

[9] Aprile, E. et al. (2010a). Design and performance of the xenon10 dark matter experiment. *arXiv:1001.2834*.

[10] Aprile, E. et al. (2010b). First dark matter results from the xenon100 experiment. *arXiv:1005.0380*.

[11] Aprile, E. et al. (2011a). Dark matter results from 100 live days of xenon100 data. *10.1103/PhysRevLett.107.131302*.

[12] Aprile, E. et al. (2011b). Likelihood approach to the first dark matter results from xenon100. *10.1103/PhysRevD.84.052003*.

[13] Aprile, E. et al. (2011c). Study of the electromagnetic background in the xenon100 experiment. *Phys.Rev.D83:082001*.

[14] Aprile, E. et al. (2012a). Dark matter results from 225 live days of xenon100 data. *Phys. Rev. Lett. 109, 181301*.

[15] Aprile, E. et al. (2012b). The xenon100 dark matter experiment. *Astropart. Phys. 35*, pages 573–590.

[16] Aprile, E. et al. (2014). First axion results from the xenon100 experiment. *Phys.Rev.D90,062009*.

[17] Aprile, E. et al. (2015). Exclusion of leptophilic dark matter models using xenon100 electronic recoil data. *arXiv:1507.07747*.

[18] Baudis, L. et al. (2013). *Phys. Rev. D87, 115015*.

[19] Bell, N. F., Cai, Y., Leane, R. K., and Medina, A. D. (2014). Leptophilic dark matter with z' interactions. *arXiv:1407.3001*.

[20] Bergmann, A., Petrosian, V., and Lynds, R. (1990). Gravitational lens models of arcs in clusters. *Ap.J. 350*, pages "23–35".

[21] Bernabei, R. et al. (2007). Investigating electron interacting dark matter. *arXiv:0712.0562*.

[22] Birkedal, A., Matchev, K., and Perelstein, M. (2004). Dark matter at colliders: a model-independent approach. *10.1103/PhysRevD.70.077701*.

[23] Blumenthal, G. R., Faber, S. M., Primack, J. R., and Rees, M. J. (1984). Formation of galaxies and large-scale structure with cold dark matter. *311*, pages 517–525.

[24] Bosma, A. (1978). *The distribution and kinematics of neutral hydrogen in spiral galaxies of various morphological types*. PhD thesis, Groningen Univ.

[25] Bunge, C. et al. (1993). Roothaan-hartree-fock ground-state atomic wave-functions - slater-type orbital expansions and expectation values for z=2-54. *10.1006/adnd.1993.1003*.

[26] Casella, G. and Berger, R. L. (1990). Statistical inference. *Duxburry Press*, page 346.

[27] Collaboration, P. (2015). Planck 2015 results. xvi. isotropy and statistics of the cmb. *arXiv:1506.07135*.

[28] Dedes, A. et al. (2010). *Nucl. Phys.B826, 148, 0907.0758*.

[29] di Matteo, T. et al. (2008). Direct cosmological simulations of the growth of black holes and galaxies. *ApJ. 676*, pages 33–53.

[30] Dolgoshein, B. A., Lebedenko, V. N., and Rodionov, B. (1970). Jet p. *Lett. 11. 513*.

[31] Dreiner, H. et al. (2012a). Illuminating dark matter at the ilc. *arXiv:1211.2254*.

[32] Dreiner, H., Huck, M., Krämer, M., Schmeier, D., and Tattersall, J. (2012b). Illuminating dark matter at the ilc. *arXiv:1211.2254*.

[33] Ellis, J. R., Flores, R., and Lewin, J. (1988). Rates for inelastic nuclear excitation by dark matter particles. *Phys.Lett.B212*, page 375.

[34] Essig, R. et al. (2012). First direct detection limits on sub-gev dark matter from xenon10. *arXiv:1206.2644*.

[35] Essig, R., Mardon, J., and Volansky, T. (2011). Direct detection of sub-gev dark matter. *arXiv:1108.5383*.

[36] Feng, J. L. (2010). Dark matter candidates from particle physics and methods of detection,. *arXiv:1003.0904*.

[37] Fox, P. J. et al. (2011). Lep shines light on dark matter. *arXiv:1103.0240*.

[38] Fox, P. J. and Poppitz, E. (2008). Leptophilic dark matter. *10.1103/PhysRevD.79.083528*.

[39] Freese, K., Lisanti, M., and Savage, C. (2012). Annual modulation of dark matter: A review. *arXiv:1209.3339*.

[40] Freitas, A. and Westhoff, S. (2014). Leptophilic dark matter in lepton interactions at lep and ilc. *10.1007/JHEP10(2014)116*.

[41] Garrett, K. and Duda, G. (2010). Dark matter: A primer. *arXiv:1006.2483*.

[Haba et al.] Haba, N. et al. A simple method of calculating effective operators. *10.1103/PhysRevD.84.014028*.

[43] Huterer, D. (2010). Weak lensing, dark matter and dark energy. *arXiv:1001.1758*.

[44] Jarosik, N. et al. (2010). Seven-year wilkinson microwave anisotropy probe (wmap1) observations: Sky maps, systematic errors, and basic results,. *arXiv:1001.4744v1*.

[45] Jedamzik, K. and Pospelov, M. (2009). Big bang nucleosynthesis and particle dark matter. *New J. Phys. 11 105028, arXiv:0906.2087*.

[46] Klasen, M., Pohl, M., and Sigl, G. (2015). Indirect and direct search for dark matter. *arXiv:1507.03800*.

[47] Kopp, J., Niro, V., Schwetz, T., and Zupanl, J. (2009). *Phys. Rev.D80, 083502*.

[48] Lavina, L. S. X. C. (2013). Latest results from xenon100 data. *arXiv:1305.0224*.

[49] Lee, S. K. et al. (2015). Modulation effects in dark matter-electron scattering experiments. *arXiv:1508.07361*.

[50] Lewin, J. D. and Smith, P. F. (1996). *Astropart. Phys.6, 87*.

[51] Massey, R., Rhodes, J., Ellis, R., et al. (2007). Dark matter maps reveal cosmic scaffolding. *Nature 445*, pages 286–290.

[52] Mocchiutti, E. et al. (2009). The pamela space experiment. *arXiv:0905.2551*.

[53] Morita, M. (1973). *Beta Decay and Muon Capture*. Benjamin, W. A, 1st Edition.

[54] Ni, K. (2006). *Development of a Liquid Xenon Time Projection Chamber for the XENON Dark Matter Search*. PhD thesis, Columbia University, New York.

[55] Oberlack, U. (2012). Hap dark universe topical workshop on data analysis and detector technologies. In *http://www.ucolick.org/ diemand/vl*.

[56] Oort, J. H. (1932). Bain. *6*, page 249.

[57] Ostriker, J. P. and Peebles, P. J. E. (1973). A numerical study of the stability of flattened galaxies: or, can cold galaxies survive?,. 186:467–480.

[58] Peebles, P. J. E. (1982). Large-scale background temperature and mass fluctuations due to scale-invariant primeval perturbations. *ApJ. 263, L1-L5*.

[59] Plante, G. (2012). *The XENON100 Dark Matter Experiment: Design, Construction, Calibration and 2010 Search Results with Improved Measurement of the Scintillation Response of Liquid Xenon to Low-Energy Nuclear Recoils*. PhD thesis, Columbia University, New York.

[60] R., B. et al. (2014). Annual modulation of cosmic relic neutrinos. *arXiv:1404.0680*.

[61] Rolke, W. A., Lopez, A. M., and Conrad, J. (2009). Limits and confidence intervals in the presence of nuisance parameters. *arXiv:physics/0403059*.

[62] Rosendahl, S., Brown, E., Cristescu, I., Fieguth, A., Huhmann, C., Murra, M., and Weinheimer, C. (2014). A cryogenic distillation column for the xenon1t experiment. *J. Phys.: Conf. Ser. 564 012006*.

[63] Rubin, V. (1983). Dark matter in spiral galaxies,. *Scientific American. 248*, pages 96–108.

[64] Rubin, V. C. and Ford, W. K. (1970). *ApJ 159. 379.*, pages 257–270.

[65] Rubin, V. C., Thonnard, N., and Ford, W. K. (1978). *ApJ 225 L107L111.*

[66] Ryden, B. (2003). Introduction to cosmology. *Addison Wessley*.

[67] Saab, T. (2012). An introduction to dark matter direct detection searches & techniques. *arXiv:1203.2566*.

[68] Smith, M. et al. (2007). The rave survey: Constraining the local galactic escape speed. *arXiv:astro-ph/0611671*.

[69] Sommerfeld, A. (1931). Uberer die beugung und bremsung der elektronen. *Annalen der Ph ysik 403*, page 257.

[70] Steigman, G. and Turner, M. S. (1985). *Nucl. Phys. B253, 375*.

[71] Szydagis, M. et al. (2011). Jinst 6. *10002*.

[72] Torii, S. et al. (2008). High-energy electron observations by ppb-bets flight in antarctica. *arXiv:0809.0760*.

[73] Tucker-Smith, D. and Weiner, N. (2001). Inelastic dark matter. *arXiv:hep-ph/0101138 [hep-ph]*.

[74] W., P. et al. (2012). Semiconductor probes of light dark matter. *arXiv:1203.2531*.

[75] Zhang, H. et al. (2011). Effective dark matter model: Relic density, cdms ii, fermi lat and lhc. *10.1007/JHEP08(2011)018*.

Appendix A

Direct Detection basics

A.1 Dark matter elastic scattering kinematics

This Appendix presents the basic kinematics for non-relativistic dark matter particles scattering elastically with an electron. This result is used to estimate the possible amount of recoil energy that can be obtain in this sort of processes. The following calculations describe the scattering when it takes place, as shown in Fig. A.1, in the laboratory frame or in the center of mass frame:

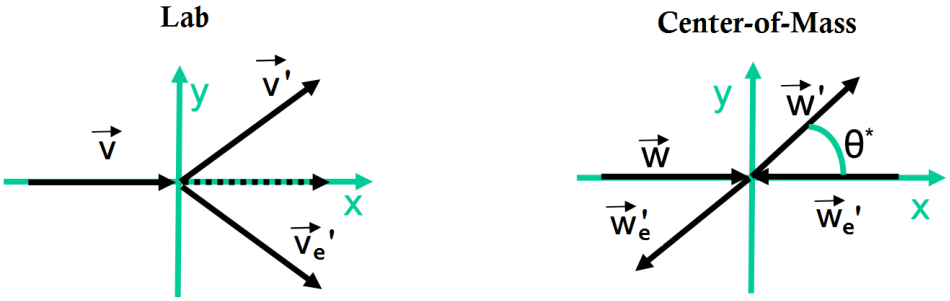

	In	Out
DM	$\vec{v}_\chi$	$\vec{v}'_\chi$
e	0	$\vec{v}_e$

	In	Out
DM	$\vec{w}_\chi$	$\vec{w}'_\chi$
e	$\vec{w}_e$	$\vec{w}'_e$

Fig. A.1 Non relativistic kinematics for the incoming and outgoing particles after the DM-e elastic scattering in the (Left) laboratory frame (Right) center of mass frame.

First, for the laboratory frame it follows that $v_\chi \equiv |\vec{v}_\chi|$, $v'_\chi \equiv |\vec{v}'_\chi|$ and $v_e \equiv |\vec{v}_e|$, while for the center of mass frame it follows that $w_\chi \equiv |\vec{w}_\chi|$, $w'_\chi \equiv |\vec{w}'_\chi|$, $w_e \equiv |\vec{w}_e|$ and $w'_e \equiv |\vec{w}'_e|$.

Under the indicated components from Fig. A.1, the recoil energy of the electron is given by

$$E_R = \frac{1}{2} m_e \vec{v}_e^2 = \frac{1}{2} m_e (v'^2_{e,x} + v'^2_{e,y}), \tag{A.1}$$

where $v_{e,x} = w'_e + v_{cm}$ and $v_{e,y} = w'_{e,y}$. From momentum and energy conservation: $w_\chi = w'_\chi$, $w_e = w'_e$ and $|\vec{w}_e| = \frac{m_\chi}{m_e}$. Given a boost:

$$(Galilean)boost = \begin{cases} v_{e,x} & = w'_{e,x} + v_{cm} \\ v_{e,y} & = w'_{e,y} \end{cases},$$

one can work the algebra to write down $v_{e,x}$ and $v_{e,y}$. First :

$$v_{cm} = \frac{m_\chi}{m_\chi + m_e} v_\chi, \quad \text{such that} \quad w_\chi = v_\chi - v_{cm} = \frac{m_e}{m_\chi + m_e} v_\chi.$$

Then, by using the angle θ^* to project the components:

$$v_{cm} = \frac{m_\chi}{m_\chi + m_e} v_\chi, \quad \text{such that} \quad w_\chi = v_\chi - v_{cm} = \frac{m_e}{m_\chi + m_e} v_\chi.$$

$$\begin{aligned} \Rightarrow v'_{e,x} &= w'_{e,x} + v_{cm} = w'_e \cos\theta^* + v_{cm} = w_e \cos\theta^* + v_{cm} = \frac{m_\chi}{m_e} w_\chi + v_{cm} \\ &= \frac{m_\chi}{m_e} \frac{m_e}{m_\chi + m_e} v_\chi \cos\theta^* + \frac{m_\chi}{m_\chi + m_e} v_\chi = \frac{m_\chi}{m_\chi + m_e} v_\chi (1 + \cos\theta^*) \end{aligned} \tag{A.2}$$

$$\Rightarrow v'_{e,y} = w'_{e,y} = w'_e \sin\theta^* = w_e \frac{m_\chi}{m_e} \frac{m_e}{m_\chi + m_e} v_\chi v_\chi \sin\theta^* = \frac{m_\chi}{m_\chi + m_e} v_\chi \sin\theta^* \tag{A.3}$$

Inserting the components $v'_{e,x}$, $v'_{e,y}$ into eq (A.1), one obtains:

$$E_R = \frac{1}{2} m_e (v'^2_{e,x} + v'^2_{e,y}) = \frac{1}{2} m_e \frac{m_\chi^2}{(m_\chi + m_e)^2} v_\chi^2 [(1 + \cos^2\theta^*)^2 + \sin^2\theta^*] \tag{A.4}$$

The recoil energy of the electrons (i.e. what experiments measure!) is then:

$$E_R = \frac{1}{2} m_\chi v_\chi^2 \times \frac{m_\chi m_e}{(m_\chi + m_e)^2} \times \frac{(1 + \cos^2\theta^*)}{2} \tag{A.5}$$

In more details:

$$E_R = \frac{1}{2} m_\chi v_\chi^2 \times \frac{m_\chi m_e}{(m_\chi + m_e)^2} \times \frac{(1+\cos^2\theta^*)}{2}$$

Kinetic Energy of incoming DM particle | mass-matching factor ($0 < f_1 < 1$) | angular factor ($0 < f_2 < 1$)

From eq (A.5) it can be infer that the maximal energy possibly transferred take place for head-on recoil ($f_2 = 1$ when $\theta^* = 0$) when the incoming particle and target have the same mass ($f_1 = 1$ when $m_\chi = m_e$):

$$E_R^{MAX} = \frac{1}{2} m_\chi v_\chi^2 = \text{ kinetic energy of incoming DM particle,} \tag{A.6}$$

i.e., in the maximal-energy-transfer collision, the DM particle is stopped and it transfers all its kinetic energy to the electrons. Two useful lessons can be learn from this trivial calculation:

- In a general way, mass matching enhances sensitivity to recoils. In a target detector made of different nuclear targets, lighter DM particles scatter mostly off lighter targets, whereas heavier DM particles scatter mostly off heavier targets. So a detector containing a light nuclear target is more sensitive to lighter DM particles compared to a detector containing heavier nuclear targets.

- Most importantly, in the context of direct detection, since the incoming DM particles velocity goes like $v \sim 10^{-3} c$, the maximal expected recoil energy in these processes is of the order of **eV's**:

$$\begin{aligned} E_R^{MAX} &\simeq \frac{1}{2}(100MeV)\left(\frac{m_\chi}{100MeV}\right)(10^{-6}) \\ &\simeq 50\ \mathbf{eV} \times \left(\frac{m_\chi}{100MeV}\right) \end{aligned} \tag{A.7}$$

A.2 Velocity Distribution

The primary astrophysical assumption made about dark matter in the halo is that it has a "sufficiently" close Maxwellian velocity distribution; which provides an appropriate description of the velocities of particles which move freely up to short collisions. Here, one assumes that the dark matter particles are isothermally and isotropically distributed in the phase space (i.e. gravitationally relaxed). Then, as discussed in [50], one considers the the incoming

dark matter particles are not monochromatic, just $v \sim 10^{-3}c$, but instead that they follow a continuous distribution f(v). This dark matter velocity distribution is given by:

$$f(v, v_E) = e^{-(v+v_E)^2/v_0^2} \tag{A.8}$$

Here, **v** is velocity onto the (Earth-borne) target, $\mathbf{v}_E$ is Earth (target) velocity relative to the dark matter distribution, v_0 is the most probable dark matter speed (given by the characteristic kinetic energy), and v_{esc} is the local Galactic escape velocity, i.e., because the dark matter halo is gravitationally bound, there is a characteristic escape velocity at which the Maxwell distribution necessarily breaks down since any particles with such energies would escape the halo[1].

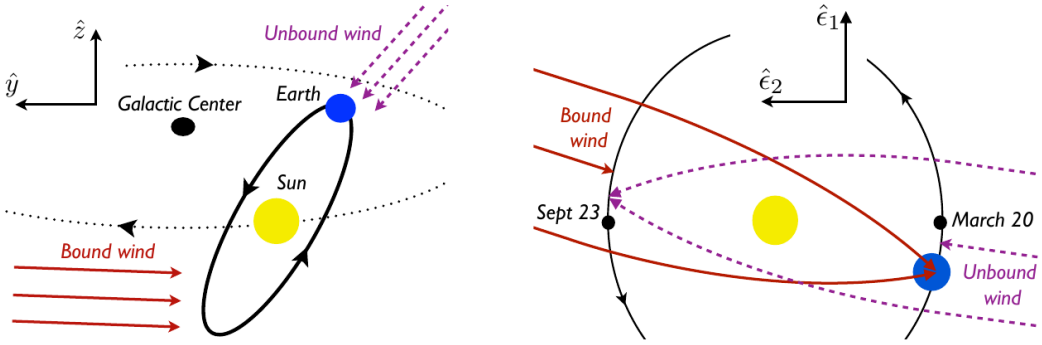

Fig. A.2 The Earth orbits around the Sun, which orbits around the Galactic Center. All of the Galaxy moves with respect to the CvB. (Left) A projection of the Earth's orbit onto the Galactic $\vec{y} - \vec{z}$ plane. The dotted curve illustrates the Sun's orbit about the Galactic Center in the $\vec{x} - \vec{y}$ plane (Right) The Earth's orbit in the ecliptic plane, spanned by the vectors, taken from [60].

Now let us account for the modulated velocity of the Earth relative to the dark matter halo, see Fig A.2, which can be written as:

$$v_E = 232 + 15\cos\left(2\pi \frac{t - 152.5\ days}{365.25\ days}\right) kms^{-1}, \tag{A.9}$$

this is due to the unfortunate placement of the solar system in the Milky Way galaxy, the average velocity ($232 km/s$) is not very well known, though the amplitude of the modulation ($15 km/s$) is well measured. One should further remark that there are small errors since the modulation isn't exactly sinusoidal.

[1]Technically, the gravitational potential modifies the Maxwell distribution at its tail, but it is typically sufficient to impose a hard cutoff.

Now, some useful results can be derived as follows: for $v_{esc} = \infty$ one has, for a stationary Earth ($\mathbf{v}_E = 0$):

$$k_0 = \int_0^{2\pi} d\phi \int_{-1}^{+1} d(\cos\theta) \int_0^{\infty} e^{-(v)^2/v_0^2} v^2 dv = (\pi v_0^2)^{3/2} \tag{A.10}$$

In the case of a moving Earth, for which $(v+v_E)^2 = v^2 + v_E^2 + 2vv_E\cos\theta$:

$$\begin{aligned} k &= \int_0^{2\pi} d\phi \int_{-1}^{+1} d(\cos\theta) \int_0^{\infty} e^{-(v+v_E)^2/v_0^2} v^2 dv \\ &= (\pi v_0^2)^{3/2} = 2\pi \int_0^{\infty} e^{-(v+v_E)^2/v_0^2} v^2 dv \int_{-1}^{+1} e^{-2vv_E\cos\theta/v_0^2} v^2 d(\cos\theta) dv \\ &= \frac{\pi v_0^2}{v_E} \int_0^{\infty} v \left[e^{-(v-v_E)^2/v_0^2} - e^{-(v+v_E)^2/v_0^2} \right] dv = \frac{\pi v_0^2}{v_E} \left[2v_E \frac{\pi^{1/2}}{2} v_0 \right] \equiv k_0 \end{aligned} \tag{A.11}$$

However, in the most general case where $v_{esc} \neq \infty$ and when the Earth movement is considered to be $\mathbf{v}_E \neq 0$, one can define the general function:

$$\eta(v_{min}) = \int \frac{1}{v} f(v, v_E) d^3v, \tag{A.12}$$

where v_{min} is define as $v_{min} = (|E_B^{nl}| + E_R)/q + q/2m_\chi$. Given that the differential and total rates require this integral, the result can be computed and expressed in terms of v-dependent inputs of the rates:

$$\begin{aligned} \eta(v_{min}) &= \int_{v_{min}}^{v_{max}} \frac{1}{v} f(v, v_E) d^3v \\ &= \frac{1}{2v_E} \left[\int_{v_{min}}^{v_{esc}+v_E} e^{-(v-v_E)^2/v_0^2} dv - \int_{v_{min}}^{v_{esc}-v_E} e^{-(v+v_E)^2/v_0^2} dv - e^{-v_{esc}^2/v_0^2} \int_{v_{esc}-v_E}^{v_{esc}+v_E} dv \right] \\ &= \frac{1}{2v_E} \left\{ \left[\int_{v_{min}-v_E}^{v_{esc}} e^{-w^2/v_0^2} dw - \int_{v_{min}+v_E}^{v_{esc}} e^{-w^2/v_0^2} dw \right] - e^{-v_{esc}^2/v_0^2} \right\} \\ &= \frac{2\pi v_0^2}{k} \left\{ \frac{\pi^{1/2}}{4} \frac{v_0}{v_E} \left[erf\left(\frac{v_{min}+v_E}{V_0} \right) - erf\left(\frac{v_{min}-v_E}{V_0} \right) \right] - e^{-v_{esc}^2/v_0^2} \right\} \end{aligned} \tag{A.13}$$

In practice, for convenience, when computationally calculating $d\langle\sigma_{ion}^{nl} v\rangle / d\ln E_R$, defined by eq (3.6), or $dR_{ion}/d\ln E_R$ defined by eq (3.11), the exponential term in eq (A.13) can be neglected without altering the results.

Appendix B

Framework Tools

B.1 RHF bound wavefunctions for Xenon

This Appendix describes the tools needed to compute the radial momentum space wave function $\chi_{nl}(p)$ for the DM-electron inelastic scattering used to evaluate the ionization form factor $|f_{ion}^{nl}(k',q)|^2$ defined in eq (3.8), and consequently the velocity-averaged differential ionization cross section $d\langle\sigma_{ion}^{nl}v\rangle/d\ln E_R$ defined in eq (3.6), along with the differential ionization rate $dR_{ion}/d\ln E_R$ defined in eq (3.11).

B.1.1 Hartree-Fock method

In the context of computational physics and chemestry, the Hartree-Fock (HF) method is an approximation method used to determine the wave function and the energy of a quantum many-body system in a stationary state.

Essentially, the HF theory was developed to solve the electronic time-independent Schrödinger equation that results after invoking the Born-Oppenheimmer approximation[1]. To do so, it assumes that the wavefunction can be approximated by a single Slater determinant made up of one spin orbital per electron.

Concretely, the objective of the HF methods is to determine the set of spin orbitals which minimize the energy and give the best single Slater determinant. As described in [25], the HF equations can be solved numerically or they can be solved in the space spanned by a set of basis functions (Roothan-Hartree-Fock equations). In either case, the solutions depend on the orbital, thus, one needs to guess some initial orbital and then refine the guesses iteratively;

[1] http://vergil.chemistry.gatech.edu/notes/hf-intro/hf-intro.pdf

for this reason, HF is called a self-consistent-field (SCF) approach, and the solutions of the RHF equations are often known as a self-consistent-field procedure.

B.1.2 χ_{nl}, R_{nl}

First, the momentum space wavefunction $\psi_{nlm}(p)$ of the initial bound electron can be defined by

$$\begin{aligned}\psi_{nlm}(p) &= \int d^3x \psi_{nlm}(x) e^{-i\mathbf{p}\cdot\mathbf{x}} \\ &\equiv \chi_{nl}(p) Y_{lm}(\theta,\phi),\end{aligned} \tag{B.1}$$

with the normalization $\int d^3p |\psi_{nlm}(p)|^2 = (2\pi)^3$.

When the scenario of DM-electron scattering is considered, the momentum space radial wave function $\chi_{nl}(\mathbf{p})$ is obtained by splitting the coordinate space wave function $\psi_{nlm}(\mathbf{x})$ into its angular part $Y_{lm}(\theta,\phi)$ and its radial part $R_{nl}(r)$:

$$\begin{aligned}\chi_{nl}(p) &= \frac{4\pi}{2l+1}\sum_m \psi_{nlm}(\mathbf{p}) Y_{lm}(\theta_p,\phi_p) \\ &= \frac{4\pi}{2l+1}\sum_m (-1)^m \int dr\, r^2 R_{nl}(r) Y_l^m(\theta_p,\phi_p) Y_l^{-m}(\theta_p,\phi_p) e^{i\mathbf{p}\cdot\mathbf{r}} d\Omega \\ &= \int dr\, r^2 R_{nl}(r) \int_0^\pi \int_0^{2\pi} P_l(\cos\theta)\sin\theta d\theta d\varphi e^{i\mathbf{p}\cdot\mathbf{r}} \\ &= 2\pi \int dr\, r^2 R_{nl}(r) \int d(\cos\theta) P_l(\cos\theta) e^{ipr\cos\theta}\end{aligned} \tag{B.2}$$

Since

$$j_n(z) = \frac{(-i)^n}{2}\int_0^\pi -d(\cos\theta) P_n(\cos\theta) e^{iz\cos\theta}, \tag{B.3}$$

so one can write eq (B.2) as

$$\chi_{nl}(p) = 4\pi i^l \int dr\, r^2 R_{nl}(r) j_l(pr). \tag{B.4}$$

Here, $\mathbf{p}$ is a momentum space vector with modulus p and arbitrary orientation (θ_p,ϕ_p), and $P_l(\cos\theta)$ is a Legendre polynomial. To obtain this result, in the second line was used the orthogonality of the spherical harmonics:

$$\int_0^\pi \int_0^{2\pi} Ylm(\theta,\phi) Yl'm'(\theta,\phi)\sin\theta d\theta d\varphi = \delta_{ll'}\delta_{mm'},$$

and in the last 2 lines was used the Gegenbauer's formula, which relates the Fourier type integral over a Legendre polynomial to the spherical Bessel function of the same degree.

As explained in [47], the radial wavefunctions R_{nl} can be approximated by a linear combination of so-called Slater type orbitals (STOs) as:

$$R_{nl}(r) = \sum_k C_{nlk} \frac{(2Z_{lk})^{n_{lk}+1/2}}{a_0^{3/2}\sqrt{(2n_{lk})!}} (r/a_0)^{n_{lk}-1} exp\left(-\frac{Z_{lk}r}{a_0}\right). \tag{B.5}$$

Here, a_0 is the Bohr radius and C_{nlk}, Z_{lk} and n_{lk} are the coefficients from the numerical Roothaan-Hartree-Fock bound wave functions tabulated in [25], used when treating the target electron as single-particles states bound in isolated xenon atoms[2].

With $R_{nl}(r)$ given in the form of eq (B.5), one can evaluate eq (B.4) analytically in order to obtain:

$$\begin{aligned}\chi_{nl}(p) = \sum_k C_{nlk} 2^{-l+n_{lk}} \left(\frac{2\pi a_0}{Z_{lk}}\right)^{3/2} \left(\frac{ipa_0}{Z_{lk}}\right)^l \frac{(1+n_{lk}+l)!}{\sqrt{(2n_{lk})!}} \\ \times {}_2F_1\left[\frac{1}{2}(2+l+n_{lk}), \frac{1}{2}(3+l+n_{lk}), \frac{3}{2}+l, -\left(\frac{pa_0}{Z_{lk}}\right)^2\right],\end{aligned} \tag{B.6}$$

where ${}_2F_1(a,b,c,x)$ is a hypergeometric function.

B.1.3 Explanation tabulated values

The tabulated values of the RHF ground state atomic wavefunction for Xenon are shown in Fig. B.1. Here, for each data block, the first row lists the element considered, its atomic number z and its configuration in terms of the ground-state wave function[3].

The second row specifies the total kinetic and potential energy in atomic units (M), where 1 $a.u. = 27.2113961\ eV$ and 1 $a.u.\ (M)$ is equivalent to 1 $a.u.\frac{1}{1+m/M}$, where m is the electrons mass and M is the nuclear mass of the target.

Next, $1s, 2p, ...$ denote the RHF orbital: below each orbital are listed the orbital energies in $a.u.\ (M)$ units and their expectation values $\langle R \rangle$ also in $a.u.\ (M)$ units. The orbital coefficients C_{nlk}, from eqs (B.5) and (B.6) are listed next under each RHF orbital $1s, 2p, ...$, which denotes

[2] For a brief summary of how to obtain and use these tabulated values, see Appendix B.1.3.

[3] As an example, for Silicon ($z = 14$): $[Ne]3s(2)3p(2)3p$ would mean $1s^2 2s^2 2p^6 3s^2 3p^{23} p$.

the Slater-type orbital (STOs) n_{jl}. Finally, the orbital exponent Z_{jl} are shown following the STO designation.

```
XENON, Z=54     [Kr]4d(10)5s(2)5p(6)  1S

TOTAL ENERGY   KINETIC ENERGY  POTENTIAL ENERGY  VIRIAL RATIO
-7232.138349     7232.138386     -14464.27673    -1.999999995

RHOat0 = 698865.13   Kato cusp = 2.000711

                 1s          2s          3s          4s          5s
ORB.ENERGY 1224.397767-189.340111 -40.175652  -7.856291  -0.944407
<R>            0.028141    0.120873    0.318696    0.745267    1.980955
<R**2>         0.001059    0.017160    0.115870    0.625571    4.440087
<1/R>         53.469284   12.309921    4.527285    1.842538    0.647891
<1/R**2>    5736.266145 614.934856 125.507901  26.858025   3.506821

1S   54.9179  -0.965401    0.313912  -0.140382   0.064020  -0.022510
2S   47.2500  -0.040350    0.236118  -0.125401   0.059550  -0.021077
2S   26.0942   0.001890   -0.985333   0.528161  -0.251138   0.088978
3S   68.1771  -0.003868    0.000229  -0.000435   0.000152  -0.000081
3S   16.8296  -0.000263   -0.346825   0.494492  -0.252274   0.095199
3S   12.0759   0.000547    0.345786  -1.855445   1.063559  -0.398492
4S   31.9030  -0.000791   -0.120941   0.128637  -0.071737   0.025623
4S    8.0145   0.000014   -0.005057  -0.017980  -0.563072   0.274471
4S    5.8396  -0.000013    0.001528   0.000792  -0.697466   0.291110
5S   14.7123  -0.000286   -0.151508   0.333907  -0.058009   0.011171
5S    3.8555   0.000005   -0.000281  -0.000228  -0.018353  -0.463123
5S    2.6343  -0.000003    0.000134   0.000191   0.002292  -0.545266
5S    1.8124   0.000001   -0.000040  -0.000037  -0.000834  -0.167779

                 2p          3p          4p          5p
ORB.ENERGY -177.782438 -35.221651  -6.008328  -0.457283
<R>            0.103082    0.309425    0.777023    2.337950
<R**2>         0.012915    0.110816    0.685527    6.276430
<1/R>         12.291694    4.444510    1.741492    0.547155
<1/R**2>     204.419530   41.612611    8.690096    0.970729
<1/R**3>    5182.670677 989.845535 189.572708  17.825267

2P   58.7712   0.051242    0.000264   0.013769  -0.005879
2P   22.6065   0.781070    0.622357  -0.426955   0.149040
3P   48.9702   0.114910   -0.009861   0.045088  -0.018716
3P   13.4997  -0.000731   -0.952677   0.748434  -0.266839
3P    9.8328   0.000458   -0.337900   0.132850  -0.031096
4P   40.2591   0.083993   -0.026340   0.059406  -0.024100
4P    7.1841  -0.000265   -0.000384  -0.679569   0.267374
4P    5.1284   0.000034   -0.001665  -0.503653   0.161460
5P   21.5330   0.009061    0.087491  -0.149635   0.059721
5P    3.4469  -0.000014    0.000240  -0.014193  -0.428353
5P    2.2384   0.000006   -0.000083   0.000528  -0.542284
5P    1.4588  -0.000002    0.000026  -0.000221  -0.201667

                 3d          4d
ORB.ENERGY   -26.118859  -2.777871
<R>            0.280333    0.870451
<R**2>         0.092633    0.880863
<1/R>          4.304379    1.508735
<1/R**2>      23.067118    4.099141
<1/R**3>     160.847940   24.028996

3D   19.9787   0.220185   -0.013758
3D   12.2129   0.603140   -0.804573
3D    8.6994   0.194682    0.260624
4D   27.7398  -0.014369    0.007490
4D   15.9410   0.049865    0.244109
4D    6.0580  -0.000300    0.597018
4D    4.0990   0.000418    0.395554
4D    2.5857  -0.000133    0.039786
```

Fig. B.1 Roothan-Hartree-Fock Ground-State Atomic Wave Function, $z = 54$ (Xenon)

B.2 Mathematica Notebook

This Appendix presents a complete description of the Mathematica Notebook (Nb) that was used to calculate all the presented results in this work. The final version of the notebook file, named " dd_limits_dm_vs_e_recoil.nb", along with the files containing the different data points used, can be found in a dropbox link [4]. The program was written down in Wolfram Mathematica version 10. Also, the data from the different plots that was compared through Chapter 5, was obtained by using the open source application for Linux " G3data graph analizer" version 1.5.4.

The integration methods chosen in each declaration of functions were based on the best preference that Mathematica's functions, such as *Nintegrate* (Numerical integrate), could provide in terms of time vs accuracy; as a standard, the functions were specified with a *WorkingPrecision* of 15, which fixed how many digits of precision should be maintained in internal computations, along with an *AccuracyGoal* of 15, which translated into how many effective digits of accuracy should be sought in the final result.

B.2.1 Structure of the Notebook

The notebook is divided into the following chapters:

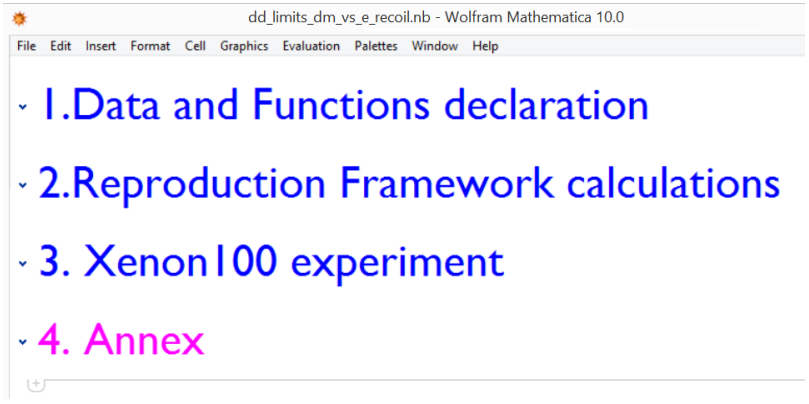

Each of these Chapters, at the same time, can be expanded into the following sections and subsections:

[4] https://www.dropbox.com/sh/wuwpws669jfi0ns/AAC0uEXg9SjALGZOhsf14VVja?dl=0

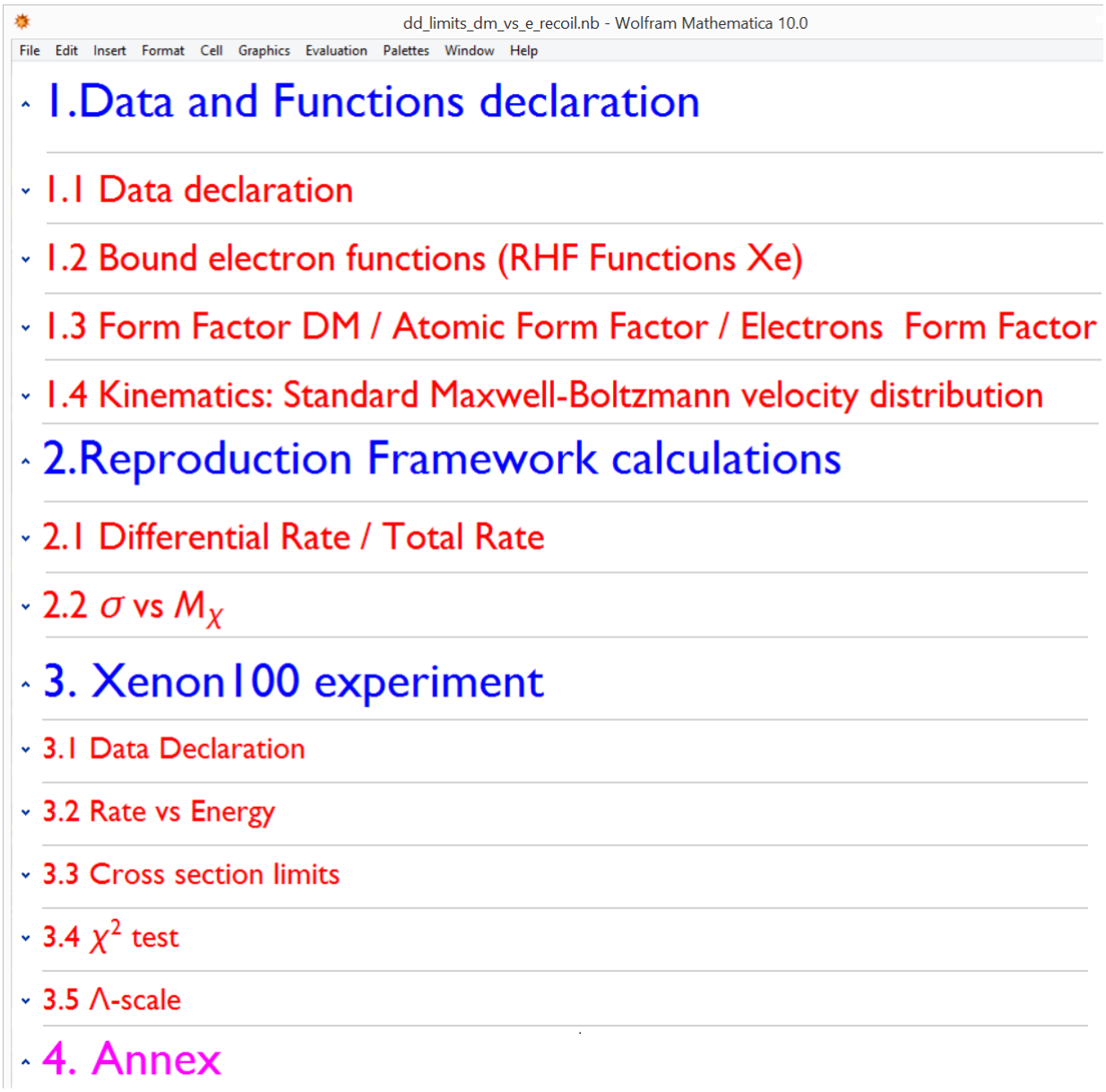

B.2.2 Description

In order to understand the functioning, a brief description of the purpose of each chapter's sections and subsections is now presented:

NB Chapter 1 objective is to declare the values of different fundamental physical constants along with the majority of the general functions which are used recursively in all the calculations.

Section 1.1 starts by declaring values such as the mass of the electron, the fine-structure constant, the Bohr radius, etc., followed by the kinematic constant values needed in Appendix A.2, in order to define the Maxwell-Boltzmann velocity distribution. Lastly, the coefficients of the RHF bounded wavefunctions for the Xenon, specified in Fig. B.1, are also declare (i.e. the coefficients C_{nlk}, Z_{lk} and n_{lk}). *Section 1.2* declares the radial momentum-space wavefuntion χ_{nl} specified by eq (B.6) and checks out its normalization condition.

Section 1.3 starts by declaring the different dark matter form factors that are going to be study, $F_{DM} = 1$ and $F_{DM} = (\alpha m_e)^2/q^2$, along with the Fermi form-factor given by eq. (3.1), and the ionization form-factor given by eq. (3.11), as discussed in Chapter 3. Lastly, *Section 1.4* declares the standard Maxwell-Boltzmann velocity distribution function and its components, as defined by eq. (A.13) in Appendix A.1.

NB Chapter 2 objective is to build up the framework tools presented in Chapter 3, and to reproduce the calculations made in the paper "Direct Detection of Sub-GeV Dark Matter", by R. Essig *et al*, [35], i.e., to get sure, before proceeding, that the framework reproduces and agrees with results already published.

Section 2.1 starts by stating the "Expected" projection values for the differential rate $dR/dlnE_R$ and cross section $d\sigma/dE_R$, in the context of the mechanism of DM-e recoil, against the mass of dark matter. Here, the declaration of the rate is done, as defined in Chapter 3, followed by the plot that shows the framework's result.

Section 2.2 deals with the calculation of the differential cross section after having assume a fixed differential rate, as specified in [35]. In order to calculate the exclusion plot σ vs m_χ, one needs to use a *Bisection* method routine[5] that will proceeds as follows: Starting from eq. (3.11), and by having assumed a fixed value for the differential rate dR/dE_R, one asks for the lowest value that σ needs to take in order to surpass the fixed quantity dR/dE_R for a given dark matter mass: the routine was designed specifically in a logarithm scale to find the values satisfying that condition (given that the search take place in the cross section scale).

The bisection method takes place and repeatedly bisects the interval specified for the cross section scale, until up to a specified accuracy provides the lowest values, such that the cross section σ surpasses dR/dE_R. Once that the value is found, iteratively, the same calculation

[5]The bisection method in mathematics is a root-finding method that repeatedly bisects an interval and then selects a sub-interval in which a root must lie for further processing. In principle, it is a very simple and robust method, although is relatively slow.

is done again for a another dark matter mass value. The program offers the option to specify the cross section scale interval for the search, along with the dark matter scale range and the number of iterations (accuracy) wanted. Later in the *subsection 2.2.2* is declared a "*for*" routine that performs the automatic calculation of the plot σ vs m_χ. *Subsection 2.2.3* presents 15 points calculated along with the plot comparing the paper's results with the results from the framework[6].

Once that the framework reproduces published results, **NB Chapter 3** proceeds by declaring the results of the XENON100 Experiment after having been analysed by the XENON Collaboration, as discussed in Chapter 2, Section 2.3.2: as a whole, the idea is to use this appropriate physical input in order to produce real cross section limits in the context of the mechanism specified. After having acquired the science data, one would expect to calculate the infamous σ vs m_χ plot showing the cross section limits for dark matter and to compare the results against the recently published ones by the XENON Collaboration in [].

Section 3.1 starts by showing the extracted data from Fig. 2.17, which provides by means of an interpolation function to convert any energy value from PE units to KeV, or MeV, units. This is followed by specifying the extracted values from the overall acceptance of the experiment by using Fig. 2.16, Bottom; from which one can reconstruct a function in order to later on compute results including the acceptance for any specific energy considered. Lastly, Fig. 2.19, Top; indicates the event distribution of the science data between 3 and 30 PE, the event values are extracted after the cut at 3 PE, and these values are expressed in MeV units using the previous function obtained (these are the physical inputs that later on one uses).

Section 3.2 presents the definition of the differential rate, including the acceptance of the experiment, for the dark matter form-factor $F_{DM} = 1$. This is followed by the plot of the differential ionization rate against the electron recoil energy in the range between 1.9-8 Kev, when different values of the mass (such as $m_\chi = 1\ Gev,\ 10\ Gev,\ 100\ Gev,\ 1TeV$), for $F_{DM} = 1$. The idea is to vary the values of σ in order to find where the rate is above the background profile model presented (dashed lines), when looking to the right of the cut point 3 PE. The value $\sigma = 10^{-35}$, shown as an example, satisfies this for all the masses values chosen.

Section 3.3 initializes the conditions to run the bisection routine that calculates the cross section limits against the dark matter mass. As explained in Section 2.2, this is one way to

[6]Each point takes approximately 28.3 hours of calculation in a Intel core i5, which justifies to just have presented a relatively modest amount of points for the plot, since the agreement was noticeable.

engage this task, although more than an exact results it is a rough estimation of the real cross section limits. Nevertheless, one can do better by calculating the same cross section but when using, instead, the science data by means of implementing the standard Pearson χ^2-Test, in order to obtain limits with a given confidence level, as explained in Appendix C.2.

Section 3.4 approaches the implementation of the χ^2-Test, in order to get far better results. First, one declares the cross section limit values achieved by the XENON Collaboration. Then, one proceeds to define the routines that implement, by using a bisection method, the new calculations under the approach of the hypothesis tested by theχ^2-Test, whose definitions are presented in Appendix C.2. This is followed by the declaration of the program that calculates the values; and in the last subsection, the comparison of all the results is performed.

Finally, *Section 3.5* implements the results achieved to calculate further restrictions for Λ, the cut-off scale for the effective field theory approach presented in Chapter 4, Section 4.1.

To conclude, **NB Chapter 4** presents a try out of the crossed check calculations proposed when doing the approximation for the ionization form-factor presented in Appendix B.1.2, explained in Chapter 3, together with result plots, such as the one showing the conciliation of leptophilic dark matter model when having an axial-vector coupling with the results of DAMA/LIBRA (presented in Chapter 5), along with a full extended analysis of the leptophilic dark matter at LEP and ILC, which was introduced in Chapter 4 and partially developed in the results showed in Chapter 5.

Appendix C

Statistical Methods

In general, the calculation of confidence intervals (or setting of limits) on parameter of a theory is one of the main problems for an experiment. Although traditionally the approach to extract these intervals was to find the point where the -2 log λ likelihood function increased by a factor defined by the required coincidence level ($\ln \mathscr{L} + \frac{1}{2}$Method)[1], nowadays it is done by using the construction method due to Neyman, Feldman and Cousin for the case of one nuisance parameter when its value is known exactly [61].

As an alternative method to re-analyse the first DM results from the XENON100 Experiment [10], one can combine the $\ln \mathscr{L} + \frac{1}{2}$Method along with the Profile Likelihood (PL) method from statistics[2]. This Appendix presents an introduction to hypothesis testing in order to contextualize and explain briefly how the PL method was used in the XENON100 Experimet, along with a brief explanation of the complementary *Person* χ^2-test.

C.1 Profile Likelihood (PL)

C.1.1 Intro:Hypothesis Testing

Detection theory refers to the problem of observing some data and deciding whether a target is present or not. More generally, this idea fits into the context of hypothesis testing, where the problem reduces, after having observe some data, to decide if an event has occurred or not. To decide whether an event happened or not, one must apply a test to the data. In the

[1] Motivated due to the standard result from Statistics (see Casella and Berger [26]) where -2 log λ converges in a distribution to a chi-square random variable with k degrees of freedom, as later shown in Fig. C.4 (Right).

[2] This combination is motivated because the multidimensional likelihood function gets reduced to a function that only depends on the parameters of prime interest.

context of a binary test, with two possible scenarios, one refers to the case where the signal of interest is present or when the signal of interest is absent; and based on them one may define the hypothesis:

$$H_0: \quad X[n] = w[n] \quad \text{(measure data due to noise)}$$
$$H_1: \quad X[n] = s[n] + w[n] \quad \text{(measure data due to signal + noise)}$$

So, given an observation x, one would like to decide which of the two scenarios was in play[3]. Regarding the hypothesis, if the data has a fully known probability density function (pdf), one refers about having a *simple hypothesis* H_i; however, if this is not the case, one has instead a composed hypothesis.
In general, the goal is to observe some data $\underline{x}$ and to have a rule which decides the best hypothesis corresponding to this data. In the binary case, for example, one defines the region $R_0 = \{\underline{x} : \text{decide } H_0\}$ as the set where H_0 is true, and the region $R_1 = \{\underline{x} : \text{decide } H_1\}$ where H_1 is true. By decomposing $\underline{x} = [x_1, x_2]$ and having 2 components, one ends up in a scenario where one can successfully partition the space corresponding to the data so one can make a decision about from which category the data came from, see Fig. C.1.

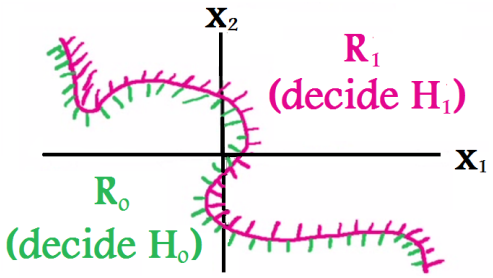

Fig. C.1 Partition of the data space into regions R_0 and R_1.

Such a categorization aims to obtain a good performance of such a decision rule. To illustrate this, one can find when characterizing the performance of a binary test that this approach leads to the following 4 possibilities:

1. "Detection": the scenario where H_1 is the true hypothesis and one decides to enforce H_1, $P_D = Prob\{H_1 \text{ true}, \text{decide } H_1\}$.

2. "False Alarm": H_0 is true, decide H_1 is true, $P_{FA} = Prob\{H_0 \text{ true}, \text{decide } H_1\}$.

In the same way, as complement:

[3]The generalization of the binary approach can be done for a multiple hypothesis test, defining that there are the possible hypothesis $H_i: \quad x[n] = s_i[n] + w[n]$ with $i = 1, 2, .., M$.

1. "Miss": H_1 is the true, decide H_0 to be true, $P_m = Prob\{H_1 \text{ true}, \text{decide } H_0 = 1 - P_D\}$.

2. "Specificity": H_0 is the true, decide H_0 true, $P_{sp} = Prob\{H_0 \text{ true}, \text{decide } H_0\} = 1 - P_{FA}$.

Recalling this classification, ones decides that H_1 is true when the data lies in the region R_1, i.e. $x \in R_1$, so the probability of false alarm, along with the probability of detection, are defined as

$$P_{FA} = \int_{x \in R_1} f(\underline{x}|H_0 \text{ true}) d\underline{x}, \qquad P_D = \int_{x \in R_1} f(\underline{x}|H_1 \text{ true}) d\underline{x}.$$

In practice, the regions R_0 and R_1 are defined using a function of the data, $T(\underline{x})$, and a threshold η, such that

$$T(\underline{x}) \underset{R_0}{\overset{R_1}{\gtrless}} = \eta \quad \Rightarrow \quad T(\underline{x}) \underset{H_0}{\overset{H_1}{\gtrless}} \eta.$$

The performance of the decision is characterized in terms of the properties of $T(\underline{x})$. Letting

$$f_{H_0}(T) = \text{pdf of } T(\underline{x}) \text{ when } H_0 \text{ is true}, \; f_{H_1}(T) = \text{pdf of } T(\underline{x}) \text{ when } H_1 \text{ is true}$$

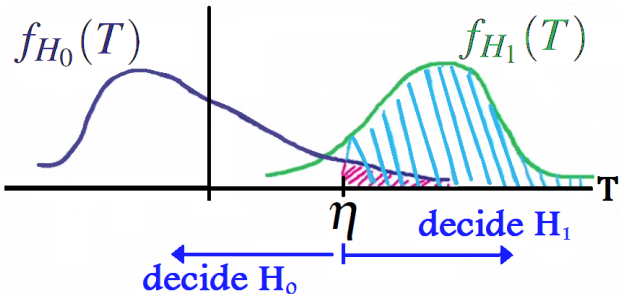

Fig. C.2 Decisions performance characterizing the data function T.

The ideal scenario would be the one where $P_{FA} = 0$ and $P_D = 1$ to have a perfect test that doesn't makes any mistakes. However, if these pdf have any overlap, then one can't choose a η that provides that performance[4].

To capture the relationship between P_{FA} and P_D associated to a test $T(x)$, one must look into the Receiver Operating Characteristic (ROC), which quantifies graphically the tradeoff between both probabilities, as can be seen in Fig. C.3.

[4]Note that there is an interplay between the problem of false alarm and the problem of detection. For example, reducing the threshold η for P_{FA} would reduce also the P_D.

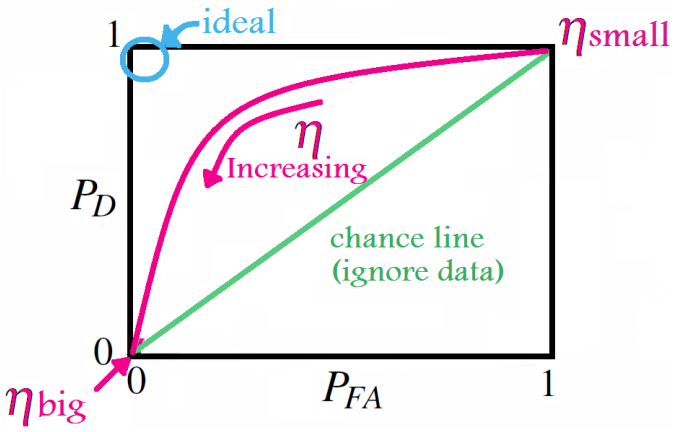

Fig. C.3 Schematics of the receiver operating characteristic, performance characterization.

The analysis of the performance characterization translates into defining the criteria for choosing a good test procedure $T(x)$, meaning to find all possible test the one that brings the ROC as close as the ideal blue point indicated in Fig. C.3. Although is difficult to identify an optimal test procedure, in the case of *simple hypothesis*, then the Neyman-Person Lemma tells what the optimal test should be. So for an observed vector $\underline{x}$, the test that maximizes P_D for any given P_{FA} is something known as the **Likelihood ratio**, defined as:

$$L(\underline{x}) = \frac{f_{H_1}(\underline{x})}{f_{H_0}(\underline{x})} \underset{H_0}{\overset{H_1}{\gtrless}} \eta,$$

where η satisfies $P_{FA} = \int_{\eta}^{\infty} f_{H_0}(L)dL$.

C.1.2 The Method

The basic idea of the profile likelihood is the following: one starts by assuming to have a probability model for some data that depends on parameters $\pi = (\pi_1, .., \pi_k)$ of interest, and also on additional nuisance parameters (number of unknown quantities) $\theta = (\theta_1, .., \theta_\ell)$. By denoting the probability density by $f(x|\pi, \theta)$ when having the independent observations $\mathbf{X} = (X_1, .., X_n)$, the full likelihood function is given by:

$$\mathscr{L}(\pi, \theta|X) = \prod_{i=1}^{n} f(X_i|\pi, \theta). \tag{C.1}$$

The procedure to obtain confidence intervals consist in finding a corresponding hypothesis test and then invert it, this is $\mathbf{H}_0 : \pi = \pi_0$ vs $\mathbf{H}_a : \pi \neq \pi_0$, so the hypothesis test can be based

on the likelihood ratio test statistic given by[5]:

$$\lambda(\pi_0|\mathbf{X}) = \frac{sup\{\mathscr{L}(\pi_0,\theta|\mathbf{X});\theta\}}{sup\{\mathscr{L}(\pi,\theta|X);\pi,\theta\}} \tag{C.2}$$

C.1.3 Implementation

In the context of the XENON100 Experiment, the parameters π correspond to the signal cross-section σ. The nuisance parameters θ, or unknown quantities of the experiment, are the number of background events N_b given the exposure and the $(S1,S2)$ parameter range in question[6], a set of probabilities $\varepsilon_s = \{e_s^j\}$ and $\varepsilon_b = \{e_b^j\}$ which describe the distribution of the signal and background events in a plane defined by $(S1,S2)$, the relative scintillation efficiency $\mathscr{L}_{eff}$ and the scape velocity v_{esc} [12].

Following the formulation introduced in eq (C.1), the full likelihood function $\mathscr{L}$ for a given WIMP of mass m_χ and cross-section σ is defined as:

$$\begin{aligned}\mathscr{L} = \mathscr{L}_1(\sigma, N_b, \varepsilon_s, \varepsilon_b, \mathscr{L}_{eff}, v_{esc}; m_\chi) \times \mathscr{L}_2(\varepsilon_s) \times \mathscr{L}_3(\varepsilon_b) \\ \times \mathscr{L}_4(\mathscr{L}_{eff}) \times \mathscr{L}_5(v_{esc}).\end{aligned} \tag{C.3}$$

The first term L_1 describes the main measurement of the XENON100 detector, while the rest of the terms L_i constrain the nuisance parameters. Postponing the definition for these terms, in order to complete the formulation idea to exclude a WIMP with a specific mass and cross section as presented by eq (C.2), one uses a statistic test q_σ to reduce the observed data to only one value in order to test the signal hypothesis H_σ. It is defined as:

$$q_\sigma = \begin{cases} -2\log\lambda & \widehat{\sigma} < \sigma \\ 0 & \widehat{\sigma} > \sigma \end{cases}, \tag{C.4}$$

where $\widehat{\sigma}$ denotes the values of σ that maximizes the likelihood eq (C.3). By construction, $0 \leq \lambda(\sigma) \leq 1$, thus $q_\sigma \geq 0$. q_σ is equals zero when the best-fit value of the cross-section $\widehat{\sigma}$ is equals the hypothesized value σ, which corresponds to the most signal-like outcome. Larger values of the test statistic q_σ indicate that the data are less compatible with the signal hypothesis H_σ.

[5] In the context of nuisance parameters, λ is known as the profile likelihood, it is a function of π_0 (and data) only, it doesn't depend on the nuisance parameters θ.

[6] S_1 and S_2 correspond to the events recorded in the experiment, the prompt and proportional scintillation signals respectively.

In accordance with the concepts introduced in the previous section, one can define $f(q_\sigma|H_\sigma)$ to be the probability distribution of the test statistic q_σ under the signal hypothesis H_σ and q_σ^{obs} (analogous to η), as the value of the test statistic obtained with the observed data. One can define, analogous to the "Detection" scenario of the signal, the probability that the outcome of an experiment results in a test statistic q_σ larger than the observed one q_σ^{obs} when the signal hypothesis H_σ is true, by

$$p_s = \int_{q_\sigma^{obs}}^{\infty} f(q_\sigma|H_\sigma)dq_\sigma. \tag{C.5}$$

Due to the fluctuations of the background, p_s needs to be modified introducing

$$p_s' = \frac{ps}{1-p_b} \quad \text{where, like the "specificity":} \quad 1-p_b = \int_{q_\sigma^{obs}}^{\infty} f(q_\sigma|H_0)dq_\sigma, \tag{C.6}$$

where $H_{\sigma=0} = H_0$. The upper limit $\sigma^{up}(m_\chi)$ on the cross-section σ for a given WIMP mass m_χ is found by solving: $p_s'(\sigma = \sigma^{up}(m_\chi)) = 10\%$.
Lastly, to fully specify the likelihood function one starts looking the calibration data for both the ER background and the NR signal. The number of calibration events used in the 4 PE-20 PE $S1$-region is $M_s = 18907$ NR from $^{241}AmBe$ and $Mb = 5053$ ER from Compton-scattered ^{60}Co gammas, divided into j = $1,..,(K = 23)$ bands in the (S_1, S_2) plane[7], as shown in Fig. C.4 (Left).

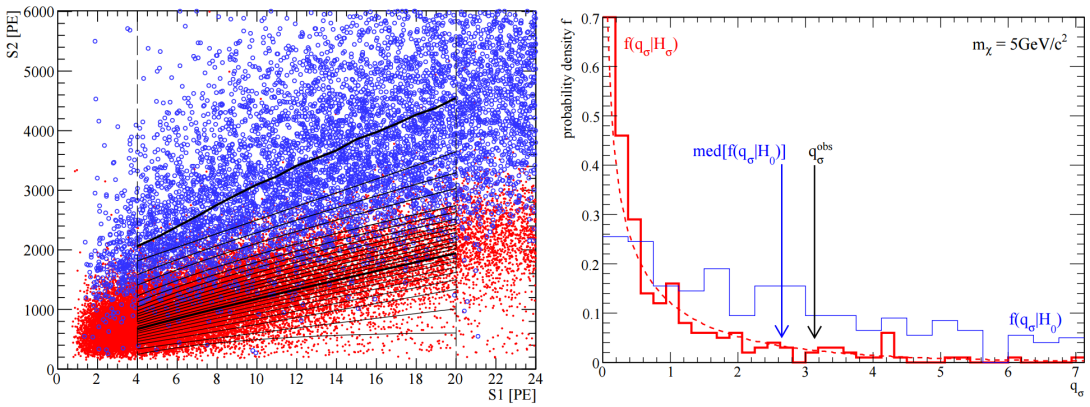

Fig. C.4 (Left)Scatter plot of ER from a ^{60}Co source (blue circles) and NR from an $^{241}AmBe$ source (red dots). Superimposed are the border lines of the bands j (thin lines). (Right) The probability density functions $f(q_\sigma|H_\sigma)$ (thick red histogram) and $f(q_\sigma|H_0)$ (thin blue histogram) for a WIMP with $m_\chi = 5GeV/c^2$ and $\sigma = \sigma^{up}$. It is clear that the distribution is well approximated by a chi-square distribution (dashed red line).

[7] In this context, ε_s^j and ε_b^j are the corresponding probabilities for a signal or background event to fall in a given band j.

First, given a set of n^j data points $(S1_i, S2_i)$ in a band j, the likelihood that these points emerge from a given WIMP spectrum is given by

$$\mathscr{L}_1 = \prod_j^K Poiss(n^j|\varepsilon_s^j N_s + \varepsilon_b^j N_b) \times \prod_{i=1}^{n^j} \frac{\varepsilon_s^j N_s f_s(S1_i) + \varepsilon_b^j N_b f_b(S1_i)}{\varepsilon_s^j N_s + \varepsilon_b^j N_b}, \tag{C.7}$$

where $f_s(S1)$ is the predicted normalized WIMP spectrum[8]. Now, by taking the calibration measurements as control measurements of m_s^j and m_b^j events in band j, assumed to be Poisson distributed. With these choice, with expectations $\varepsilon_{s,b}^j M_{s,b}$, one can express

$$\mathscr{L}_2(\varepsilon_s^j) = \prod_j^K Poiss(m_s^j|\varepsilon_s^j M_s), \quad \mathscr{L}_3(\varepsilon_b^j) = \prod_j^K Poiss(m_b^j|\varepsilon_b^j M_b), \tag{C.8}$$

For one hand, the relative scintillation efficiency $\mathscr{L}_{eff}$ is the largest systematic uncertainty for the data analyzed, and one can parametrize its uncertainty with a nuisance parameter t[9], while for the uncertainty on the escape velocity v_{esc}, using the asymmetric probability distribution f_v shown in Fig. 7 of [68], the likelihood terms of these variables are defined as

$$\mathscr{L}_4(\mathscr{L}_{eff}) = exp(-(t - t_{obs})^2/2), \quad \mathscr{L}_5(v_{esc}) = f_v(v_{obs}|v_{esc}). \tag{C.9}$$

For completeness, it can be indicated that the signal rate in number of photoelectrons n is given by

$$\frac{dR}{dn} = \int_0^\infty dR \frac{dR}{dE}(E; m_\chi, v_{esc}) \times Poiss(n|\nu(E)), \tag{C.10}$$

where $\nu(E)$, the expected number of photoelectrons for a given recoil energy E_{NR}, is given by $\nu(E_{NR}) = E_{NR} \times \mathscr{L}_{eff}(E_{NR}) \times S_{nr}/S_{ee} \times L_y$[10]. Also, by considering the finite average single-photoelectron resolution $\sigma_{PMT} = 0.5$ PE, the resulting S1-spectrum is given by

$$\frac{dR}{dS1} = \sum_{n=1}^\infty Gauss(S1|n, \sqrt{n}\sigma_{PMT}) \times \frac{dR}{dn} \times \varepsilon_{cuts}(S1), \tag{C.11}$$

where $\varepsilon_{cuts}(S1)$ is the acceptance of the applied cuts. The test statistics q_σ is obtained when plugging the likelihood obtained overall, into eqs C.3 and C.4.

[8] Specifically $f_s(S1; m_\chi) = \frac{dR}{dS1}(m_\chi) / \int_{S1_{lower}}^{S1_{upper}} \frac{dR}{dS1}(m_\chi) dS1$, see eq (C.11).

[9] The recoil energy dependence of $\mathscr{L}_{eff}$ together with its uncertainty are taken from a Gaussian fit of all direct detection measurements, as shown in Fig. 1 of [4].

[10] $S_{ee} = 0.58$ and $S_{nr} = 0.95$ are the scintillation quenching factors due to the electric field for electronic and NR. The light yield L_y was measured to be $L_y(122keV_{ee}) = (2.20 \pm 0.09) PE/keV_{ee}$.

C.2 χ^2-test

A chi-squared test is any statistical hypothesis test used to show whether or not there is relationship between two categorical variables. In principle, it tests a null hypothesis H_0 stating that the frequency distribution of certain events observed in a sample are consistent with a particular theoretical distribution.

Pearson's chi-squared test can be used to approach two different types of comparison: tests of *goodness of fit* and *tests of independence*. The procedure starts by calculating the χ^2-test, determine the degrees of freedom (df), or the number of categories reduced by the number of parameters of the fitted distribution, and then in selecting a desired confidence level (CL) for the result of the test[11]. After having these results, one compares the χ^2 value obtained to the value from the chi-squared distribution given the chosen df and the selected CL. The comparison is an indication to accept or reject the null hypothesis, since indicates how different is the distribution to the expected(theoretical) distribution. If the test statistic exceeds the critical value of χ^2, H_0 can be rejected with the selected CL.

The value of the test-statistic is defined as

$$\chi^2 = \sum_{i=1}^{n} \frac{(O_i - E_i)^2}{E_i}, \tag{C.12}$$

where χ^2 is the Pearson's cumulative test statistic, O_i are the observed values, E_i are the expected ones, or predicted, asserted by the null hypothesis, and n is an entry for the number data considered in the calculations.

[11] A full *Chi-Square Distribution Standard Table* can be found online, for example, in https://www.medcalc.org/manual/chi-square-table.php.

Appendix D

Complementary calculations

D.1 Interaction's mediator

This appendix presents how the analysis described in Section 4.1 does not rely on any specific realization of an effective interaction, see Fig. 4.1. In that sense, the simplest approach is to assume that the interaction is induced by the exchange of an intermediate particle whose mass is much larger (or much smaller) than the recoil momenta. One can take a look at the χ-lepton interaction mediated by a scalar field ϕ, as shown in Fig. D.1.

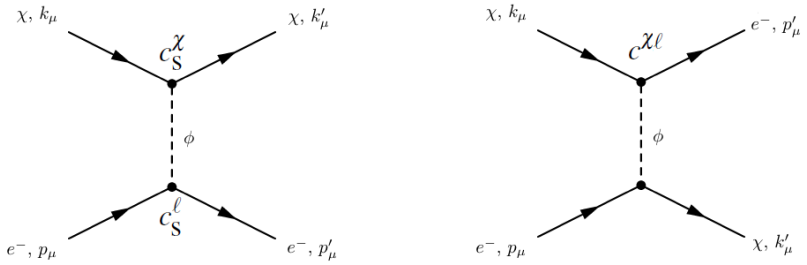

Fig. D.1 (Left) t-channel diagram. (Right) u-channel diagram.

First case For the diagram showed to the left in Fig. D.1, representing the t-channel, the invariant amplitude is given by:

$$\begin{aligned}
\mathscr{M} &= \overline{u}_{\chi}^{s'}(k')\ ic_s^{\chi} u_{\chi}^{s}(k) \frac{i}{q^2 - m_{\phi}^2 + i\varepsilon} \overline{u}_{\ell}^{r'}(p')\ ic_s^{\ell} u_{\ell}^{r}(p) \\
i\mathscr{M} &= \frac{[\overline{u}_{\chi}^{s'}(k')\ c_s^{\chi} u_{\chi}^{s}(k)][\overline{u}_{\ell}^{r'}(p')\ c_s^{\ell} u_{\ell}^{r}(p)]}{q^2 - m_{\phi}^2 + i\varepsilon} \\
(i\mathscr{M})^{\dagger} &= \frac{[\overline{u}_{\ell}^{r}(p)\ c_s^{\ell} u_{\ell}^{r'}(p')][\overline{u}_{\chi}^{s}(k)\ c_s^{\chi} u_{\chi}^{s'}(k')]}{q^2 - m_{\phi}^2 + i\varepsilon}
\end{aligned} \tag{D.1}$$

If $q^2 = (p'-p)^2 \ll m_\phi^2$ then $\frac{1}{q^2-m_\phi^2+i\varepsilon} \simeq -\frac{1}{m_\phi^2}$, the invariant amplitude becomes

$$\begin{aligned}
|\mathscr{M}|^2 &= \frac{1}{4m_\phi^4}\left(\sum_r u_\ell^r(p)\overline{u}_\ell^r(p)\right)_{da} c_{sab}^\ell \left(\sum_{r'} u_\ell^{r'}(p')\overline{u}_\ell^{r'}(p')\right)_{bc} c_{scd}^\ell \\
&\times \left(\sum_s u_\chi^s(p)\overline{u}_\chi^s(p)\right)_{he} c_s^\chi{}_{ef} \left(\sum_{s'} u_\chi^{s'}(k')\overline{u}_\chi^{s'}(k')\right)_{fg} c_s^\chi{}_{gh} \\
&= \frac{1}{4m_\phi^4} Tr[(\not{p}+m_e)\ c_s^\ell(\not{p}'+m_e)\ c_s^\ell] Tr[(\not{k}+m_\chi)\ c_s^\chi(\not{k}'+m_\chi)\ c_s^\chi] \\
&= \frac{4(c_s^\ell c_s^\chi)^2}{m_\phi^4}[(p\cdot p')(k\cdot k') + (p\cdot p')m_\chi^2 + (k\cdot k')m_e^2 + m_\chi^2 m_e^2]
\end{aligned} \tag{D.2}$$

Now, from $E-p$ conservation $p_\mu p^\mu = E^2 - p^2 = m^2$ (when taking $c=1$) and from conservation of momentum: $k+p = k'+p' \ \Rightarrow k\cdot k' = m_\chi^2 - q^2/2, \ \ p\cdot p' = m_e^2 - q^2/2$. Rewriting everything in these terms:

$$\begin{aligned}
|\mathscr{M}|^2 &= \frac{4(c_s^\ell c_s^\chi)^2}{m_\phi^4}\left[\left(m_e^2 - \frac{q^2}{2}\right)\left(m_\chi^2 - \frac{q^2}{2}\right) + \left(m_e^2 - \frac{q^2}{2}\right)m_\chi^2 \right. \\
&\left. + \left(m_\chi^2 - \frac{q^2}{2}\right)m_e^2 + m_e^2 m_\chi^2\right] \\
|\mathscr{M}|^2 &= \frac{(c_s^\ell c_s^\chi)^2}{m_\phi^4}\left[16m_e^2 m_\chi^2 - 4(m_e^2+m_\chi^2)q^2 + q^4\right]
\end{aligned} \tag{D.3}$$

Since $q^2 \ll m_\phi^2$:

$$|\mathscr{M}|^2 \simeq 16(c_s^\ell c_s^\chi)^2 \frac{m_e^2 m_\chi^2}{m_\phi^4} \tag{D.4}$$

Second case

As for the diagram showed to the right in Fig. D.1, representing the u-channel, the invariant

amplitude is given by:

$$\begin{aligned}
\mathscr{M} &= \overline{u}_{\ell}^{r'}(p')\; ic_s^{\chi\ell} u_{\chi}^{s}(k) \frac{i}{q^2 - m_{\phi}^2 + i\varepsilon} \overline{u}_{\chi}^{s'}(k')\; ic_s^{\chi\ell} u_{\ell}^{r}(p) \\
i\mathscr{M} &= \frac{[\overline{u}_{\ell}^{r'}(p')\; c_s^{\chi\ell} u_{\chi}^{s}(k)][\overline{u}_{\chi}^{s'}(k')\; c_s^{\chi\ell} u_{\ell}^{r'}(p')]}{q^2 - m_{\phi}^2 + i\varepsilon} \\
(i\mathscr{M})^{\dagger} &= \frac{[\overline{u}_{\ell}^{r}(p)\; c_s^{\chi\ell} u_{\chi}^{s'}(k')][\overline{u}_{\chi}^{s}(k)\; c_s^{\chi\ell} u_{\ell}^{r'}(p')]}{q^2 - m_{\phi}^2 + i\varepsilon}
\end{aligned} \tag{D.5}$$

If $q^2 = (p'-p)^2 \ll m_{\phi}^2$ then $\frac{1}{q^2 - m_{\phi}^2 + i\varepsilon} \simeq -\frac{1}{m_{\phi}^2}$. So that

$$\begin{aligned}
|\mathscr{M}|^2 &= \frac{1}{4m_{\phi}^4} \left(\sum_r u_{\ell}^{r}(p) \overline{u}_{\ell}^{r}(p) \right)_{da} c_s^{\chi\ell}{}_{ab} \left(\sum_{r'} u_{\ell}^{r'}(k') \overline{u}_{\ell}^{r'}(k') \right)_{bc} c_s^{\chi\ell}{}_{cd} \\
&\times \left(\sum_s u_{\chi}^{s}(k) \overline{u}_{\chi}^{s}(k) \right)_{he} c_s^{\chi\ell}{}_{ef} \left(\sum_{s'} u_{\chi}^{s'}(k') \overline{u}_{\chi}^{s'}(k') \right)_{fg} c_s^{\chi\ell}{}_{gh} \\
&= \frac{1}{4m_{\phi}^4} Tr[(\not{p} + m_e)\; c_s^{\chi\ell} (\not{k}' + m_{\chi})\; c_s^{\chi\ell}] Tr[(\not{k} + m_{\chi})\; c_s^{\chi\ell} (\not{p}' + m_e)\; c_s^{\chi\ell}] \\
&= \frac{4(c_s^{\chi\ell})^4}{m_{\phi}^4} [(p\cdot k')(k\cdot p') + (p\cdot k' + k\cdot p') m_{\chi} m_e + m_{\chi}^2 m_e^2]
\end{aligned} \tag{D.6}$$

Now, from $E-p$ conservation $p_{\mu}p^{\mu} = E^2 - p^2 = m^2$ (when taking $c=1$) and from conservation of momentum: $k + p = k' + p' \;\Rightarrow (k-p')^2 = (k'-p)^2 = u$. Solving for the variables of interest, $k\cdot p' = \frac{m_{\chi}^2}{2} + \frac{m_e^2}{2} - \frac{u}{2}$ and $k'\cdot p = \frac{m_{\chi}^2}{2} + \frac{m_e^2}{2} - \frac{u}{2}$. Rewriting everything in these terms:

$$\begin{aligned}
|\mathscr{M}|^2 &= \frac{(c_s^{\chi\ell})^4}{m_{\phi}^4} \big[m_e^4 + m_{\chi}^4 + u^2 + 6m_e^2 m_{\chi}^2 - 2(m_e^2 + m_{\chi}^2)u \\
&\quad + 4(m_{\chi}^3 m_e + m_e^3 m_{\chi} - u m_e m_{\chi}) \\
|\mathscr{M}|^2 &= \frac{(c_s^{\ell} c_s^{\chi})^2}{m_{\phi}^4} \big[(u - (m_{\chi} + m_e)^2)^2 \big]
\end{aligned} \tag{D.7}$$

Since $q^2 = u \ll m_{\phi}^2$:

$$|\mathscr{M}|^2 \simeq (c_s^{\chi\ell})^4 \frac{(m_{\chi} + m_e)^4}{m_{\phi}^4} \tag{D.8}$$

D.2 $\overline{|\mathscr{M}_{VA}|^2}$

The following calculations present the invariant amplitude for $DM - e^-$ scattering by using a Fermi-like 4-fermion contact interaction in the case of vector-type couplings between dark matter and leptons. The most relevant scenario, as discussed in Section 4.1, where $DM - e^-$ scattering dominates among the possible processes that can take place ends up being axial-vector couplings.

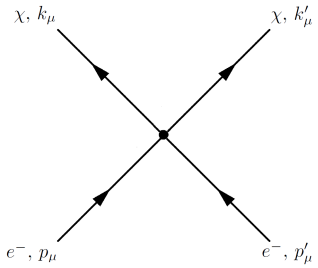

Fig. D.2 The $\chi - e^-$ scattering and definition of the momentum variables in the laboratory frame.

As shown in Fig. D.2, in the invariant amplitude produced, the squared matrix element is averaged over the initial spins and summed over the final ones, obtaining in that way

$$\overline{|\mathscr{M}_{VA}|^2} = G^2 L_\chi^{\mu\nu} L^e_{\mu\nu}, \tag{D.9}$$

where:

$$L_\chi^{\mu\nu} = \frac{1}{2}\sum_{spin}\left[\overline{U}_\chi(k')\gamma^\mu(c_V^\chi + c_A^\chi\gamma_5)U_\chi(k)\right]\left[\overline{U}_\chi(k)\gamma^\nu(c_V^\chi + c_A^\chi\gamma_5)U_\chi(k')\right] \tag{D.10}$$

$$L^e_{\mu\nu} = \frac{1}{2}\sum_{spin}\left[\overline{U}_e(p')\gamma_\mu(c_V^\ell + c_A^\ell\gamma_5)U_e(p)\right]\left[\overline{U}_e(p)\gamma_\nu(c_V^\ell + c_A^\ell\gamma_5)U_e(p')\right]. \tag{D.11}$$

Now, one can focus in eq (D.10) or in eq (D.11), given that they have the same structure. One can split the first term into:

$$\begin{aligned} L_\chi^{\mu\nu} &= \frac{1}{2}Tr\left[(\not{k}' + m_\chi)\gamma^\mu(c_V^\chi + c_A^\chi\gamma_5)(\not{k} + m_\chi)\gamma^\nu(c_V^\chi + c_A^\chi\gamma_5)\right] \\ &= L_\chi^{AA} + L_\chi^{VA} + L_\chi^{AV} + L_\chi^{VV}, \end{aligned} \tag{D.12}$$

where the four terms are explicitly:

$$L_\chi^{AA} = \frac{1}{2}Tr\left[(\not{k}' + m_\chi)\gamma^\mu c_A^\chi\gamma_5(\not{k} + m_\chi)\gamma^\nu c_A^\chi\gamma_5\right] \tag{D.13}$$

$$L_\chi^{VA} = \frac{1}{2} Tr\left[(\not{k}' + m_\chi)\gamma^\mu c_V^\chi (\not{k} + m_\chi)\gamma^\nu c_A^\chi \gamma_5\right] \tag{D.14}$$

$$L_\chi^{AV} = \frac{1}{2} Tr\left[(\not{k}' + m_\chi)\gamma^\mu c_A^\chi \gamma_5 (\not{k} + m_\chi)\gamma^\nu c_V^\chi\right] \tag{D.15}$$

$$L_\chi^{VV} = \frac{1}{2} Tr\left[(\not{k}' + m_\chi)\gamma^\mu c_V^\chi (\not{k} + m_\chi)\gamma^\nu c_V^\chi\right] \tag{D.16}$$

Given that the gamma matrices follow properties like:

$$\begin{aligned} Tr(\gamma^\mu \gamma^\nu) &= 4g^{\mu\nu} \\ Tr(\gamma^\mu \gamma^\nu \gamma^\lambda \gamma^\sigma) &= 4(g^{\mu\nu} g^{\lambda\sigma} - g^{\mu\lambda} g^{\nu\sigma} + g^{\mu\sigma} g^{\nu\lambda}) \\ Tr(\gamma_5 \gamma^\mu \gamma^\nu \gamma^\lambda) &= 0 \end{aligned} \tag{D.17}$$

By using these trace theorems, one can rewrite the eqs defined before as:

$$L_\chi^{AA} = 2(c_A^\chi)^2 \left((k'^\mu k^\nu + k'^\nu k^\mu - k' \cdot k g^{\mu\nu} - m_\chi^2 g^{\mu\nu}\right) \tag{D.18}$$

$$L_\chi^{VV} = 2(c_V^\chi)^2 \left((k'^\mu k^\nu + k'^\nu k^\mu - k' \cdot k g^{\mu\nu} + m_\chi^2 g^{\mu\nu}\right) \tag{D.19}$$

$$L_\chi^{AV} = \frac{1}{2} Tr\left[(\not{k}' + m_\chi)\gamma^\mu (\not{k} - m_\chi)\gamma^\nu c_A^\chi \gamma_5 c_V^\chi\right] \tag{D.20}$$

$$L_\chi^{VA} = \frac{1}{2} c_V^\chi c_A^\chi Tr\left[\gamma_5 \not{k}' \gamma^\mu \not{k} \gamma^\nu\right] = L_\chi^{AV} \tag{D.21}$$

$$L_\chi^{VA} + L_\chi^{AV} = -c_V^\chi c_A^\chi 4i\varepsilon^{\alpha\mu\beta\nu} k'_\alpha k_\beta \tag{D.22}$$

Which means that as a whole, eq (D.12) can be written as:

$$\begin{aligned} L_\chi^{\mu\nu} &= 2((c_V^\chi)^2 + (c_A^\chi)^2)\left[(k'^\mu k^\nu + k'^\nu k^\mu - k \cdot k' g^{\mu\nu}\right] \\ &\quad + 2((c_V^\chi)^2 - (c_A^\chi)^2) m_\chi^2 g^{\mu\nu} - 4c_V^\chi c_A^\chi i\varepsilon^{\alpha\mu\beta\nu} k'_\alpha k_\beta \end{aligned} \tag{D.23}$$

Due to the fact that $L_{\mu\nu}^e$ has the same structure, it takes quite the same result. This allows to put everything together in the definition for $|\mathscr{M}_{V-A}|^2$ as:

$$\begin{aligned} \overline{|\mathscr{M}_{VA}|^2} &= G^2 L_\chi^{\mu\nu} L_{\mu\nu}^e \\ &= 4G^2 \Big\{ ((c_V^\chi)^2 + (c_A^\chi)^2)\left(k'^\mu k^\nu + k'^\nu k^\mu - k \cdot k' g^{\mu\nu}\right) \\ &\quad + ((c_V^\chi)^2 - (c_A^\chi)^2) m_\chi^2 g^{\mu\nu} - 2c_V^\chi c_A^\chi i\varepsilon^{\alpha\mu\beta\nu} k'_\alpha k_\beta] \\ &\quad \times [((c_V^\ell)^2 + (c_A^\ell)^2)\left(p'^\mu p^\nu + p'^\nu p^\mu - p \cdot p' g^{\mu\nu}\right) \\ &\quad + ((c_V^\ell)^2 - (c_A^\ell)^2) m_e^2 g^{\mu\nu} - 2c_V^\ell c_A^\ell i\varepsilon_{\alpha\mu\beta\nu} p'_\alpha p_\beta \Big\} \end{aligned} \tag{D.24}$$

Now, one can use the fact that:

$$\varepsilon^{\alpha\mu\beta\nu}\varepsilon_{\alpha\mu\beta\nu} = 4! = 24 \quad \text{and} \quad g^{\mu\nu}g_{\mu\nu} = 4$$

If additionally one chooses to reduce the notation by introducing:

$$q = (c_V^\chi)^2 + (c_A^\chi)^2 \qquad r = (c_V^\chi)^2 - (c_A^\chi)^2 \qquad s = (c_V^\ell)^2 + (c_A^\ell)^2 \qquad r = (c_V^\ell)^2 - (c_A^\ell)^2 \tag{D.25}$$

$$\begin{aligned}\overline{|\mathscr{M}_{VA}|^2} &= G^2 L_\chi^{\mu\nu} L_{\mu\nu}^e \\ &= 8G^2\Big\{\mathscr{A}(p'\cdot k')(p\cdot k) + \mathscr{B}(p'\cdot k)(p\cdot k') + \mathscr{C}(k'\cdot k)m_e^2 - \mathscr{D}(p'\cdot p)m_\chi^2\Big\}\end{aligned} \tag{D.26}$$

where

$$\begin{aligned}\mathscr{A} &= q\cdot s + 4c_V^\chi c_V^\ell c_A^\chi c_A^\ell \\ &= ((c_V^\ell)^2 + (c_A^\ell)^2)((c_V^\chi)^2 + (c_A^\chi)^2) + 4c_V^\chi c_V^\ell c_A^\chi c_A^\ell \\ &= (c_V^\ell c_V^\chi + c_A^\ell c_A^\chi)^2 + (c_V^\ell c_A^\chi + c_A^\ell c_V^\chi)^2 \\ \mathscr{B} &= q\cdot s - 4c_V^\chi c_V^\ell c_A^\chi c_A^\ell \\ &= (c_V^\ell c_V^\chi - c_A^\ell c_A^\chi)^2 + (c_V^\ell c_A^\chi - c_A^\ell c_V^\chi)^2 \\ \mathscr{C} &= ((c_V^\chi)^2 + (c_A^\chi)^2)((c_V^\ell)^2 - (c_A^\ell)^2) \\ \mathscr{D} &= ((c_V^\chi)^2 - (c_A^\chi)^2)((c_V^\ell)^2 + (c_A^\ell)^2)\end{aligned} \tag{D.27}$$

In the case of $V \pm A$ interaction ($|c_V^\ell| = |c_A^\ell|$ and $|c_V^\chi| = |c_A^\chi|$), the matrix element is:

$$\overline{|\mathscr{M}_{V\pm A}|^2} = 8G^2\Big[\mathscr{A}(p'\cdot k')(p\cdot k) + \mathscr{B}(p'\cdot k)(p\cdot k')\Big] \tag{D.28}$$

since χ is not relativistic, one obtains that $(p'\cdot k')(p\cdot k) \simeq p'_0 k'_0 p_0 k_0$ and $(p'\cdot k)(p\cdot k') \simeq p'_0 k'_0 p_0 k_0$; moreover for $E_R \sim KeV$, one has $p'_0 \simeq p_0$, giving:

$$\overline{|\mathscr{M}_{V\pm A}|^2} = 16G_{V\pm A}^2 m_\chi^2 p_0^2, \tag{D.29}$$

where the Fermi effective coupling constant is defined as:

$$G_{V\pm A}^2 = G^2((c_V^\ell)^2 + (c_A^\ell)^2)((c_V^\chi)^2 + (c_A^\chi)^2). \tag{D.30}$$